Optimization of a Time Resolved Magneto Optical Kerr Effect Magnetometer Over Nanosecond Time-Scales with Femtosecond Resolution

by

Christina Balanduk

A Thesis submitted to the Faculty of Graduate Studies of
The University of Manitoba
in partial fulfillment of the requirements of the degree of

MASTERS OF SCIENCE

Department of Physics and Astronomy
University of Manitoba
Winnipeg

Abstract

Time-resolved magneto-optic studies of magnetic materials are of wide interest across the globe today as we constantly search for new ways to push the development of technology forward. The development of technology requires new and innovative characterization methods to determine which materials are worth our research focus. The time-resolved magneto-optical Kerr effect (TR-MOKE) has been a characterization tool applied to study magneto-dynamic phenomena over time-scales down to tens of femtoseconds, known as ultrafast phenomena, since the 1990s. This thesis will present the development a TR-MOKE magnetometer that implements a dual-delay line configuration to obtain resolution shorter than one picosecond for a total delay over ten nanoseconds. The apparatus, which is developed throughout this work, will be capable of measuring spin waves with GHz frequencies down to ultrafast switching phenomena in the THz range, allowing for the investigation of long- and short-time scale magneto-dynamic phenomena. This apparatus is additionally designed for versatility. Alterations were made to obtain preliminary time-resolved infrared spectroscopy measurements over nanosecond timescales.

Acknowledgements

I have many people to thank for support during the completion of this thesis work. I have to start by thanking my supervisor Dr. Jacob Burgess for providing frequent support and ideas throughout this work. I'm endlessly grateful for the many skills I have developed under his supervision and look forward to growing more as a researcher in this lab in years to come.

I'd like to thank the many students who have passed through this lab over the years. Akif Ahmed, AJ Braconnier and Josh Gibbs all assisted in my initial training in this lab and provided a soundboard for ideas when I ran into obstacles. A special thank you goes to Sangeev Selvaratnam for all of his assistance in designing and printing 3D pieces. Sangeev would offer assistance at the drop of a hat and it was always highly appreciated.

I need to acknowledge the work of those who had a hand in the earliest days of this experiment; Nils Refvik, Brydyn Mac Intyre, and August Mendelsohn all made contributions to this work before I joined the lab.

I'd like to thank the office staff Robyn Beaulieu, Aymsley Bishop Mahon, and especially Susan Beshta for all that you do within the department and to keep students like me on track.

I'd like to thank my friends Brynne Blaikie and Katryna Fast for the constant support, many laughs, and the endless joy they bring to my life. Brynne and Kate are some of the most supportive people I've ever met and I wouldn't be the person I am without them.

I'd like to thank my partner Eric Horn for all of his support and all of the time he would spend listening to me talk about the details of my work. Thank you for all of the support and love you provided during some of the most difficult times of the past few years.

Finally, I'd like to extent my gratitude to mine and Eric's families. Every time my grandma would take down notes to tell my grandpa about the work I do or Eric's grandpa would ask me questions about physics news he'd heard filled my life with joy. Every person within each of our families has made me feel so loved and accepted.

To my loving friends

Contents

List of Figures

Chapter 1

Introduction

Magnets have stolen the attention and curiosity of many throughout time. Magnetism is a fascinating phenomenon which has been observed throughout history, but still grabs the attention of scientists around the world to this day. In Coey's discussion of magnetism in the past, present, and future, he describes seven distinct "ages of magnetism" where the field saw huge changes [1, 2]. For example, it was in the 1820s that Oersted accidentally discovered that magnetism and electricity were related, this directly lead to the development of the electromagnet, allowing for the first time for a tunable magnetic field. As time goes on, interest in the study of magnetism continues to grow steadily and today much of the study of magnetism is towards developing and improving magnetic memory storage devices as the need to efficiently store and access large amounts of information grows [3].

To highlight the current status of the field, we can turn to the Magnetism Roadmap published in 2014, 2017, and again in 2020 [4–6]. Through these publications, many experts within the field were able to describe the current state of magnetism at the time from their perspective, leading to these being an insightful resource for observing where the focus of the field is at present.

In 2014, the first edition of the Magnetism Roadmap was published, attempting to sum up some of the major topics in the field at that snapshot in time. The major topics covered included nano-scale phenomena and materials, as well as magnon spintronics studying magnetic effects over GHz frequencies and magnetic applications within the world of biotechnology. The 2014 roadmap additionally held discussion of the status of research into permanent magnets and other technologies in development.

The 2017 and 2020 chronicles shift to have more emphasis placed on to topological spin textures and ultrafast magneto-dynamics. Within recent years there has been much study into phenomena such as all-optical magnetization reversal. This was noted in 2007 when Stanciu et al. studied a thin film of a GdFeCo alloy with circularly polarized

laser light [7].

The field of magnetism is expanding constantly and there is a push for more detailed characterization and understanding of materials. Throughout this thesis, we will incentivize the development of an apparatus to study a variety of magnetic behavior using the time-resolved magneto-optical Kerr effect over nanosecond timescales with femtosecond resolution to continue to add to the wealth of information with the goal of expanding our understanding of magneto-dynamics.

The techniques used here for the measurement of TR-MOKE were first developed by Mark Freeman in 1991 when he excited charge carriers in an emission line with a 300 fs pulse and used a probe to study the changing magnetic state of microscopic samples [8]. Measurement methods were further developed by Wayne Hiebert in 2001 [9] and these are the resources on which the methodologies used here will largely build.

1.1 Motivation

The unique nature of the apparatus developed throughout this work stems from the utilization of a dual-delay line configuration. One of the delay lines used can provide a time delay up to 297 ps reliably with step sizes of 33 fs. This short delay allows for the observation of rapid excitations up to THz frequencies (10^{12} Hz). There is an additional option to microstep for increased temporal resolution below the 33 fs threshold.

The second delay line is a 2 meter long rail with a cart moved using an arduino and a stepper motor. Once work has been completed, as we will discuss in this thesis, the functional area of this longer delay line allows a time delay of up to 10.7 ns, with a step size of ~1.3 ps. This delay line allows for the measurement of slow spin-wave modes down to GHz (10^9 Hz) frequencies.

The dual-delay configuration positions us uniquely to study high frequency waves over long time spans. This means we are able to detect a multitude of complex excitations and any nonlinear conversions from low frequency phenomena to high frequency spin waves over long periods of time.

In the section to follow, we will outline how this thesis will proceed to describe the physics required for the context of this research and the steps towards developing the apparatus which is the primary focus of this work. We will then discuss in the history of magnetism to understand the path the field has taken throughout time, and develop an understanding of how we expect the progress in magnetic research to develop in the future.

1.2 Outline

To begin this thesis, we will discuss many of the relevant topics within magnetism to motivate the development of an apparatus to study the time-resolved magneto-optical Kerr effect over long and short delay times. For the remainder of this chapter we will discuss many of the major developments in magnetism throughout time in order to understand the trajectory of the field. Once we have developed an appreciation of the history that brought magnetism to its current status we may focus in on developing a more rigorous mathematical framework for magnetism as it stands today.

Chapter 2 will aim to develop the mathematics and theoretical understanding of the phenomena this apparatus is capable of observing. We will explore the origins of magnetism within materials before diving into the many dynamic phenomena which this apparatus is designed to study as well as some samples which will be of interest as a result. It is here where we'll introduce the Magneto-Optical Kerr Effect (MOKE) to understand how we may study these magneto-dynamic effects.

In chapter 3, the theoretical discussion will narrow to that the critical optics used in the development of this apparatus. This chapter is aimed to break down many of the considerations that went into the development of this apparatus. We will elaborate on the light used for the study of magnetic materials as well as the ways in which it is manipulated in order to observe the effects discussed in the prior chapter.

Chapter 4 will then explore the necessary steps taken towards obtaining time resolution. At this stage in the experiment we will have already observed the way a magnetized sample can alter the light reflected from it's surface. The aim of this chapter is then to demonstrate the reasonable expectation of time resolution using a pump-probe measurement technique. This chapter will additionally discuss the many methods of optically altering a magnetic sample to study its dynamic behaviour.

Chapter 5 will display one of the various modifications which can be easily made to the design of this apparatus in order to complete an entirely different experiment. The lay-out of this apparatus is intentionally designed such that modifications may be made to complete different measurements, such as time-resolved spectroscopy. The dual-delay line design may be useful for measurements outside of MOKE, this chapter discussed the first demonstration of this utility with more to come in the future.

Finally we will conclude the works of this thesis. The design of this apparatus comes with a number of challenges, some of which are still in the process of being solved. We will explore some of these challenges and the current solutions in the works so that we may look forward to the future development of the apparatus. Once these final challenges have been overcome, the apparatus will not only be used to study a variety of interesting samples, but will also face further modifications towards becoming capable

of studying an even wider variety of phenomena.

1.3 A Brief History of Magnetism

Likely, the first magnets used were lodestones. A lodestone is a stone containing magnetite, theorized to have been magnetized by lightning striking the stone, generating a strong magnetic field and ordering the spins of the ferrimagnet leading to its behaviour as a seemingly permanent magnet. In China, well before the eleventh century it had been noted that a long piece of lodestone, left suspended, will always orient itself to point North-South, aligning with the Earth's magnetic field [10]. The discovery of the self-aligning piece of lodestone was responsible for the development of the first magnetic device, the compass.

In the year 1600 William Gilbert published his book *De Magnete*, detailing some of the early rigorous studies of magnetism following what's closer to the scientific methods we use today. In his book, Gilbert detailed the first demonstration of magnetic fields. Gilbert placed a number of small iron wires on the surface of a strong spherical lodestone and observed how they stood upright everywhere except at the magnetic equator of the stone where they lay flat [11, 12].

An analogy between magnetism and electricity can be clearly drawn, however the manner through which these phenomena are linked mystified scientists for ages. Yet, it was not until 1820 when Hans-Christian Oersted was able to show the generation of a magnetic field around a charge carrying wire, linking magnetism and electricity for the first time [13]. This was then quickly developed into the solenoid, able to generate a uniform magnetic field proportional to the number of turns of wires and the current passing through them, leading to a huge revolution in the field of magnetism [2]. Suddenly, scientists were able to generate a magnetic field of controllable magnitude.

From the year 1820 on, developments in the study of magnetism and electricity began to occur more rapidly. In 1845 Michael Faraday published his paper describing how light and magnetism interact through what is now known as the magneto-optic Faraday Effect. Following Faraday's experimental work, James Clerk Maxwell proceeded to describe the observed phenomena mathematically. The famous Maxwell equations were first published in 1864 [14].

From Faraday's demonstration of the alteration of light when passing through a slab of glass held between the poles of a magnet [15, 16], John Kerr became convinced that light reflected off of a magnetic surface should also experience a change in polarization. The Kerr effect, as we now know it, was published for the first time in discussions by John Kerr in 1877 and 1878 [17, 18].

Jumping ahead to the 1900's, magnetic and electric fields in space are now relatively understood, however, there still exists no satisfying explanation for the existence of a ferromagnet. The classical picture of moving charges generating a magnetic field as the only explanation for magnetism leaves much to be desired. If moving charge were the only explanation for magnetic fields, a ferromagnet with a non-zero net magnetization at room temperature would require a large current to travel around the surface of the sample perpetually. In 1907 Pierre Weiss proposed a molecular field theory which required a magnetic field within the sample parallel to the magnetization, but stronger by three orders of magnitude [2, 19].

Weiss considered how elementary magnets in a ferromagnet behave to generate a spontaneous magnetization [19,20]. In his works, Weiss considers a magnetic field inside the ferromagnet resulting from the magnetic dipoles (electrons) of which it is made such that the total field inside the material is the sum of the internally generated magnetic field and any applied field [21]. The orientation of the dipoles is then determined by both the internal and external magnetic fields. This description for a ferromagnet seemed unlikely at a time before quantum mechanics as Maxwell's equations required the magnetic field be continuous and no field so strong had been detected.

It was in 1925 when Weiss's molecular field theory began to truly come together. George Uhlenbeck and Samuel Goudsmit discovered that electrons seem to have an associated quantized angular momentum now known as spin.

In 1929 Werner Heisenberg developed a Hamiltonian describing the manor in which two neighboring spins interact with one another to generate this Weiss field. The interaction is called the exchange interaction and is governed by the Pauli exclusion principle which dictates that no two electrons within an atom can have the same quantum numbers.

It is from the Weiss molecular field and the exchange interaction that modern magnetism is born. These demonstrate clearly the quantum mechanical nature of magnetism and it is from here that we may begin to investigate modern models of magnetic systems and their dynamics.

It is of interest to note that, within the development of magnetism, often the experimental work and commercial demands lead the theoretical explanation. Not only are observations often leading theory, but the field as we know it today is still young. The quantum mechanical explanation was developed within the last hundred years and measurements on the pico- and femtosecond timescales have only been completed within the last 31 years. There is still a large push for further development of experimental techniques to develop the understanding of magneto-dynamics, and one can expect these innovations will lead to the field looking quite different within another 30 years.

In this chapter we have worked to understand how our present understanding of magnetism has developed over time. Starting from this spring-board, in the chapter to follow let us work out a mathematical understanding of the dynamic processes of interest which may be studied with the unique TR-MOKE magnetometer developed for this project.

Chapter 2

Magnetic Motivation and Theory

We will begin this work by laying down the appropriate theoretical foundation for the magneto-dynamics which this apparatus will study. In this chapter, we will begin by describing a simple static model of magnetism before expanding into a description of some relevant magneto-dynamic phenomena. Effects resulting from the angular momentum of an incident laser beam as well as from ultrafast heating will be explored theoretically. From the study of many dynamic processes which can be studied using TR-MOKE, we will wrap up the chapter discussing the magneto-optic Kerr effect in order to understand how these magneto-dynamic phenomena are observed.

2.1 Origins of Magnetism

As mentioned in chapter 1.3, the existence of a permanent magnet cannot be described using only classical mechanics. This is because the only classical description is through moving charges generating a magnetic field, however, without moving charges in a permanent magnet, the classical description stops short.

The magnetization of a system is dictated by the quantized angular momentum of its electrons. We then must understand the general behaviour of these electrons alongside the ways in which they interact in order to begin to properly describe a magnetic sample.

Working from the relativistic Dirac equation, taking into account symmetry requirements, the Hamiltonian describing the magnetic behaviour of an electron is

$$\mathscr{H} = \frac{1}{2m}\left(\boldsymbol{p} - \frac{e}{c}\boldsymbol{A}\right)^2 + e\phi - \frac{e\hbar}{2mc}\boldsymbol{\sigma}\cdot\boldsymbol{H} + \zeta\boldsymbol{l}\cdot\boldsymbol{\sigma}, \tag{2.1}$$

where a spin-orbit term has been defined as

$$\zeta = \frac{e\hbar^2}{4m^2c^2}\frac{1}{r}\frac{\partial V(r)}{\partial r}. \tag{2.2}$$

Here, m is the mass of the electron, $\boldsymbol{p}$ is the momentum, e is the charge of the electron, c is the speed of light, $\boldsymbol{A}$ is the magnetic vector potential, ϕ is the magnetic scalar potential, $\boldsymbol{\sigma}$ is the intrinsic spin of the electron, $\boldsymbol{H}$ is the external magnetic field, $\boldsymbol{l}$ is the electrons orbital momentum, and $V(r)$ is the electronic scalar potential with respect to distance r from the nucleus, where the electron cloud is taken to be spherically symmetric. The final term in this Hamiltonian describes how the spin of the electron interacts with the field generated by the electron's orbit, and the second to last term describes how the spin of the electron interacts with the external magnetic field [22].

While the terms describing the coupling of a spin to its own orbit or the external field can lead to large magnetic responses, there are more interactions at play to consider as well. We must discuss the ways in which spins interact. We now turn our attention to the Heisenberg Hamiltonian for interacting spins $\boldsymbol{S_i}$ and $\boldsymbol{S_j}$

$$\mathscr{H} = -\frac{1}{2}\sum_{\langle i,j\rangle} J_{i,j}\boldsymbol{S_i}\cdot\boldsymbol{S_j}, \tag{2.3}$$

where J is the exchange constant [23]. If $J_{i,j}$ is positive, the interacting spins will favor parallel alignment and if $J_{i,j}$ is negative the preferred alignment will be anti-parallel [24]. The influence of electrons from separate ions on one another is described as an exchange interaction [25]. When two electrons are in conductors directly next to one another this is called direct exchange. Should an insulator such as Oxygen be present between the conducting ions, the electrons of the conductors may still interact with one another, this interaction is called super exchange [26]. Direct exchange describes the hopping between d-orbitals of transition-metals which are highly localized. The super exchange interaction is more common in transition-metal oxides where the oxygen molecules lead to larger distances between d-orbitals of the metals, then the magnetization of such a system is the result of electrons hopping via in the intermediate p-orbitals of the conductors [27].

Through the shift from classical to quantum mechanics we have now developed the beginning work towards understanding how magnetism arises in materials. We have developed expressions to describe the magnetic nature of a single electron in a field, how the electron interacts with the field generated by its own motion, and an expression to describe how the electrons of a system influence one another. The next step is to begin to use these tools to describe real systems, however this is not quite so simple in practice. The descriptions provided so far can reasonably be worked with for a system consisting of only a few atoms, however, as the system gets larger the many-body problem becomes unreasonable to work with as one must account for the interactions between every single electron in the system. A simpler approach

is to apply a mean-field approximation where a semi-classical model allows for the treatment of an effective field within the sample as opposed to treating the interactions between each spin independently. The section to follow will detail a semi-classical model of a magnetic sample in order to approximate the phenomena observed through experimental works [9].

2.2 Static Micromagnetics

Throughout this section we will work to develop an energy equation to describe many of the phenomena that take place within a static micromagnetic sample. The working energy equation is:

$$W = W_{\text{exchange}} + W_{\text{anisotropy}} + W_{\text{demagnetize}} + W_{\text{external}}. \tag{2.4}$$

We will break down a qualitative description of each term in order to understand many of the effects observed through experiment, beginning with the previously discussed exchange interaction.

2.2.1 The Exchange Interaction

Taking a localized picture of the exchange interaction and treating the discrete properties of a magnetic sample as continuous, including vectors and space, the Heisenberg Hamiltonian from equation 2.3 can be rewritten as

$$\mathscr{H} = -JS^2 \sum_{\text{neighbors}} \cos(\phi_{i,j}). \tag{2.5}$$

Applying the small angle approximation such that $\phi_{i,j} \approx 1 - \frac{1}{2}\phi^2$ and taking the sample to have cubic symmetry, we may write

$$\phi_{ij} \approx \left|\vec{m}_i - \vec{m}_j\right|^2 \approx \left|\vec{r_{i,j}} \cdot \vec{\nabla} m\right|^2 \approx \nabla m_x^2 + \nabla m_y^2 + \nabla m_z^2. \tag{2.6}$$

The exchange energy density then takes the form

$$W_{\text{ex}} = \frac{JS^2}{a} k_{\text{neighbor}} \left[\nabla m_x^2 + \nabla m_y^2 + \nabla m_z^2\right], \tag{2.7}$$

where k_{neighbor} is the number of nearest neighbors depending on the crystal lattice of a sample. Of note is that the coefficient $\frac{JS^2}{a} k_{\text{neighbor}}$ is often called the stiffness constant A. For a given material A will often be quoted for both a crystalline and polycrystalline value [9].

2.2.2 Magnetic Anisotropy

The next term in equation 2.4 is the anisotropy energy. Anisotropy describes the magnetic density distribution over as well as electrons spin-orbit coupling. Anisotropy comes in two forms, shape and crystalline. The crystalline anisotropy stems from the distribution of electrons within the crystal structure of a sample, whereas the shape anisotropy results from the samples overall shape. Examples of samples with a significant shape anisotropy include nanowires and thin films, where a spherical nanoparticle might have a near zero shape anisotropy. Whether the anisotropy of a sample results from the crystal structure or the shape, the result is one axis where the sample may be more easily magnetized (the easy axis) than the other axis (the hard axis).

The anisotropy energy of a sample with a simple cubic symmetry takes the form

$$W_{\text{cubic}} = K(\alpha_x\alpha_y + \alpha_y\alpha_z + \alpha_z\alpha_x) \tag{2.8}$$

where K is the anisotropy constant and the α terms are the direction cosines from the crystal lattice.

2.2.3 Zeeman Energy

The remaining two terms in equation 2.4 are the result of the spin coupling to a magnetic field H. This Zeeman energy can be split into two components, the first of which is the external field applied to a sample

$$W_{\text{external}} = -\int \boldsymbol{M}\cdot\boldsymbol{H}. \tag{2.9}$$

The other, the demagnetizing energy which is the internal magnetic field acting on a spin, generated by all of the other spins that make up the sample. This demagnetizing energy works to minimize free spins on the surface of the sample and describes the dipole-dipole interaction between spins. The demagnetizing energy is written as

$$W_{\text{demagnetize}} = -\frac{1}{2}\int \boldsymbol{M}\cdot\boldsymbol{H}_{\text{demagnetize}}. \tag{2.10}$$

This demagnetizing field is non-trivial to calculate as the effect on one spin requires knowledge of the orientation of every other spin in the system. It is possible to calculate the demagnetizing field for the infinite cylinder, infinite layer, or a uniformly magnetized ellipsoid, and much more involved for most non-uniform systems [9].

It is through the demagnetizing field that domains are born. There is an energy loss associated with the dipolar field. When the magnetization reaches a boundary, such as the edge of a magnetic sample, the field diverges, costing an energy of $B^2/2\mu_0$ Joules

per cubic meter where B is the magnetic field and μ_0 is the permeability of free space. The energy cost associated with the formation of a domain wall creating a boundary between two regions of different magnetization, costs an energy $E = -2JS^2 cos\theta$, where θ is the angle between two neighboring spins. The formation of domain walls, then, is a matter of minimizing the energy of a system. Should a sample be small enough a single domain may be present with no walls, this is the case for many nanoparticles [24].

Now that we have built out an understanding of the basic systems at play to allow for magnetization, we may begin to expand the discussion to include dynamics.

2.3 Dynamic Magnetism

The static system defined in the previous section must be expanded to a dynamic description in order to transition into the discussion of the time-resolved phenomena which this research aims to study. Beginning by defining the energy density $w = W/\text{Volume}$ where W is the energy from equation 2.4 [9]. The effective field is then

$$H_{\text{eff}} = -\frac{dw}{d\boldsymbol{M}}. \tag{2.11}$$

The equation of motion of the dynamic system is now

$$\frac{d\boldsymbol{M}}{dt} = -\gamma \boldsymbol{M} \times \boldsymbol{H}_{\text{eff}} + \boldsymbol{R}(\boldsymbol{M}, \boldsymbol{H}), \tag{2.12}$$

where γ is the gyromagnetic ratio and $\boldsymbol{R}$ is the damping term. The gyromagnetic ratio is

$$\gamma = \frac{g|e|}{(2mc)}, \tag{2.13}$$

where g is the spectroscopic splitting factor, which is typically taken to be $g = 2$ for the free electron case as well as 3d transition metal ferromagnets such as Permalloy.

When an external field is applied to a sample, the motion taken in the relaxation of the spins towards alignment with the field will appear different depending on the form of the damping term. The initial damping term suggested by Landau and Lifshitz takes the form

$$\boldsymbol{R} = -\frac{\lambda}{M_s^2} \boldsymbol{M} \times (\boldsymbol{M} \times \boldsymbol{H}_{\text{eff}}), \tag{2.14}$$

where λ is a damping parameter and M_s is the saturation magnetization [28]. This damping term allows that the magnitude of the magnetization does not change in

length, however is only applicable for the low damping case. For the high damping case, this form leads to rapid motion of the magnetization and so this form is considered nonphysical for the high damping case.

Another form for the damping term was suggested by Gilbert using a Lagrangian approach [29,30]. The damping term suggested by Gilbert was:

$$\boldsymbol{R} = -\frac{\alpha}{M_s}\boldsymbol{M} \times \frac{d\boldsymbol{M}}{dt}, \tag{2.15}$$

where α is a dimensionless damping parameter. The spin motion described by Gilbert's damping term now goes to zero as the damping parameter becomes large. Equation 2.12 now looks like

$$\frac{d\boldsymbol{M}}{dt} = -\gamma\left(\boldsymbol{M} \times \frac{\delta w}{\delta \boldsymbol{M}}\right) - \frac{\alpha}{M_s}\left(\boldsymbol{M} \times \frac{d\boldsymbol{M}}{dt}\right), \tag{2.16}$$

which is known as the Landau-Lifshitz-Gilbert equation. The LLG equation is fundamental in applied magnetism and is the equation on which many dynamic micromagnetic simulations are based [31].

Now that we have developed an understanding of the equations governing magneto-dynamics, we will look into the phenomena that allow the magnetization of a sample to change under an applied magnetic field. We will begin with the discussion of the result of a moderate field, before discussing the high field case.

When Landau and Lifshitz developed the equation of motion for a magneto-dynamic system and made their first suggestion for a damping parameter, their goal was actually to determine the velocity of domain wall motion. When an external magnetic field is applied to a sample with multiple domains, the domains already pointing in the same direction as the applied field will begin to expand as depicted in figure 2.1.

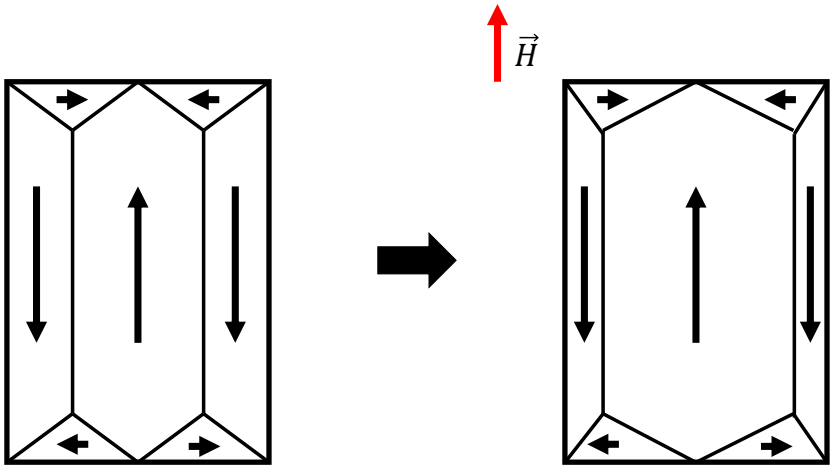

Figure 2.1: A sketch of the domain wall motion from an applied magnetic field. [28] [24]

The equation describing the velocity of the domain wall motion is

$$v = \mu_w(H - B), \tag{2.17}$$

where μ_w is the mobility, H describes the applied magnetic field and B is the magnetic field offset as described by the coercivity of the sample. The mobility includes all of the damping parameters and can be written as

$$\mu_w = \frac{2\gamma^2 M_s}{g}\sqrt{\frac{A}{K}}. \tag{2.18}$$

Taking domain wall motion to the 1D case, the velocity is then written as

$$v = \frac{\gamma\Delta}{\alpha}H, \tag{2.19}$$

where Δ is the width of the domain wall described by

$$\Delta = \sqrt{\frac{A}{K_u}}, \tag{2.20}$$

A is the exchange constant and K_u is the uniaxial anisotropy. The domain wall is made up of spins at angles that transition from one domain to the next. These spins are described as the domain wall and the width essentially is described by the number of spins in this transition from one domain to the next. The velocity of a domain wall is not able to increase to infinity with increasing field, the maximum velocity is

$$v_w = 2\pi\gamma\Delta M_s. \tag{2.21}$$

The maximum velocity of a domain wall has an associated critical field

$$H_{\text{crit}} = 2\pi\alpha M_s, \tag{2.22}$$

which generates the rapid motion. Applied fields larger than this critical value lead to a phenomena known as magnetic switching. This occurs on ultrafast timescales and brings us to our next section.

2.4 Ultrafast Dynamics

Our discussion of the dynamics of magnetic systems has rapidly brought us to the realm of ultrafast phenomena. In this section we will continue the focus on magneto-dynamics through specific phenomena of notable interest in the modern day.

2.4.1 Switching

We begin this section by restating a question. What happens to a sample if a field is applied much greater than the critical field? What occurs in the case where an ultra-fast magnetic field is applied such that the domain wall motion is too slow to respond to the field? The answer to these questions is magnetic switching. The phenomenon of switching was observed in the 1950s resulting from commercial pressures to develop early versions of a magnetic memory array [32].

Should material be deposited in a film so thin, it can only be single domain, as a large magnetic field is applied, domain wall motion cannot be the explanation for a change in magnetization direction. Instead, the domain itself rotates to align along the direction of magnetic field. The phenomenon of switching was observed by both Blois and Conger in 1955, doing just this with a thin film of permalloy [33, 34].

From equation 2.17 it is clear that, up to the critical field, the velocity of domain wall motion is proportional to the applied field H. The time taken for switching by the motion of a domain wall is then

$$\tau^{-1} = S_w^{-1}(H - B), \tag{2.23}$$

where S_w is a switching coefficient. The switching coefficient is taken to have many forms depending on different models. Many of the different models, as well as their accompanying results are discussed thoroughly in reference [9].

The study of magnetic switching is a popular field today. Investigations into all-optical magnetic switching are commonly done using the Faraday or Kerr effect. For some recent examples, the reader may turn to references [35–37].

From this qualitative discussion of magnetic switching, we will transition into other ultrafast phenomena from which switching occasionally results.

2.4.2 The Inverse Faraday Effect

In 1936, Richard A Beth proved that circularly polarized light has an angular momentum [38]. Beth found by passing light through a series of half-wave plates, that the plate actually acquired an angular momentum related to the flux of photons passing through it [39]. As spin is a description of quantized angular momentum, it is then reasonable to expect that the circularly polarized light passing through a magnetic material should influence the magnetization. This expectation follows reasonably from Beth's discovery in 1936, and can be seen clearly through the experimental work of Kimel in 2005 [40, 41]. The effect of polarized light on the magnetization of a sample is called the Inverse Faraday Effect, often shortened to IFE.

The Faraday effect, as stated by Kimel, describes the rotation of the polarization of light after it has been transmitted through a magnetic medium as

$$\alpha_F = \frac{\chi}{n} \boldsymbol{M} \cdot \boldsymbol{k}, \tag{2.24}$$

where α_F is the Faraday rotation, χ is the magnetic susceptibility, n is the index of refraction, $\boldsymbol{M}$ is the magnetization, and $\boldsymbol{k}$ is the wave vector [40]. The inverse Faraday effect describes the static magnetization induced in a sample by high intensity laser radiation:

$$\boldsymbol{M}(0) = \frac{\chi}{16\pi} [\boldsymbol{E}(\omega) \times \boldsymbol{E}^*(\omega)], \tag{2.25}$$

where E and E^* are the electric field and it's complex conjugate respectively, and ω is the frequency of the incident light. The inverse Faraday effect does not require any absorption of light, so the effect is essentially instantaneous, occurring over femtosecond time-scales. An ultrafast circularly polarized beam of sufficient intensity will then be capable of exciting a sample sufficiently to cause magnetic switching with no thermal excitation, leading to switching on timescales nearly as short as the pulse of the laser.

This section has aimed to provide a qualitative description of the inverse Faraday effect as the study of this effect is one of interest with the dual-delay line TR-MOKE apparatus. For a detailed break-down of the mathematics describing the Faraday effect and the inverse Faraday effect, one may turn to reference [42] where Battiato et al. derive the lengthy equations rigorously using quantum mechanics.

2.4.3 Ultrafast Demagnetization

Another phenomena which occurs over the time scales of interest in this chapter is ultrafast demagnetization. This phenomena has a controversial history, where many of the papers contradict one another as, from the time of its discovery, it took roughly 20 years to properly explain the observation.

In 1996, Beaurepaire observed the first instance of ultrafast demagnetization using a 60 fs laser pulse [43]. Beaurepaire observed demagnetization in a Nickel thin film on sub-picosecond time scales with additional electron and spin dynamics occurring over the next 5 ps to follow the initial demagnetization. From these results, Beaurepaire suggested a phenomenological treatment of the sample as if it had three thermalized reservoirs, an electron system at temperature T_e, a spin system of temperature T_s, and a lattice (or phonon) temperature of T_l. The evolution of the system could then be described as three coupled differential equations:

$$\begin{aligned} C_e(T_e)\frac{dT_e}{dt} &= -G_{e,l}(T_e - T_l) - G_{e,s}(T_e - T_s) + P(t) \\ C_s(T_s)\frac{dT_s}{dt} &= -G_{e,s}(T_s - T_e) - G_{s,l}(T_s - T_l) \\ C_l(T_l)\frac{dT_l}{dt} &= -G_{e,l}(T_l - T_e) - G_{s,l}(T_l - T_s), \end{aligned} \tag{2.26}$$

where C_e is the electron specific heat, C_s and C_l are the spin and lattice contributions to specific heat respectively. $G_{e,l}$, $G_{e,s}$, and $G_{s,l}$ represent the electron-lattice, electron-spin, and spin-lattice interaction constants respectively. This model allows G to represent the energy transfer from one reservoir to the next and P(t) represents the laser power, which is only applied to the electronic term as it is assumed all of the energy transfer initially goes through the "electron reservoir". Within the Ni sample studied by Beaurepaire, this phenomenological picture then describes the laser transferring energy to the electron reservoir which heats up and begins to cool with an exponential decay curve with a characteristic time of around 1 ps. The spin reservoir, however has a delayed peak in temperature after approximately 2 ps and then follows a similar decay pattern to the electron heating. Beaurepaire, and many to follow, assumes that the demagnetization occurs too quickly for the energy to transfer to the crystal lattice based off of the observed data.

In the year 2000, Zang and Hübner suggested that the ultrafast demagnetization demonstrated by Beaurepaire and others was the result of the field generated by the laser interacting with the spin-orbit coupling of the magnetic sample [44]. Zang and Hübner begin by arguing that it is the spin-orbit coupling which allows for an alteration of the magnetic moment, such that, without this term, even under the application of a laser field, there is no spin relaxation. Through their theoretical analysis of a sample consisting of a single layer of Nickel, they found that the expected demagnetization time should be in the neighborhood of 50 fs.

In a review of ultrafast demagnetization in Nickel, Dalla Longa et al. attempts to investigate the many papers published describing this ultrafast demagnetization in order to determine the importance of pump helicity (the handedness and degree of ellipicity of the polarization of the beam) on the demagnetizing effects [45]. It is noted that the pump helicity is important in garnets, where the inverse Faraday effect leads to the application of a torque on the magnetization vector, however, it appears that this is not in fact the case for transition metals. Dalla Longa et al. find that, while the helicity appears to have an effect over short time scales on the samples, the demagnetization time scale and the final demagnetized state are not altered by the helicity of the light.

Eventually, in 2013 Eschenlohr et al. found that direct irradiation from a laser beam was not necessary to cause ultrafast demagnetization. Eschenlohr et al. studied a nickel,

gold multilayer where the gold was used as a capping layer [46]. Their findings were that, as a result of the observed ultrafast demagnetization, spin-flip mechanisms induced through the spin-laser field interaction could not be responsible. The laser interacting with the topical gold layer will result in heating of the layer, which will eventually heat the nickel after a the heating has propagated through the gold layer at the speed of sound over a few picoseconds.

The findings of Eschenlohr et al. are that the ultrafast demagnetization is a transport effect, where spins are displaced out of the magnetic layer on the femtosecond timescale. Thermal effects then proceed to take place over picosecond timescales to follow, where spin diffusion and spin-flip scattering lead to a magnetic relaxation, and eventually a re-magnetization. This result is further supported by Vodungbo et al. in 2016 where they followed a similar procedure with a Cobalt Palladium multilayer capped with Aluminum [47].

The historical trajectory of ultrafast demagnetization highlights the complexity of explaining emergent phenomena. The effect, now understood to be transport based, occur over tens to hundreds of femtoseconds. These timescales for such a strong effect make it of high interest within the study of magnetism today.

2.4.4 All-Optical Switching (AOS)

Now that we've developed a qualitative understanding of some ultrafast phenomena, we return to the discussion of switching. All-optical switching is simply the switching of a magnetic sample using only light. For industry applications, AOS will ideally occur over ultrashort timescales (tens to hundreds of femtoseconds), have a low threshold for control power, high efficiency, and be on the nanoscale. These are the pillars that then define many of the materials investigated for AOS [48].

In 2007 it was found that GdFeCo alloys may experience AOS through a single circularly polarized laser pulse [7]. This appeared to be a result of both thermal effects, as well as the helicity of the laser beam. GdFeCo alloys have since appeared to be able to undergo AOS in an entirely helicity independent case, while ferrimagnetic CoTb and ferromagnetic thin films such as Co/Pt multilaysers demonstrate helicity dependent AOS [49].

Quessab et al. determined through review and research that AOS may be obtained for Co/Pt multilayers where the helicity of light is in the most absorbent state according to magnetic circular dichroism (MCD), where MCD describes the helicity dependence of the absorption coefficient of the material [50].

We have now discussed many of the ultrafast phenomena associated with some of the samples which are intended to be the initial targets of study of this apparatus.

Phenomena resulting from heating may be studied using a linearly polarized beam to pump a magnetic sample. By simply adding a quarter waveplate to the pump the polarization of the beam can be converted to circularly polarized, thus allowing for the study of the inverse Faraday effect. In the section to follow, let us turn our attention to phenomena which occur over much longer timescales.

2.5 Spin Waves

Returning to the semi-classical model outlined in chapter 2.2, we take a look at the description of a precessing spin. A spin wave can then be imagined as a series of precessing spins next to one another with a linear difference in the phase. This picture can be seen more clearly through figure 2.2.

By adding in the consideration of a number of frequency components leading to a wave packet, the spin waves can then be described as a sort of particle propagating through a material with an effective mass

$$m = \frac{\hbar^2}{2Ja^2}, \tag{2.27}$$

where J is the exchange interaction between neighboring spins and a is the distance between spins defined by the crystal lattice [25]. The spin wave dispersion relation can be derived by again looking to the Heisenberg Hamiltonian, this time expressed as

$$\mathscr{H} = \sum_k \epsilon_k n_k, \tag{2.28}$$

with energy

$$\epsilon_k = \left(\frac{2\gamma\hbar A}{M_s}\right) k^2 + \gamma\hbar H_0, \tag{2.29}$$

where n_k represents the number of magnons [9]. One could alternatively find spin waves through the Holstein-Primakoff Hamiltonian [52] where magnons come out of the theory as the quasi-particle responsible for flipped magnetization. The Holstein-Primakoff Hamiltonian can be written as

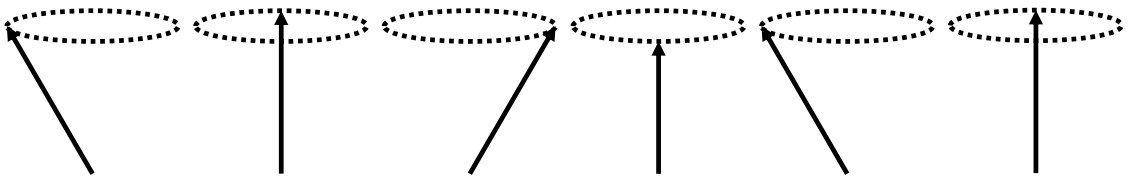

Figure 2.2: A sketch representing a spin wave, remade from [51].

$$\mathcal{H} = \sum_k (\hbar\omega_k)\alpha_k^\dagger \alpha_k, \tag{2.30}$$

where α_k and $\alpha_k^\dagger$ are the creation and annihilation operators. Here, the details are mostly hidden in the frequency

$$\omega_k = \begin{cases} \sqrt{(\gamma H_i + N_x\omega_M)(\gamma H_i + N_y\omega_M)} & k = 0 \\ \sqrt{\left[\gamma H_i + 2zJS(1-\gamma_k)\right]\left[\gamma H_i + 2zJS(1-\gamma_k) + \omega_M sin^2\theta_k\right]} & k \neq 0 \end{cases}, \tag{2.31}$$

where

$$H_i = H_0 - 4\pi N_z M \qquad \omega_M = 4\pi\gamma M_s \qquad \gamma_k = \frac{1}{z}\sum_\delta e^{ik\cdot\delta}, \tag{2.32}$$

J is the exchange constant for spins S, H_0 is the external field, z is the number of nearest neighbors, N_z is the demagnetizing factor due to shape in a given direction, and the angle θ_k is the spherical coordinate. It can be shown that for the case where k approaches zero, the result in equation 2.29 is reproduced.

Both of these methods of mathematically demonstrating the existence of spin waves must make small angle approximations for the validity of the results. This means that they may be a good proof of concept, but for large angle rotations, numerical simulation are still necessary.

From equation 2.31, we note that the spin-wave frequencies are lowest for $\theta_k \to 0°$, or when propagating through the symmetry axis, and largest for $\theta = 90°$, where the wave propagates perpendicular to the symmetry axis.

In 1948, Kittel derived the resonance frequency for a spin wave to be

$$\omega_0 = \gamma\sqrt{BH_0}, \tag{2.33}$$

for a frequency oscillation in a plane surface where γ is the magneto-mechanical ratio for an electron, H is the static magnetic field strength, and B is the magnetic induction in the sample [53].

From the formulations described above, fast and slow frequency spin waves may be understood to some degree. The conclusion of this section is that the equations can give an overview of the expectations of spin waves, however, due to the complexity of the phenomenon, they are typically insufficient to describe in a complete sense the effects observed in a lab environment, which once again require numerical simulation. Spin-waves themselves are a result of phase differences between precessing neighboring spins, and are used (like all of the other effects described) to reduce the energy of the

system.

For a more detailed analysis of spin waves, the reader may turn to reference [51]. Additionally Magnonics by Demokritov and Salvin provides a compilation of relevant reading for a good indication of the current state of magnonic research [54]. Due to the sheer size of the field, it would be an onerous task to highlight the current status of spin-wave research in the modern day. This chapter aims to provide enough information on the basics of spin waves that we may build on in more detail for specific cases in chapter 2.6.

2.6 Samples of Interest

The aim of this chapter thus far has been to develop an understanding of both static and dynamic magnetism to motivate the development of an apparatus capable of observing ultrafast phenomena, as well as slow phenomena occurring over nanosecond time scales. In this section we will briefly discuss some of the first targets of this apparatus now that we have the knowledge to predict some of their expected dynamic behaviour.

2.6.1 Permalloy

Thin film Permalloy has been studied extensively over the years using TR-MOKE. In Heibert's 2001 PhD thesis, he finds long time relaxation of the magnetization of thin film Permalloy samples of varying composition (referring to the ratio of Iron to Nickel) with relaxation occurring over 2 ns following the 10 ns excitation [9].

In his work, Hiebert found in a large-field regimen that the thin film Permalloy after excitation experienced the formation of a domain, followed by the rotation of the domain, as described by the magnetic switching in chapter 2.4.1.

Due to the highly reported GHz frequency excitation in Permalloy this sample is a good candidate for initial study [55]. Following the confirmation of expected long range excitations indicating spin wave propagation, we may investigate Permalloy multi-layers where different dynamics may be observed.

2.6.2 Pt/Co Multilayers

As we've discussed earlier in this chapter, Pt/Co multilayers present interest in the development of our understanding of all-optical switching. We have access to a number of samples of Pt/Co multilayers of various thickness and ratios which may be studied using ultrafast heating with a linearly polarized beam. This apparatus also has the ability to study samples using a circularly polarized pump, so studies of the helicity

dependance over short time scales to attempt to reproduce results presented by the likes of Ganping and Beaurepaire will be possible [56, 57]. Both of these papers found demagnetizing events occurring faster than one picosecond.

Upon the completion of the apparatus developed throughout this work, we will be capable of observing these same demagnetizing events occurring over less than 100 fs and should be able to observe the full magnetic recovery to the initial state. Both Ganping and Beaurepaire were able to observe the demagnetization, but did not have sufficient delays to observe magnetic recovery, as they were limited by time scales of a maximum of 60 ps. with access to a delay line capable of observing over 10 ns of delay, the apparatus developed through this work should be able to observe the process of magnetic recovery for these interesting samples through both direct heating and helicity dependent measurements.

2.6.3 Permalloy on Cobalt Oxide

With Permalloy's long time scale spin waves and Cobalt oxide's ultrafast demagnetization, this multilayer material may be a candidate material which offers both short and long range dynamics. The interest with this sample lays in the interaction between the Permalloy and Cobalt oxide layers and how the interaction presents dynamically.

2.6.4 $\epsilon - Fe_2O_3$ Nanoparticles

The study of nanoparticles is of interest as, due to the high surface-to-volume ratio of smaller nanoparticles magnetic switching is more likely to occur. $\epsilon - Fe_2O_3$ nanoparticles have only been synthesized in their pure form within the last 25 years. These are the least studied of the Fe_2O_3 polymorphs due to the difficulty in generating these metastable nanoparticles. The ϵ phase exists only in nanoparticle form and requires a specific heating regime to transform from the precursor into this phase. These nanoparticles are known to have a very large coercivity and a relatively small saturation magnetization. Due to their relatively recent development and unusually large coercivity [58], they are of interest to study with the apparatus developed for this thesis.

The study of these nanoparticles presents some challenges that this experiment should be capable of accommodating. For one, the low magnetization of the $\epsilon - Fe_2O_3$ nanoparticles does present a challenge in that they will likely only present a small rotation in the magnetization. So long as the signal to noise is good, this may require a large amount of averaging but it should be possible to measure the change. Both the small size of the nanoparticles leading to single domain and thus the expectation of observing magnetic switching plus the large coercivity of these nanoparticles suggests

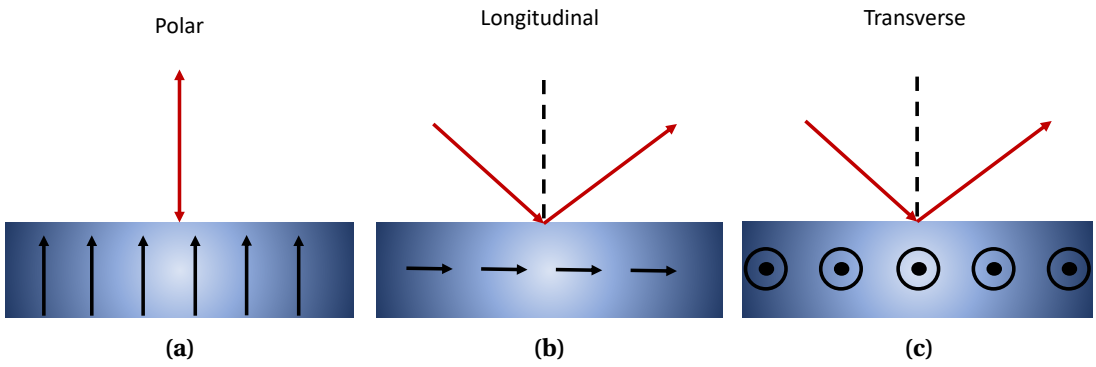

Figure 2.3: The three different geometries of MOKE. The slab representing the sample, the red arrows reflecting off of it representing the laser beam, and the black direction indicates the magnetization of the sample that can be observed from the incident light.

that the demagnetization upon heating should occur over short time scales, but the magnetic recovery could be expected to occur over a longer delay time.

It is noteworthy that the nature of these particles being grain like as opposed to the reflective thin films is also a challenge. While the measurement of these particles has not yet occurred at the time of writing, in later chapters we will discuss the options for mounting particles such as these which allows for the study of a wide variety of samples.

2.7 The Magneto-Optical Kerr Effect

This chapter has presented in detail many of the magneto-dynamic phenomena which incentivize the development of the apparatus through this work. In this section, we will now discuss how the observation of these magnetic alterations may take place through the interaction of light with a magnetic material. The Faraday effect and Kerr effect are discussed interchangeably in the literature at times, however, while the effects are similar, we will proceed to discuss the Faraday effect as a transmission response, while the Kerr effect requires reflection off of a surface.

In 1877, John Kerr originally discussed the rotation of the plane of polarization of light reflecting off of a magnet in the geometry now known as that generating a polar Kerr effect [17]. This theory of the Kerr effect was then expanded the following year when he observed the longitudinal Kerr effect, or the change in plane of polarization of light when reflected off a magnet which itself has a magnetization parallel to the plane of incidence and the surface of the magnet [18, 59]. Since the late 1870's another orientation for observing the Kerr effect emerged, and there are now three distinct geometries of MOKE: polar, longitudinal, and transverse, as depicted in figure 2.3.

In his original papers detailing the Kerr effect, John Kerr did not have the benefits of many modern technologies. In place of the many techniques which can now be used

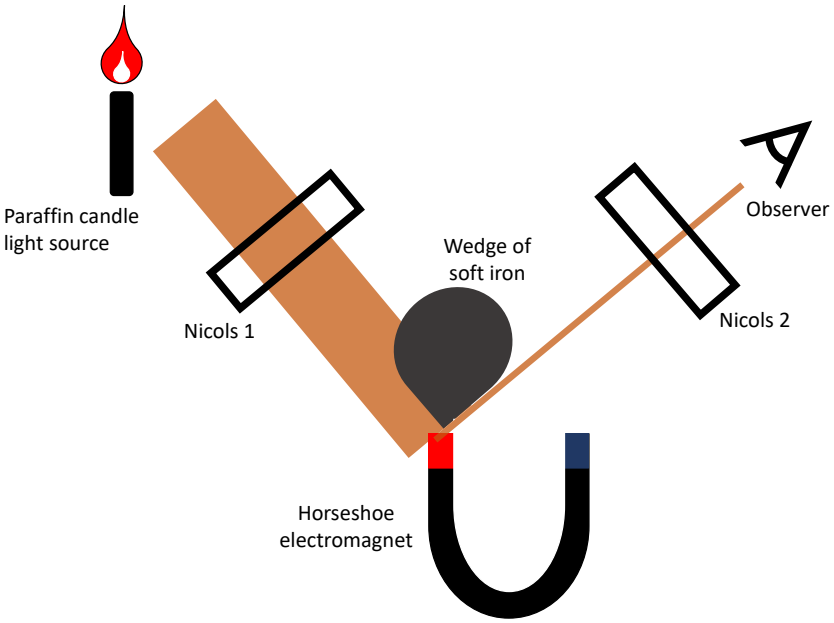

Figure 2.4: A schematic of John Kerr's original Kerr effect experiment where each Nicols was a polarizer rotated to a specific angle to allow passage of one polarization. Inspiration for this sketch came from Kerr's paper [18] and a more modern review of Kerr's work done by P. Weinberger in 2008 [59].

to deposit reflective thin films on appropriate surfaces, or polishing equipment with some degree of automation, Kerr polished the ends of a horseshoe electromagnet by hand to as good a mirror finish as he could get, describing the process as tedious, and made use of the light from a paraffin candle nearby. The light from the candle would first pass through a Nicols polarizer used to pass one orientation of the polarization of light such that the light transmitted was linearly polarized, the light would then reflect off the polished surface of the magnet before it passed through another Nicols polarizer, then to the observer. John Kerr added to this setup a wedge of soft iron to block some of the light near the magnet such that only a slit of light need be observed at the other end. A sketch depicting roughly how Kerr observed the first polar Kerr effect can be seen in figure 2.4.

While Kerr only ventured to present his findings and postulate classically as to how to describe them, we now have a more detailed mathematical understanding of the influence a magnetic sample has on the orientation of the polarization of light. The Kerr effect can be demonstrated mathematically by calculating the reflectance coefficents of light.

The present computation of the reflectance coefficients for the Kerr effect follows from Freiser's derivation [16]. First, we will take the dielectric tensor of a cubic crystal with a spontaneous magnetization to be

$$\boldsymbol{\kappa} = \begin{bmatrix} \kappa_1 & \kappa_2 & 0 \\ -\kappa_2 & \kappa_1 & 0 \\ 0 & 0 & \kappa_3 \end{bmatrix} \tag{2.34}$$

where κ_2 is an odd function of the free space magnetic field $\boldsymbol{H}$ and as a result of magnetization $\boldsymbol{M}$ inside the magnetic sample. Equation 2.34 is often expressed with $\kappa_2 = -i\epsilon Q$ where ϵ is the dielectric constant and Q is the complex magneto-optic parameter containing information about the material and wavelength [60]. From equation 2.34, the first order reflectance (or Fresnel) coefficients can be derived for each of the MOKE geometries described by figure 2.3. In each coefficient, s and p refer to s- or p-polarized light where p-polarized light has the polarization oriented in the plane of incidence, while for s-polarized light the polarization is outside the plane of incidence [16,60]. This is illustrated in the sketch in figure 2.5.

The reflection relations can be described by:

$$\begin{bmatrix} R_p \\ R_s \end{bmatrix} = \begin{bmatrix} r_{pp} & r_{ps} \\ r_{sp} & r_{ss} \end{bmatrix} \begin{bmatrix} I_p \\ I_s \end{bmatrix} \tag{2.35}$$

where $\begin{bmatrix} I_p \\ I_s \end{bmatrix}$ is the incident intensity of the beam [61].

For both the polar and longitudinal case we find:

$$r_{pp} = \frac{n\gamma - \gamma'}{n\gamma + \gamma'} \qquad r_{ss} = \frac{\gamma - n\gamma'}{\gamma + n\gamma'}. \tag{2.36}$$

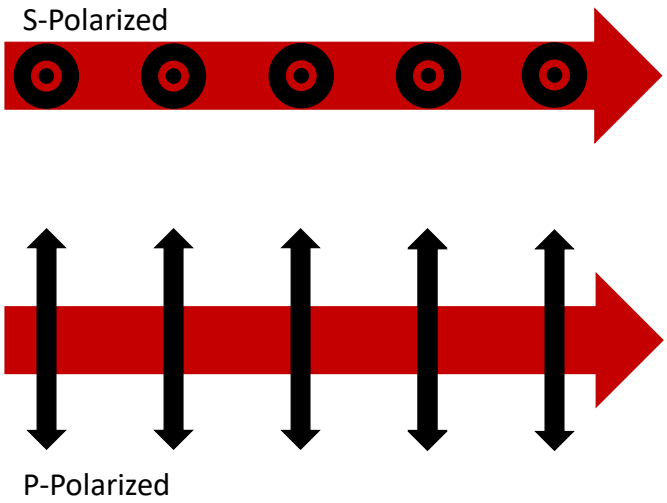

Figure 2.5: A sketch depicting s- and p-polarized light. The red arrows depict the direction of the beam while the black direction indicates the direction of the electric field.

In the polar case, when p-polarized light converts to s-polarized upon reflection (or vice versa), we find:

$$r_{sp} = r_{ps} = \frac{\kappa_2 / n}{(\gamma + n\gamma')(n\gamma + \gamma')}. \tag{2.37}$$

Similarly, the same mixing case for the longitudinal geometry results in coefficients:

$$r_{ps} = -r_{sp} = \frac{\gamma\beta}{n\gamma'} \left[\frac{\kappa_2 / n}{(\gamma + n\gamma')(n\gamma + \gamma'} \right]. \tag{2.38}$$

In the case of transverse MOKE (also known as equatorial MOKE), the reflectance coefficients look quite different, we find:

$$r_{pp} = \frac{n\gamma - 1}{n\gamma + 1} \left\{ 1 + \frac{\sin(2\theta)\kappa_2 / n}{(n\gamma + 1)(n\gamma - 1)} \right\} \tag{2.39}$$

$$r_{ss} = \frac{\gamma - n}{\gamma + n} \tag{2.40}$$

$$r_{sp} = r_{ps} = 0. \tag{2.41}$$

In equations 2.36 through 2.41 we have defined:

$$\gamma = cos\theta \qquad \gamma' = cos\theta' = \sqrt{1 - \frac{sin^2\theta}{n^2}} \qquad \beta = sin\theta$$

for simplicity, where θ is the angle of incidence and n is the index of refraction of the magnetic material.

Since κ_2 is proportional to the magnetization in the reflective material, equations 2.36 through 2.41 can describe well what information is provided through the different geometries of MOKE. Equation 2.36 has no dependence on magnetization and thus, when the polarization of the light doesn't change upon reflection, in the case of polar or longitudinal geometries, the magnetisation of the sample is not probed. However, in equations 2.37 and 2.38 there is a dependence on $\boldsymbol{M}$ (as κ_2 is proportional to $\boldsymbol{M}$) and since κ_2 is understood to typically produce a phase shift [9], the result is elliptically polarized light proportional to the magnetization of the reflective surface.

The transverse MOKE geometry is interesting in that the case where mixing occurs between p- and s- polarization upon reflection yields no result. However, in the case described by equation 2.39, no rotation in the polarization occurs, but instead a small change in intensity and phase.

While all three geometries of MOKE result in a method of measuring the magnetization off of a reflective surface, transverse MOKE is expected to produce the smallest of

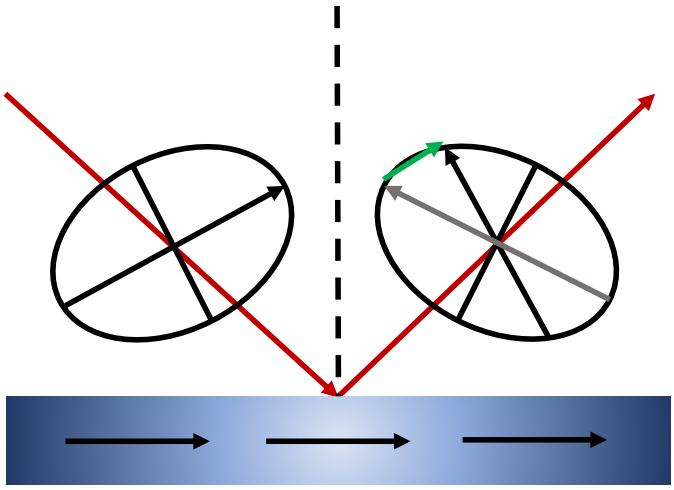

Figure 2.6: A cartoon depiction of the change in angle resulting from the Kerr effect with a longitudinal geometry.

an already weak signal, and thus is out of the running. Polar and Longitudinal MOKE are then the two to choose from and both are attempted at a time in this experiment.

The majority of the work for this thesis is completed using a longitudinal MOKE geometry due to physical restrictions of the setup. In order to perform polar MOKE, the light need be incident at 0° with respect to the surface normal. This requires a beamsplitting cube before the sample, which leads to losses of 50% of the probe power before interacting with the sample, then another 50% of the remaining beam before the detection polarizer. This reduces an already small portion of the laser power down to nearly nothing and limits the ability to detect a signal. For these reasons, a Longitudinal MOKE geometry was chosen as described in figure 2.6.

Chapter 3

Experimental Apparatus

The main goal of this thesis is to develop an apparatus to study the time-resolved magneto-optical Kerr effect using a dual delay line configuration. There are a number of critical points in the project where the chosen optic has a significant impact on the quality of the apparatus and thus, warrants elaboration. In this chapter we will discuss much of the mathematics that describe how the most critical of these optics work as well as how they will be applied. We will additionally begin to explore some of the initial set-up and troubleshooting that must be done in order to develop this apparatus.

We will begin with a description of the pulsed laser applied for this project along with some of the details of its operation. We will then consider many of the optics on table including a Beta Barium Borate (BBO) crystal used to frequency double the beam for the probe, the 2 meter rail along with the modifications and work completed to ensure linearity including the retroreflector which travels along this stage to return light in the direction from which it came. At last, we will explore the details of the magneto-optical Kerr effect, from the polarization optics and setup for the detection of a Kerr rotation, to the initial observation of a DC MOKE measurement. The aim of this chapter is to understand how many of these critical pieces work as well as the reason behind their implementation.

3.1 Laser Specifications

The first system critical to this apparatus is the laser that provides the infrared light source. This project applies a Ytterbium Fiber (Y-Fi) femtosecond laser from KMLABS (later acquired by ThorLabs).This laser has operating modes generating pulses at a frequency of 1 MHz, 3 MHz, 10 MHz, or 60 MHz. This project primarily applies the 10 MHz mode where the laser has an expected 120 fs pulse length and a maximum average power of around 20 W, thus having a maximum pulse energy of about 2 μJ and

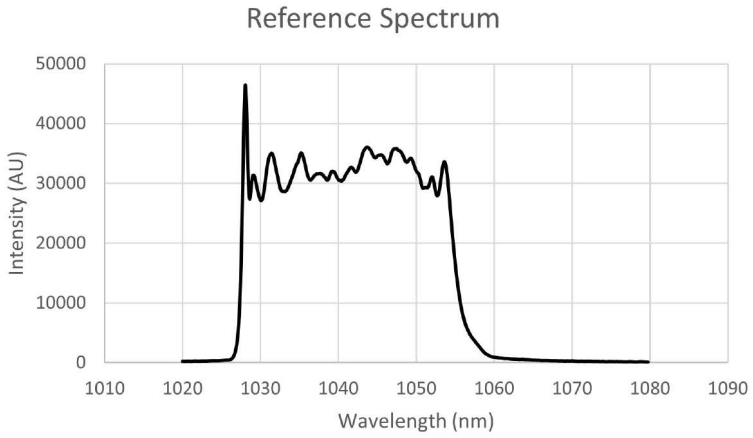

Figure 3.1: The oscillator spectrum applied for this experiment. This spectrum was chosen due to it's high stability with changing laser temperatures and the high intensity near 1030 nm, which leads to higher intensity green light when using a nonlinear BBO crystal.

a maximum peak power of 16.67 MW [62]. The laser spectrum generated throughout this experiment ranges from around 1027 nm to 1059 nm in wavelength, with special care to ensure a peak in the power near $\lambda = 1030$ nm. The increased power in this range appears directly correlated with the generation of 515 nm light through second-harmonic generation. The physics and applications of second-harmonic generation will be discussed further in a later section of this chapter. The spectrum for the laser that is used for alignment and some measurements can be seen in figure 3.1.

The laser in use has a quoted less than 10 μrad pointing error after the initial heating which is quoted as being 30 minutes [63]. In practice the real heating typically takes over an hour before the temperature of the electronics settle to a stable temperature $\pm 0.3°C$. As a result of the pointing error, the laser must be allowed to reach the operating temperature before the alignment of sensitive optics may be done.

The spectrum generated by the laser seen in figure 3.1 is controlled by four liquid crystal polarizers. The liquid crystal polarizers are non-linearly dependent on one another. By altering the voltage applied to each liquid crystal polarizer the laser user is able to tune the spectrum to the desired output for a given experiment with a number of limitations.

While the liquid crystal polarizers are controlled primarily by the voltage applied to them they are also strongly impacted by ambient conditions. As the lab fluctuates in temperature and humidity throughout the day there are notable changes in the spectrum. This means that the requirements for a spectrum are not only defined by the experiment it is intended for in terms of output intensity with respect to wavelength, but also the regions of stability.

Stability is defined here as the phase space region where the laser beam can maintain

its pulse characteristics. There are many combinations of voltage values that can be applied to the polarizers that will result in a continuous wave (CW) beam or some superposition of a continuous and pulsed beam. Under these conditions the lasers amplifier and pulse compressor cannot operate and shut down as they are only able to operate with a pulsed beam. If the laser is operating with a combination of voltage values which results in low stability and the surrounding temperature or humidity changes slightly, the laser will turn off automatically. Should this occur during a measurement, the measurement must then be discarded. For this reason, one of the requirements of stability is that there be a variation of at least 0.03 V on each liquid crystal polarizer, preferably closer to 0.05 V where the pulse is considered to have adequate stability or in other words, where no continuous wave is generated. For good practice, the stability of a spectrum is ensured daily before operating the laser.

3.2 Second Harmonic Generation

For this apparatus, we have chosen to operate with an IR pump beam and an optical probe. This choice is made as the optical probe will result in the ability to generate a smaller beam spot size. In the future development of this apparatus, there will eventually be an added functionality to adopt a scanning Kerr effect measurement in order to image the magnetic state of a sample. For imaging purposes, the smaller spot size will allow for higher image quality.

To complete the pump-probe experiment for the time-resolved magneto-optical Kerr effect experiment, the IR beam is split to follow two paths. One of the beams is then directed towards a β-barium borate crystal (BBO). The BBOs nonlinear susceptibility leads to a process known as second harmonic generation (SHG) where a portion of the IR beam is frequency doubled and thus 1030 nm light is converted to 515 nm light, which is in the green region of the visible spectrum.

In most linear optical media, the polarization could be described by the strength of the electric field of the incident light as:

$$P(t) = \epsilon_0 \chi^{(1)} E(t) \tag{3.1}$$

where $\chi^{(1)}$ is the first order susceptibility and ϵ_0 is the permittivity of free space [64]. The polarization can, however, be expanded into a power series in E(t) to obtain higher order terms [65]

$$P(t) = \epsilon_0 \left(\chi^{(1)} E(t) + \chi^{(2)} E(t)^2 + \chi^{(3)} E(t)^3 + ... \right), \tag{3.2}$$

where $\chi^{(2)}$ and $\chi^{(3)}$ represent the second and third order susceptibility terms respectively.

Equation 3.2 is a good first introduction but makes some assumptions that do not hold for all cases. For one, equation 3.2 treats the polarization and incident electric field as scalar quantities, whereas these are actually vector quantities. Equation 3.2 also assumes the polarization at a given time is only dependent on the instantaneous strength of the applied electric field, thus assuming the system to be lossless and dispersionless.

The wave equation in a nonlinear medium typically takes the form

$$\nabla^2 \vec{E} - \frac{n^2}{c^2}\frac{\partial^2 \vec{E}}{\partial t^2} = \frac{1}{\epsilon_0 c^2}\frac{\partial^2 \vec{P^{NL}}}{\partial t^2}. \tag{3.3}$$

We may take the incident electric field to generally be described as:

$$E(t) = Ee^{-i\omega t} + c.c. \tag{3.4}$$

where c.c. is in place of the complex conjugate of the adjacent term. From equation 3.2 we find the second order polarization term takes the form

$$P^{(2)}(t) = 2\epsilon_0 \chi^{(2)} EE^* + \left(\epsilon_0 \chi^{(2)} E^2 e^{-i2\omega t} + c.c.\right). \tag{3.5}$$

If we substitute equation 3.5 into equation 3.3, assuming no spatial dependence of the electric field such that the first term in the wave equation is zero, we find

$$n^2 \sin(\omega t) = 4\chi^{(2)} E \sin(2\omega t) \tag{3.6}$$

if we take the real part of the electric field. We find, from a given initial frequency, a crystal with a non-zero second order susceptibility generates light with twice the frequency of the initial incident beam [64].

The second-harmonic generation resulting from the BBO crystal is not only beneficial in reducing the probe spot size, but may also be exploited for a number of other purposes. In chapter 4.2 we will discuss how BBOs nonlinear susceptibility may be used to generate an autocorrelation peak to determine when the pump and probe have traveled the same distance. This autocorrelation peak additionally may be used to determine the step size of the long delay line alongside the repeatability of its motion. For now, we may investigate the quality of the two meter rail before we determine its step properties.

3.3 Long Scale Time Delay

A critical element of this apparatus is the two meter delay line that optimally could allow for a time delay of up to 13.3 ns. The laser in use is primarily operated in 10 MHz mode, leading to one pulse every 100 ns, so even with the long delay line, we only expect to see the results of a single pulse interacting with the sample. The maximum frequency mode of the laser is 60 MHz, so even with the maximum number of pulses per second generated, a delay of over 16 ns would be required to observe more than one pulse. The long delay line allows for the observation of slow spin waves with GHz range frequencies.

For the purpose of improving the alignment of the long delay line, a large area retroreflector from Edmunds Optics is used on a cart which may travel along the delay line operated by a stepper motor with an Arduino and an Adafruit motor shield controller. A retroreflector is used as it reflects light back accurately in the direction of origin with an offset in position. As a result of the use of a retroreflector, so long as the rail is straight such that the retro itself is not moving in the plane perpendicular to the plane of incidence of the light, the steering mirrors just before the delay line may be adjusted so that the beam at some location on the table following the retroreflector will not move no matter the path length of the beam. The rail unfortunately was not perfectly linear when the early work on this project began. In the beginning, no matter the angle of incidence, the beam returned by the retroreflector demonstrated a notable change in position.

The rail itself has metric holes for mounting to an optical table, but the table in use is imperial. To accommodate the incompatible mounting holes, the rail was attached to the optical table using slotted bases from ThorLabs. It was with these slotted bases that minor adjustments were able to be made to increase the linearity of the rail. A measurement was made by moving the retroreflector along the rail and detecting the resulting intensity with a Newport power meter in order to observe the response of the rail. The power meter has a filter to reduce the intensity of light below the detectors saturation point. This filter has a relatively small area of constant refractive index, with a rapid increase in detected signal as the beam deviates from the center position. This may be exploited as it will amplify the effects of beam wander in these measurements. A clamp at a given position along the rail as pictured in figure 3.2, could then be tightened or loosened to apply more or less force in a given direction on the slotted base mount.

The specific position along the delay line which required adjustment was determined by manually moving the retroreflector along the rail. The Zurich Instruments MFLI lock-in amplifier applied to this experiment has a web interface which may present a real time display of the detected signal. Once the retroreflector had been moved to

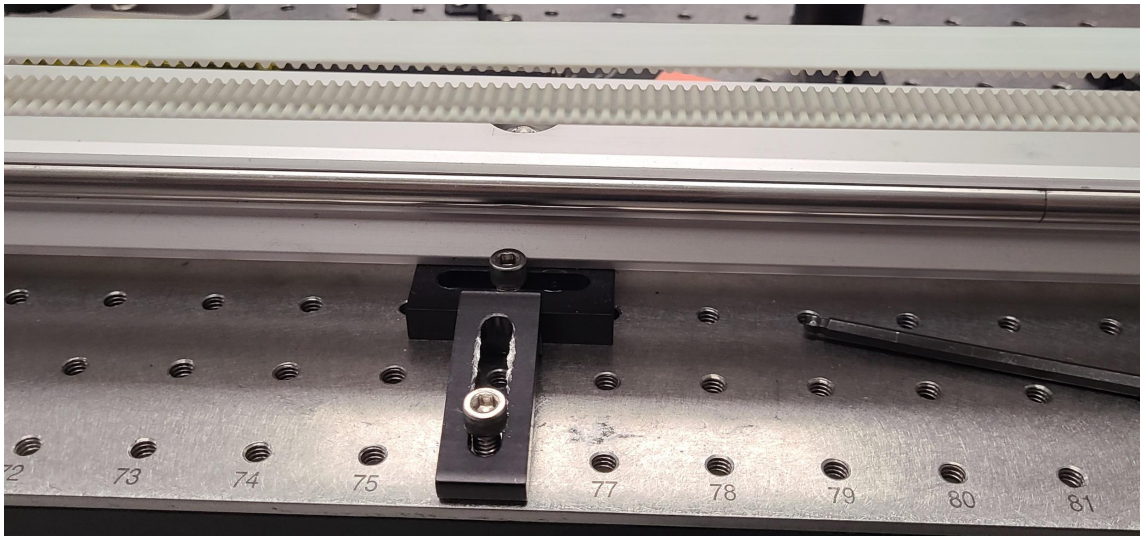

Figure 3.2: A clamp tightened to push on a slotted base clamp holding the linear rail.

an appropriate position demonstrating an alteration in signal, the corresponding plate would be adjusted while watching the effect on the displayed intensity. Another measurement is then run to check the adjustment, and this process is iteratively repeated. An example of two of these measurements is presented in figure 3.3.

Once the best linearity was achieved, all of the slotted base clamps were secured in place. Through this process it was determined that approximately the last 30 cm of the rail could not be held in a position that was sufficiently consistent with the rest of the stage and so that portion of the rail is not used for additional measurements. Additionally, due to space constraints on the table, a small amount of the rail on the other end is inaccessible. The resulting maximum possible delay for this experiment is

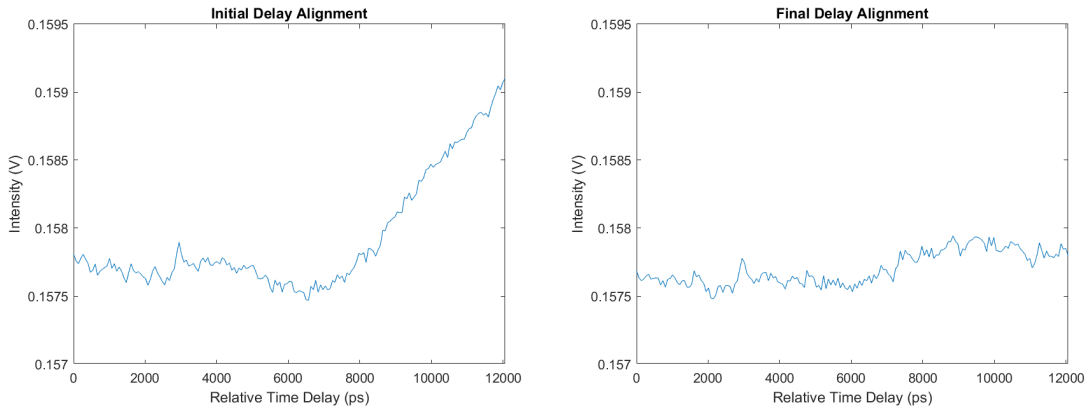

(a) **(b)**

Figure 3.3: Intensity measurements as the rail is taken from initial alignment (a) on table to being pushed to a more linear position (b). Note that the power meter in use requires a neutral density filter which has edge effects that lead to an increase in intensity when the beam has just moved to an edge of the filter.

10.7 ns.

At this stage in the development of the apparatus, the linear stage has been adjusted to provide satisfactory linearity and the beam wander resulting from the stage has been minimized. We now turn our attention to the retroreflector which played a notable part in simplifying the use of this long delay line.

3.3.1 Retro Reflectors

Alignment of a beam along a 2 meter distance is not the most complicated thing to do. Aligning the beam such that the returning beam remains in the same alignment as the path length shortens however, is highly non-trivial. Should this method be attempted, the researcher would be left with four points which alter the beams directional vector (two steering mirrors sending the beam down the line, then two additional mirrors to return the beam in the direction from which it came). This process is not terribly difficult over short distances, but tedious and highly challenging as the distance increases. The corner-cube retroreflector is truly the solution to this issue.

Corner-cube retroreflectors are, in fact, quite fantastic for aligning light traveling far distances, as they return the light in the direction from which it came with a high degree of accuracy. For example, perhaps the most famous usage of corner-cube retroreflectors are the arrays of retroreflectors on the moon. These arrays have been used for decades now in the pursuit to understand the moon's internal structure as well as the dynamics describing how the Moon and Earth influence one another [66, 67]. Surely if an array of small corner-cube retroreflectors on the Moon are able to return light to Earth for many years as they shift on the Moon's surface, a large area corner-cube retroreflector is more than a fair solution for a difficult alignment problem over a distance of two meters.

The light generated by the laser for this experiment is linearly polarized, so to ensure the optics on table are not altering the polarization of the light in any way, we may calculate the effect of a retroreflector on the electric field of an incident beam. Liu and Azzam describe the use of ray-tracing in order to obtain the Jones matrices describing the polarization of light once it has traveled through a retroreflector [68]. In their analysis, Liu and Azzam choose to numerically solve for each value of the Jones matrix and it's eigenvalues for each individual path a ray could follow within a corner-cube retroreflector assuming it travels in a counter-clockwise direction. We will instead follow closely the convention taken on by Scholl, where a general solution is obtained [69].

First, we must define some language for this discussion. A corner-cube retroreflector is made up of three plane mirrors, each at a right angle to the others, thus in the orientation of the corner of a cube. When looked at head on, the corner-cube retroreflector appears to have six total sections resulting from reflections of the seams between the

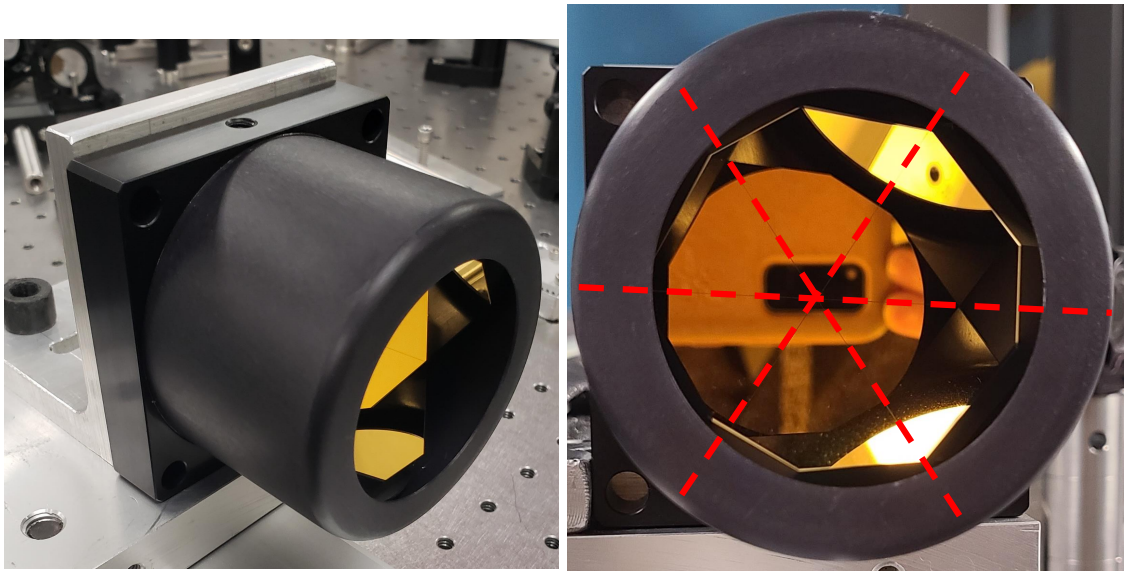

Figure 3.4: The hollow corner cube retroreflector from Edmunds Optics on the cart on the long delay line. The lines between sections are highlighted with red dashed lines.

mirrors. The retroreflector used for this research is pictured in figure 3.4.

We will consider an arbitrary ray of light incident on an ideal corner-cube retroreflector

$$\vec{K}_i = (l, m, n) = (K_{i,x}\hat{i}, K_{i,y}\hat{j}, K_{i,z}\hat{k}), \tag{3.7}$$

where $\hat{i}$, $\hat{j}$, and$\hat{k}$ are the unit vectors for x, y, and z respectively. In this case an ideal retroreflector is defined as one which does not alter the direction, phase, or amplitude of light, independent of the segment. Starting with a coordinate system as defined in figure 3.5.

The ray incident on the retroreflector undergoes three reflections before being sent back in the same direction from which it came. Thus, the normalized exiting wave vector may be written as

$$\vec{K}_f = R_{yx}R_{xz}R_{zy}\vec{K}_i, \tag{3.8}$$

where R_{yx} is the reflection matrix off of the y-x mirror. As we are assuming a perfect retroreflector with no differences in surface quality, reflectivity, or angle between the three mirrors, the order of the reflections in equation 3.8 will yield the same result [70]. As the light reflected from a corner-cube retroreflector returns in the direction of incidence, we can write the exiting wave vector as

$$\vec{K}_f = (-l, -m, -n). \tag{3.9}$$

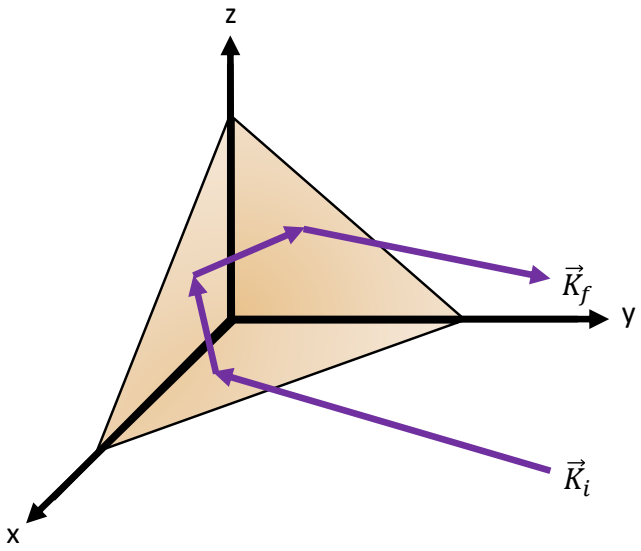

Figure 3.5: Coordinate definition for an arbitrary ray of light incident on a corner-cube retroreflector where $\vec{K}_i$ and $\vec{K}_f$ are the incident and reflected rays respectively.

The complex reflectivity for each polarization state is represented by:

$$R_{\parallel}(\theta_i) = r_{\parallel}(\theta_i) exp[i\phi_{\parallel}(\theta_i)] \quad \text{and} \tag{3.10}$$

$$R_{\perp}(\theta_i) = r_{\perp}(\theta_i) exp[i\phi_{\perp}(\theta_i)] \tag{3.11}$$

where r is the amplitude reflectivity and ϕ is the phase.

We will use figure 3.6 to define $\hat{N}$ as the unit vector normal to the plane of incidence which can be expressed as

$$\hat{N} = \frac{\vec{K}_i \times \hat{S}}{\left|\vec{K}_i \times \hat{S}\right|}. \tag{3.12}$$

We may additionally define a unit vector perpendicular to both $\vec{K}_i$ and $\hat{N}$,

$$\hat{M} = \vec{K}_i \times \hat{N}. \tag{3.13}$$

Following from the convention set forth by Scholl [69], the electric field of the incoming beam in terms of these new unit vectors after one reflection is altered as

$$\vec{E_{R\parallel}} = R_{\parallel}(\theta_i)(\vec{E}_i \cdot \hat{M})\hat{M} \quad \text{and} \tag{3.14}$$

$$\vec{E_{R\perp}} = R_{\perp}(\theta_i)(\vec{E}_i \cdot \hat{N})\hat{N}, \tag{3.15}$$

where each term in equations 3.14 and 3.15 is dependent on the angle of incidence of an arbitrary ray of light.

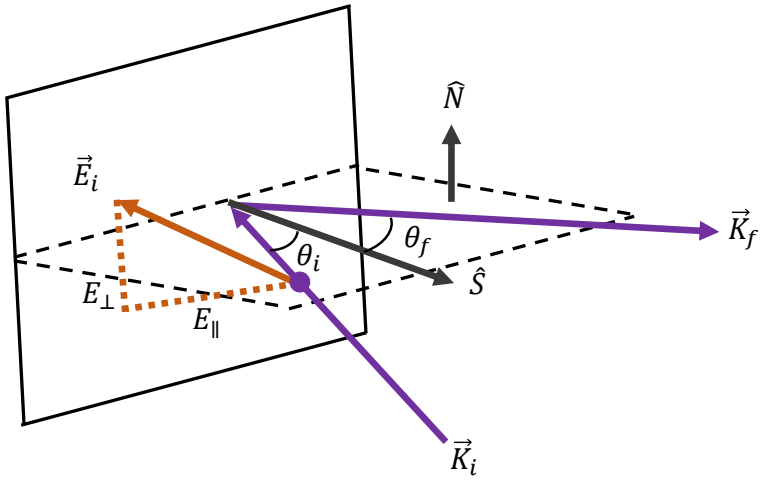

Figure 3.6: The geometry of the reflection of an incident beam $\vec{K}_i$ where E_i is the electric field of the incident beam. The surface normal is defined as $\hat{S}$ and the normal to the plane of incidence is defined as $\hat{N}$. This sketch is recreated from [69].

Thus far, we have been treating the corner-cube retroreflector in an ideal case where the three mirrors are identical and perfectly orthogonal to one another. While the retroreflector applied to the experiment of this work is not far from the ideal case, a phase shift must still be introduced to the electric field to account for minor irregularities. The electric field after the first reflection will undergo a phase shift described by

$$E_{i,1} = E_i \exp(i\phi_1). \tag{3.16}$$

After three reflections the beam exits the retroreflector. Expanding the electric field into its parallel and perpendicular components, the electric field of an arbitrary incident beam, taking into account variations in the optical component is:

$$\begin{aligned}
&\vec{E_{R3}} \\
&= [R_{1\parallel}(\theta_i) R_{2\parallel} R_{3\parallel} (\vec{E}_i \cdot \hat{M}_1)(\hat{M}_1 \cdot \hat{M}_2)(\hat{M}_2 \cdot \hat{M}_3) \\
&\quad + R_{1\perp}(\theta_i) R_{2\parallel} R_{3\parallel} (\vec{E}_i \cdot \hat{N}_1)(\hat{N}_1 \cdot \hat{M}_2)(\hat{M}_2 \cdot \hat{M}_3) \\
&\quad + R_{1\parallel}(\theta_i) R_{2\perp} R_{3\parallel} (\vec{E}_i \cdot \hat{M}_1)(\hat{M}_1 \cdot \hat{N}_2)(\hat{N}_2 \cdot \hat{M}_3) \\
&\quad + R_{1\perp}(\theta_i) R_{2\perp} R_{3\parallel} (\vec{E}_i \cdot \hat{N}_1)(\hat{N}_1 \cdot \hat{N}_2)(\hat{N}_2 \cdot \hat{M}_3)] \hat{M}_3 \\
&\quad + [R_{1\parallel}(\theta_i) R_{2\parallel} R_{3\perp} (\vec{E}_i \cdot \hat{M}_1)(\hat{M}_1 \cdot \hat{M}_2)(\hat{M}_2 \cdot \hat{N}_3) \\
&\quad + R_{1\perp}(\theta_i) R_{2\parallel} R_{3\perp} (\vec{E}_i \cdot \hat{N}_1)(\hat{N}_1 \cdot \hat{M}_2)(\hat{M}_2 \cdot \hat{N}_3) \\
&\quad + R_{1\parallel}(\theta_i) R_{2\perp} R_{3\perp} (\vec{E}_i \cdot \hat{M}_1)(\hat{M}_1 \cdot \hat{N}_2)(\hat{N}_2 \cdot \hat{N}_3) \\
&\quad + R_{1\perp}(\theta_i) R_{2\perp} R_{3\perp} (\vec{E}_i \cdot \hat{N}_1)(\hat{N}_1 \cdot \hat{N}_2)(\hat{N}_2 \cdot \hat{N}_3)] \hat{N}_3.
\end{aligned} \tag{3.17}$$

In equation 3.17, the subscripts correspond to the order of the reflection and the phase change associated with the angle between mirrors is built into $\hat{M}_{1,2,3}$ and $\hat{N}_{1,2,3}$ for each reflection. The result that equation 3.17 provides is that the final electric field is a function of the incident angle and is also dependent on the the true angle between the mirrors, the reflectivity of the mirrors, and any non-uniformity in the mirror surfaces. Alternative methods of calculating the effects of a corner-cube retroreflecter have been used, all of the methods suggesting that barring a perfect retroreflector, there will be an effect on the electric field of the final beam; see references [70–75].

The corner-cube retroreflector is an important optic in solving the alignment problem of the two meter delay line. The main elements affecting the electric field are the angles of the mirrors and the surface quality. The calculation presented here makes no assumptions where the retrorflector is treated any differently than a series of three mirrors. It makes sense then, to compare the result of the retroreflector with the option of two mirrors to return the beam down to long delay line. The transformation to the electric field after only two reflections by this same analysis is

$$\begin{aligned} E_{R2} =& R_{1\parallel}(\theta_i)R_{2,\parallel}(E_i\cdot\hat{M}_1)(\hat{M}_1\cdot\hat{M}_2)\hat{M}_2 \\ &+ R_{1\perp}(\theta_i)R_{2\parallel}(\vec{E}_i\cdot\hat{N}_1)(\hat{N}_1\cdot\hat{M}_2)\hat{M}_2 \\ &+ R_{1\parallel}(\theta_i)R_{2\perp}(\vec{E}_i\cdot\hat{M}_1)(\hat{M}_1\cdot\hat{N}_2)\hat{N}_2 \\ &+ R_{1\perp}(\theta_i)R_{2\perp}(\vec{E}_i\cdot\hat{N}_1)(\hat{N}_1\cdot\hat{N}_2)\hat{N}_2. \end{aligned} \tag{3.18}$$

Two mirrors placed and adjusted by hand will lead to a larger difference from orthogonal alignment of the mirrors when compared to the retroreflector which is quoted to have a parallelism (the potential variation in the return beam) of only two arcseconds [76].

The end result of the calculations in this section is that there is an effect on the electric field of the incident beam. Experimentally this has been found to be indistinguishable when checked using a Wollaston prism, however this does lend insight to the placement of optics for some of the various effects we wish to observe. For instance, with the inverse Faraday effect measurements, the polarization of the pump is altered using a quarter waveplate. With the effects described in this section, it is only logical to convert the pump from linear polarization to circular polarization immediately before the pump is directed towards the sample.

Traveling further down the beam path of this experiment, the next optics to consider alter the polarization of the beam in order to begin to detect a Kerr rotation.

3.4 Detection Scheme

The detection scheme for the measurement of the Kerr effect needs close consideration due to the low signal to noise associated with the Kerr rotation.

Overall, the detection scheme consists of some carefully chosen polarizers both to ensure linear polarization before the light interacts with the sample, as well as to improve our ability to detect the rotation afterwards. The detection scheme is then followed by two large-area photodiodes from ThorLabs which were used in conjunction with a Zurich Instruments MFLI lock-in amplifier. In this section, we will discuss the details of the polarization optics as well as the signal processing and demodulation of the laser beam using the lock-in amplifier.

3.4.1 Polarization Optics

The polarization of light describes how the electric field of a beam propagates through time and space. The light generated by the laser passes through a number of polarizers to ensure a clean, linearly polarized beam before the polarization may be altered by the magnetic state of the sample. There are, however, a number of optics which alter the polarization of the light along the probe beam line and so we will start at the first polarization optic and work along the path the probe takes.

As we've discussed in previous sections, the second order susceptibility of the BBO crystal means the polarization of the beam may be altered depending on the crystal's orientation. While there is some control over the polarization, optimizing for maximum generation and then adding in a linear polarizer (colloquially dubbed a scrubber) to clean up the polarization of the beam leads to the largest remaining intensity.

Through experimental observation, it was noted that the primary polarization component flipped following the green generation. This was noted by intercepting the IR beam before the BBO with a Wollaston polarizer. The axis of the Wollaston was then rotated such that one of the components exiting was minimized. Once this was done the angle was locked in using a set-screw and the Wollaston was moved to intercept the green generated beam. The beam that was minimized in IR was now maximized in green. The polarization also appeared to no longer be linear following the green generation, so it was necessary to add a linear polarizer. This test additionally determined that a 90° rotation should be made to the IR beam on the pump or probe such that both beams are linearly polarized in the same axis by the time they interact with the sample.

The tool for the 90° rotation in polarization is a half-waveplate. The way a waveplate (also known as a wave retarder) alters the polarization of the light can be best understood by looking at the matrix which describes the system:

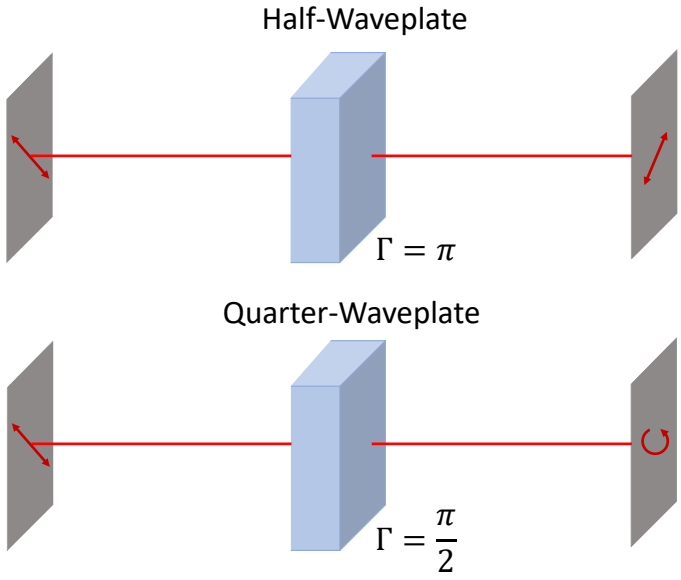

Figure 3.7: A sketch of the effects of a half- and quarter-waveplate on linearly polarized light. Sketch inspired by reference [77].

$$\begin{bmatrix} 1 & 0 \\ 0 & e^{-i\Gamma} \end{bmatrix}. \tag{3.19}$$

Equation 3.19 can be understood as the x-axis of the beam is left unaltered, while the y-axis is retarded by a phase Γ. This then defines the x-axis as the "fast axis" and the y-axis as the "slow axis" [77].

Linearly polarized light represented by the vector $\begin{bmatrix} 1 \\ 1 \end{bmatrix}$, incident on a quarter wave-plate with phase $\Gamma = \frac{\pi}{2}$ represented by the Jones matrix $\begin{bmatrix} 1 & 0 \\ 0 & -i \end{bmatrix}$ will be converted into left circularly polarized light. Alternatively, if the same light is incident on a half-waveplate with a phase $\Gamma = \frac{\pi}{2}$ represented by the Jones matrix $\begin{bmatrix} 1 & 0 \\ 0 & -1 \end{bmatrix}$, instead the light will exit the waveplate with vector $\begin{bmatrix} 1 \\ -1 \end{bmatrix}$. This is represented visually in figure 3.7.

As a result of the manner in which the BBO alters the polarization of incident light, it was decided to add a half-wave plate to the probe beam. The linear polarizer immediately before the sample will ensure a high purity polarization, so alterations early along the probe beam line will still leave the extinction ratio high near the sample.

The next polarization optic to discuss along the probe beam line is the linear polarizer used to scrub the beam. The Jones matrix for a linear polarizer is

$$\begin{bmatrix} \cos^2\theta & \sin\theta\cos\theta \\ \sin\theta\cos\theta & \sin^2\theta \end{bmatrix}, \tag{3.20}$$

where θ is the angle with respect to one axis. For this application, it was chosen to use a nanoparticle linear polarizer from ThorLabs. This polarizer in particular has an extinction ratio of at least $1:10^7$ for light in the 515 nm range, meaning that the power of light that transmits through the polarizer and is not the intended polarization is less than a ratio of $\frac{1}{10^7}$ and the vast majority of light without the desired polarization is reflected away.

The final two polarization optics in this beam line include a quarter waveplate which is used in order to reduce phase noise in the detection of the signal [78], and the detection polarizer.

Two different detection polarizers are used throughout this works. The first of these, and the polarizer used for the majority of the time is a Wollaston prism. The Wollaston prism has an extinction ratio of $20\,000:1$. The incident beam is split into its polarization components, which exit the Wollaston with roughly a 45° angle to one another. A sketch of the beam path through the Wollaston may be seen in figure 3.8.

The odd exit angles of the two beams from the Wollaston prism make the optimization of it's polarization axis difficult. This optimization procedure will be outlined later on in this chapter. As the angle defined by the Wollaston to split the beam shifts with the rotation of the polarizer, both of the exit beams move, then requiring a realignment of the photodiodes detecting these beams with each shift of the angle of the Wollaston prism.

Attempts were made to reduce the workload associated with optimizing the Wollaston angle. A 3D printed mount was made in order to hold the two photodiodes in place

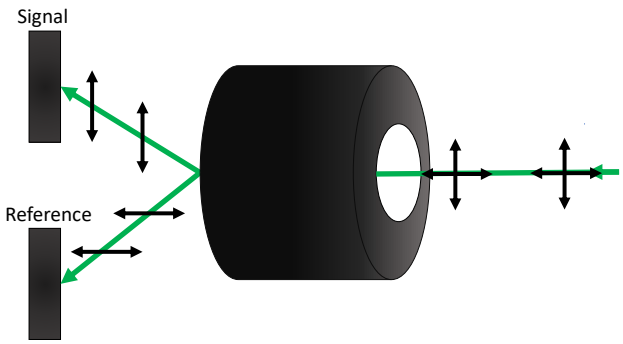

Figure 3.8: The geometry of the beams exiting a Wollaston polarizer.

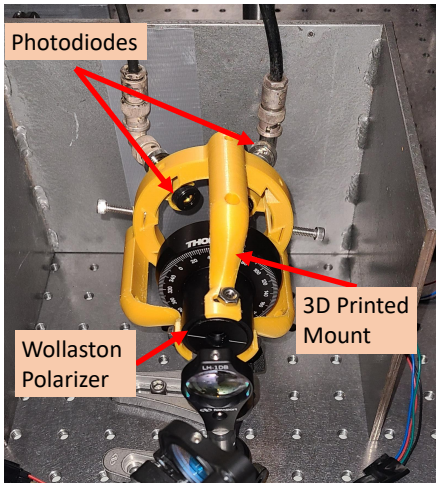

Figure 3.9: An image of the 3D printed mount used to simplify the optimization of the angle of the Wollaston prism. The black arrows indicate polarization to demonstrate how the polarizer splits light

as the Wollaston rotated. An image of this mount is seen in figure 3.9.

This mount was developed with the requirements that the angle indicator on the Wollaston must be visible, and there must be the ability to modify the position of the photo diodes for alignment purposes. This control over the position of the photo diodes was obtained by having a separate piece to hold each diode on an angled dove-tale insert such that the distance from the Wollaston prism may be adjusted. A set screw could then be tightened to lock in the position of the photodiode.

This design was a step forward but ultimately was unsuccessful. Further development could be done to make the design viable, however it was determined that the difficulty of alignment and relatively low extinction ratio of the prism warranted an upgrade. There are a number of upgrades to this mount which would be necessary for future use of the piece. The major downfall of the design is its rigidity. The weight from the photo diodes applied a strain on the three arms attached to the prism mount. This lead to unpredictable shifting of the photo diodes, then requiring frequent realignment, nullifying the purpose of the design. This could be solved by making a mount out of metal. The increased rigidity of, say, aluminium would be sufficient to reduce this problem significantly.

The other issue, which does not yet have a solution, is the visibility of the photo diodes themselves. As beams exiting the Wollaston prism are at an odd angle and the photo diodes are not necessarily being held at the exact angle, it is necessary to see the surface of the silicone active area to ensure no clipping of the beam is occurring. It can be seen in figure 3.9 that only one of the photo diodes is easily visible.

The upgraded polarizer is a 200 000 : 1 extinction ratio Glan-Laser Prism from LaserAnd optics. The design of most Glan-type polarizers is such that one beam passes

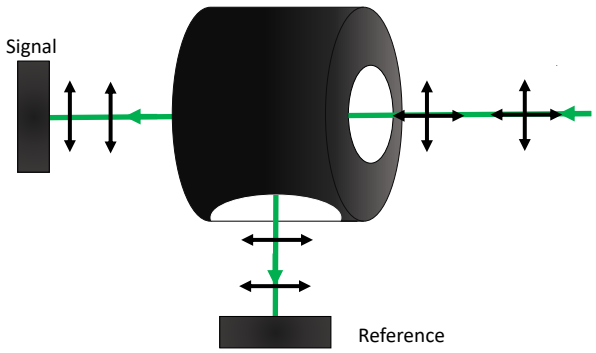

Figure 3.10: A Sketch of the splitting of polarization by an α-BBO Glan Laser prism and the detection by photodiodes labeled Signal and Reference. The black arrows indicate polarization to demonstrate how the polarizer splits light.

directly through the polarizer, while the other is reflected perpendicular to the incident angle. A sketch of the path through a Glan-Laser is presented in figure 3.10. Both the Wollaston and the Glan-Laser use birefringence to split the beam into the two polarization components.

The Glan-laser polarizer not only benefits from the higher extinction ratio, meaning a more pure polarization of the beam, but also the optimization of the angle for detecting the Kerr rotation becomes much easier with an improved precision mount. No matter the angle of rotation, one of the photodiodes will always remain aligned and only one must be moved. In addition, the new mount chosen for the Glan-Laser is a high-precision mount with angle measurements down to an arcminute ($1/60^{th}$ of a degree). The high precision mount is pictured in figure 3.11.

At this point, we have thoroughly discussed all of the optics required in order to alter the polarization of the beam. In the following section we will begin to turn our attention to the reduction of noise, starting with a technique known as demodulation.

3.4.2 Signal Demodulation

The collection and demodulation of signal for this experiment is done using a Zurich Instruments MFLI Lock-in Amplifier. This Lock-in amplifier is fed a reference frequency from a chopper placed in the beam line which periodically blocks and unblocks the laser beam. The frequency of the blocking and unblocking of the beam is then passed through a mixing algorithm in the lock-in amplifier and reduced from the input signal. The result is a visible signal which has had a large portion of noise automatically removed.

Demodulation is a common technique in optical measurements in the modern day.

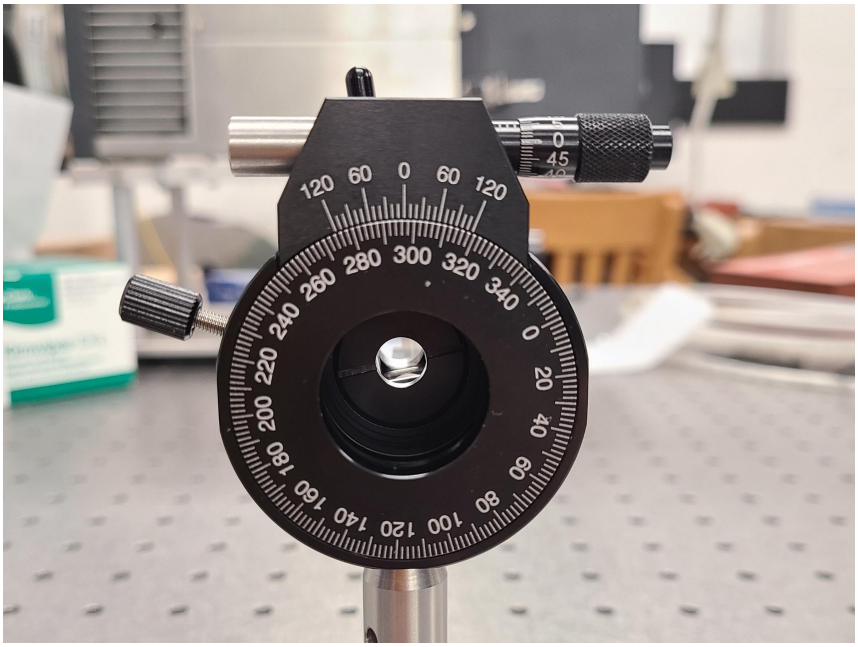

Figure 3.11: An image of the upgraded precision mount for the detection polarizer.

In most scenarios, the chopper would be placed along the pump beam line, The pump beam never goes to the detectors, however the probe reading the effects of the pump on the sample does, and this leads to the lock-in amplifier being highly sensitive to the types of magneto-optic effects this technique is employed to study.

Many measurements were made demodulating the pump beam, however the result, instead of a high sensitivity to alterations to the sample, was a high sensitivity to background scattering on the optical table. Blocking was put in place to reduce the background noise picked up but, likely due to the use of a retroreflector, it appears some of the noise travels along the same path taken by the probe beam near the photodiodes. This entirely eliminates the benefits to demodulating the pump, and thus for many measurements, we instead demodulate the probe.

The shortcomings of demodulating the probe are that we may be more sensitive to laser fluctuations, however, the benefit of no longer locking into an incessant background cannot be overlooked.

3.4.3 Signal-to-Noise Optimization

In 2003, Allwood et al. provided a detailed analysis of the factors that must be considered when optimizing the signal to noise of a MOKE apparatus as well as provided a procedure to do so [78]. Taking a look at figure 3.10, Allwood describes first placing the signal photodiode such that it detects the polarization passing straight through the detection polarizer. The polarizer is then rotated until the signal being detected reaches a minimum. This was done with a large area photodiode from ThorLabs connected to

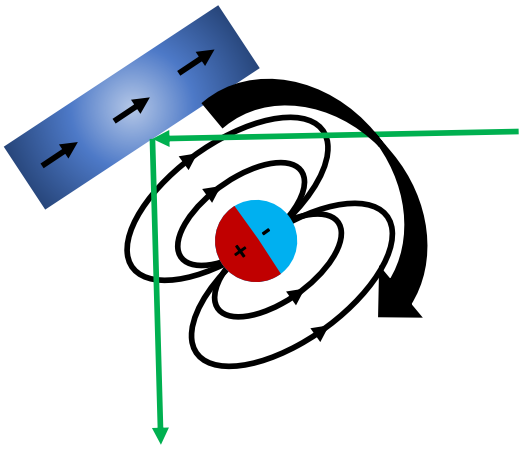

Figure 3.12: A cartoon depiction of the rotating magnet system for observing a DC MOKE response.

a Zurich Instruments MFLI lock-in amplifier. The Zurich lock-in amplifier has many functionalities accessible through it's use of a web-based interface such that a user can watch a real-time plotter of a voltage readout.

The plotter from the Zurich lock-in was used to minimize the signal beam, then a quarter waveplate was added in front of the Glan-Taylor, and again rotated to minimize the signal. Iterating back and forth between rotating the Glan-Taylor and the quarter-waveplate to minimize the signal until no further minimization could occur.

Allwood then describes rotating the detection polarizer (the Glan-Taylor in our case) by 1.7° for optimal signal to noise. This value is not consistent across all materials and thus does need to be optimized for the material as well as between different laser powers. In order to confirm the optimization, the reference photo diode is placed such that the reference beam is hitting the active area of its respective photo diode and a DC MOKE measurement is completed using the Zurich Instruments lock-in amplifier's built in DAQ.

3.5 DC MOKE

The magneto-optical Kerr effect describes how the polarization of light is altered when it is reflected off of a magnetic surface. In this section we will discuss the first observation of what is known as a DC MOKE response from the apparatus of this thesis. We will also expand on the ways in which DC MOKE can be useful in both the characterization of magnetic samples as well as the optimization of signal to noise for this project.

For the purpose of this experiment, the DC MOKE signal is treated as an optimization tool and a proof of functionality more than a method for characterizing the samples

themselves, although some information can be inferred through this process. In this section we will take a look at how a DC signal was obtained, we will go over the optimization routine followed for this apparatus, and discuss some of the results.

A cylindrical diametrically poled neodymium magnet was chosen for the DC MOKE experiment. The orientation of the poles (compared to an axially poled magnet) allows the magnet to be rotated without changing the distance to the sample and reducing the likelihood of blocking the beam, causing an artificial response. This magnet was connected to a small stepper motor so that for each step of the motor the magnet would rotate by some measurable amount. A cartoon depiction of the spinning magnet can be seen in figure 3.12.

An image of the setup can be seen in figure 3.13 where the magnet is placed at the closest position to the magnetic sample. The probe beam reflects off of a harmonic separator which ensures the remaining light is only 515 nm in wavelength, the probe then reflects off of a sample being influenced by the magnet on the motor and is sent to the polarizers for detection.

A schematic diagram of the setup for the spinning magnet measurements is presented in figure 3.14.

Upon first observation of a DC MOKE signal, the signal had to be checked against a reference to ensure that it was a real Kerr rotation and not the result a periodic non-magnetic alteration to the beam. The magnetic sample used for the first DC MOKE

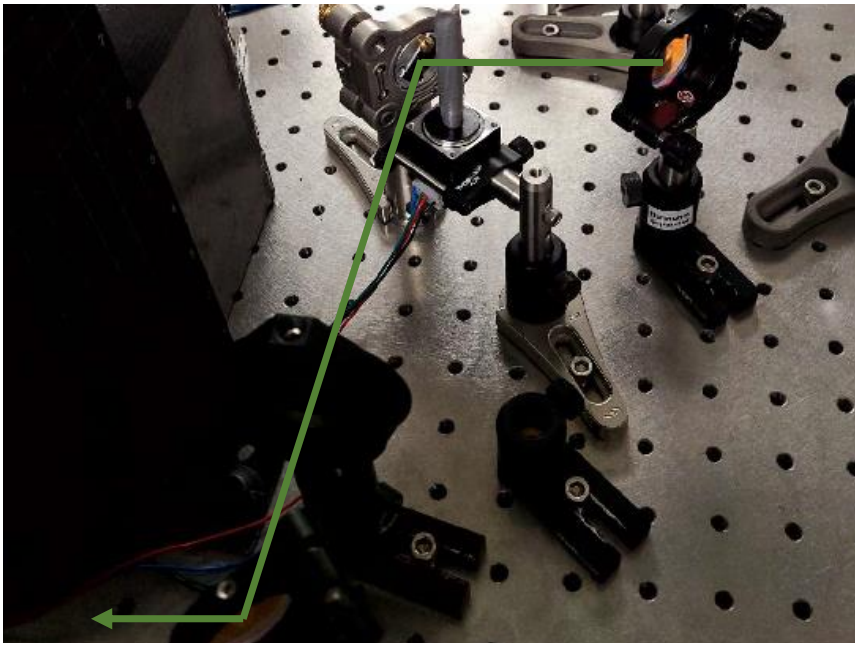

Figure 3.13: An image of the setup to detect a DC MOKE response. The magnet is magnetized along the long axis, such that when it spins it flips the magnetization of the nearby sample. This beam is then passed through a quarter-waveplate and sent to the detection polarizer, where the beam is split into its polarization components which are read by two photodiodes.

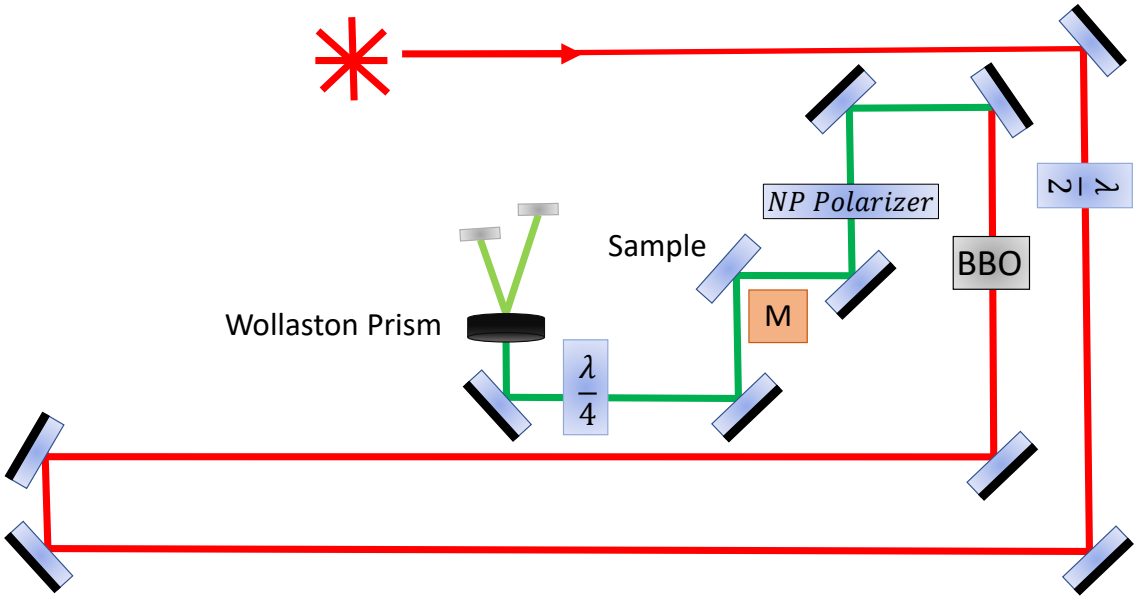

Figure 3.14: A schematic diagram of the beam line for the spinning magnet measurement. M is in the place of the spinning magnet.

measurements was a permalloy/cobalt oxide multilayer. To confirm the magnetic nature of the signal, the sample was substituted with a gold mirror. Gold in most applications can be treated as a non-magnetic metal. Certain cases taking advantage of heating [79] or gold nanoparticles will allow the study of gold's magnetic properties [80], however,

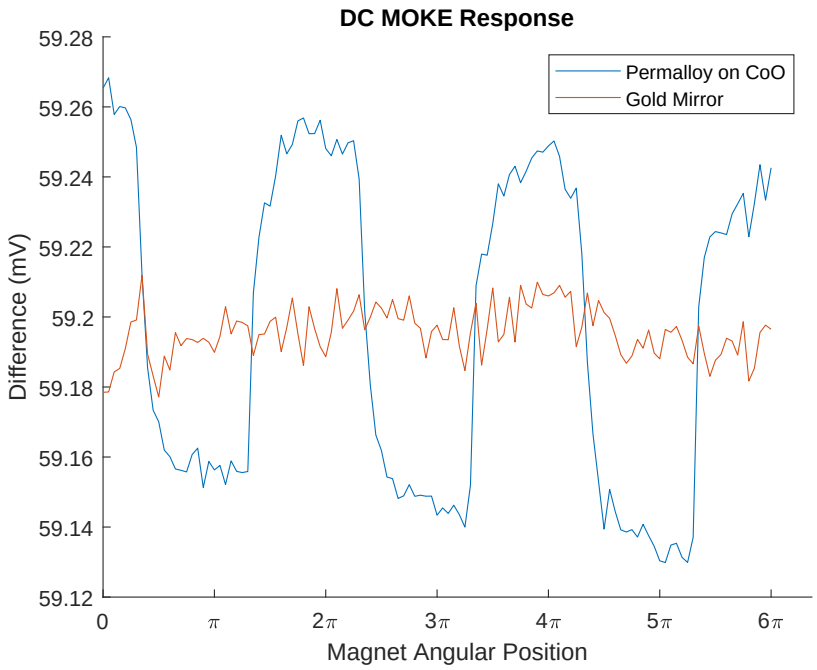

Figure 3.15: DC MOKE measurements where the magnet was rotated by about 1.5 turns total. Both the Permalloy on CoO and Gold mirror plots represents a single measurement without averaging.

with a room temperature gold mirror, little to no effect from the spinning magnet should be expected. These results are presented in figure 3.15 where there is a clear magnetic response from the Permalloy on CoO sample and no notable change in magnetization when the beam is reflected off the gold mirror.

First attempts at obtaining a DC MOKE measurement were completed with a Wollaston prism. The rotation mount on the Wollaston has angle indications every 2 degrees of rotation as seen in figure 3.16. To the best accuracy of this mount, the DC MOKE response was optimized using the methods previously outlined in this section. Once a DC MOKE signal was seen, the Wollaston would be rotated and a spinning magnet scan run, such that different angles of the Wollaston could be compared to determine the best signal to noise attainable. Figure 3.17 demonstrates a DC MOKE response from the Permalloy on CoO sample with the Wollaston first at the optimal angle in figure 3.17a, then rotated by just four degrees in figure 3.17b.

The large variability for minor changes in angle of the Wollaston demonstrates well the reason for upgrading to a higher quality polarizer in the form of the α-BBO Glan Laser (with an extinction ratio of 200 000:1) with a high precision mount with accuracy down to the arcminute as pictured in figure 3.11.

This brings us to the end of this chapter. The critical optics which are the pillars of this experiment have been noted and discussed in detail. We have explored much of

Figure 3.16: An image of the Wollaston prism used for the majority of this project

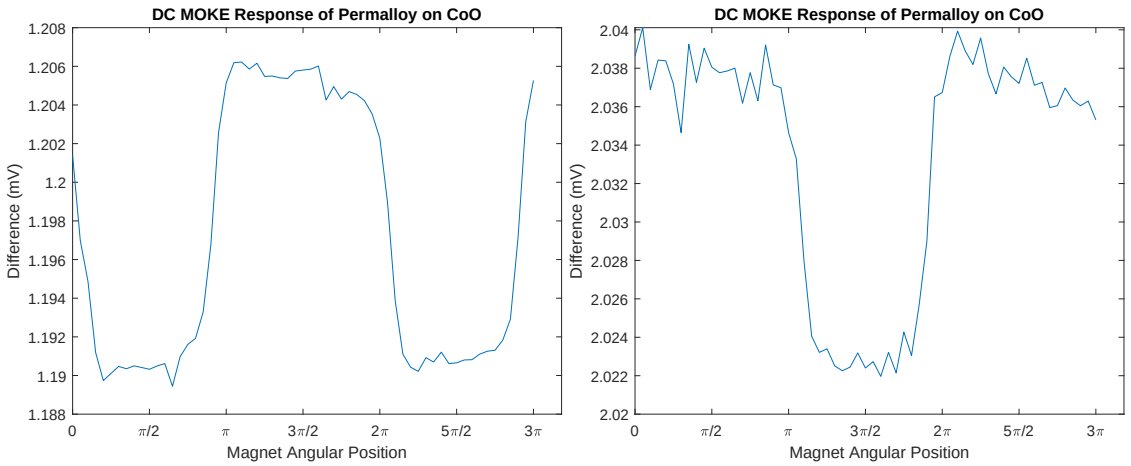

(a) **(b)**

Figure 3.17: MOKE response from Permalloy on CoO resulting from the rotation of a magnet near the sample as described in figure 3.12. Figure 3.17a has optimized signal-to-noise and figure 3.17b has the quarter waveplate before the detection polarizer off the optimized angle by a 3° rotation.

the initial work towards improving the quality of the long delay line and developed an understanding of the laser polarization along every stage of the beam path. The first observation of a Kerr rotation has been detected and thus, half of the goal of this project has been achieved. In the section to follow we will now build out the apparatus to make proper use of both delay lines towards the goal of observing a time-resolved signal.

Chapter 4

The Time-Resolved Magneto-Optical Kerr Effect

The invention of the laser in 1960 was followed by a huge leap in the development of many scientific techniques [81]. In 1964 Willis Lamb showed that a pulse limited by the bandwidth of a laser could be generated using mode locking. This lead to the development of a 1.5 ps pulsed laser beam. Since this discovery, the push to generate shorter laser pulses continued with Donna Strickland and Gerard Mourou developing techniques to generate pulses of only 30 fs, then a group lead by Richard Fork in 1987 pushed this limit down to a 6 fs pulse [82]. Techniques were eventually applied to develop time resolved studies of magnetic samples over ultrafast timescales in 1991 [8]. This chapter aims to describe the experimental techniques applied in order to develop the DC MOKE measurement into TR-MOKE in order to study a variety of magnetic phenomena.

In this chapter, we will discuss the application of pump-probe techniques towards the goal of obtaining a time-resolved signal. We will discuss some of the methods of determining the starting point of these measurements through autocorrelation before we expand on the different techniques for optically pumping a sample. We will cover the physical measurement methods that are prepared to allow for this apparatus to study many of the dynamic behaviors discussed previously in chapter 2.

To begin this chapter, we will discuss some of the aspects of the initial design of this apparatus which were altered considerably over time.

4.1 Alterations to Initial Design

In the development of this project, there were a number of optical components that were expected to be a part of the final version of this setup that were discarded for

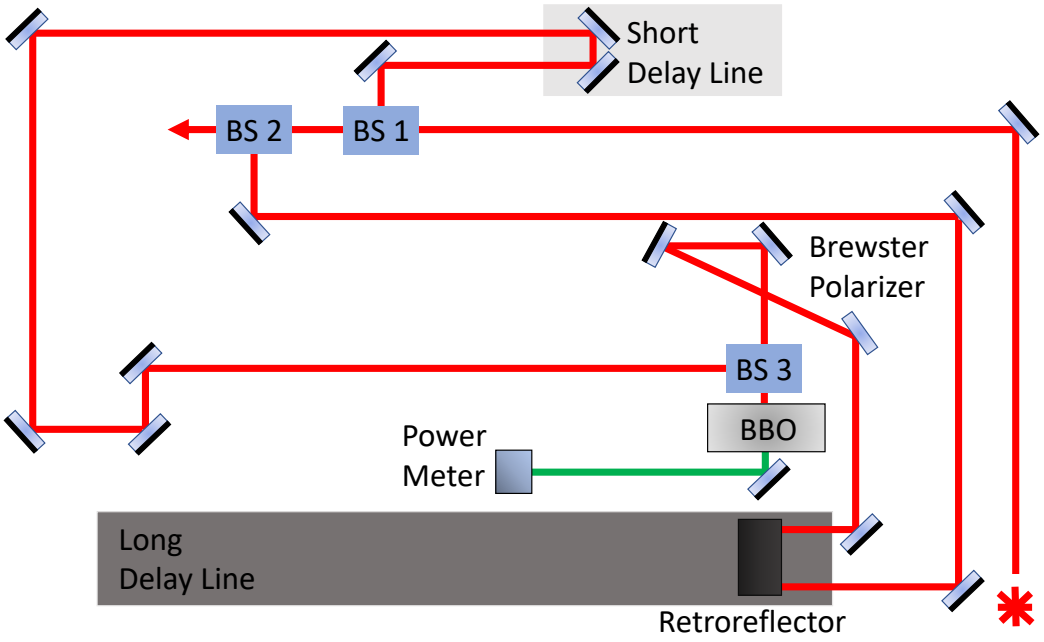

Figure 4.1: A schematic diagram of the original setup for the autocorrelation measurements where BS1 is a 90:10 beamsplitter, BS2 is an 80:20 beamsplitter, and BS3 is a 50:50 beamsplitter. For each beamsplitter, the larger percentage of the beam is reflected. The schematic is simplified to eliminate many of the optics that are not critical to the understanding of how it was set up.

various reasons. In order to keep reasonable continuity throughout this thesis, it is now important to make note of the optics that were discarded, those that were replaced, and those that will return in future work.

4.1.1 Long Delay Alignment

As discussed in chapter 3.3, the long time delay comes with a degree of beam wobble following the return beam. This was minimized in efforts described in chapter 3.3, however could not be entirely eliminated at that time. Figure 4.1 is a schematic diagram representing the early alignment for an intensity autocorrelation measurement which will be discussed later on in this chapter. As displayed in this diagram, the initial alignment had the probe traveling along the long delay line and the pump along the short delay line.

For some time in the development of this experiment, an issue was present where, at seemingly random times the detected signal would undergo a sudden increase or decrease in value. Due to the noted wobble resulting from the delay line, the first assumption was that the beam was occasionally clipping the edge of the detector leading to these odd observations. To solve this problem, the clear solution was to alter the alignment of the beams such that the pump travelled along both delay lines and the probe had a fixed path length. Unfortunately, this did not ultimately solve the

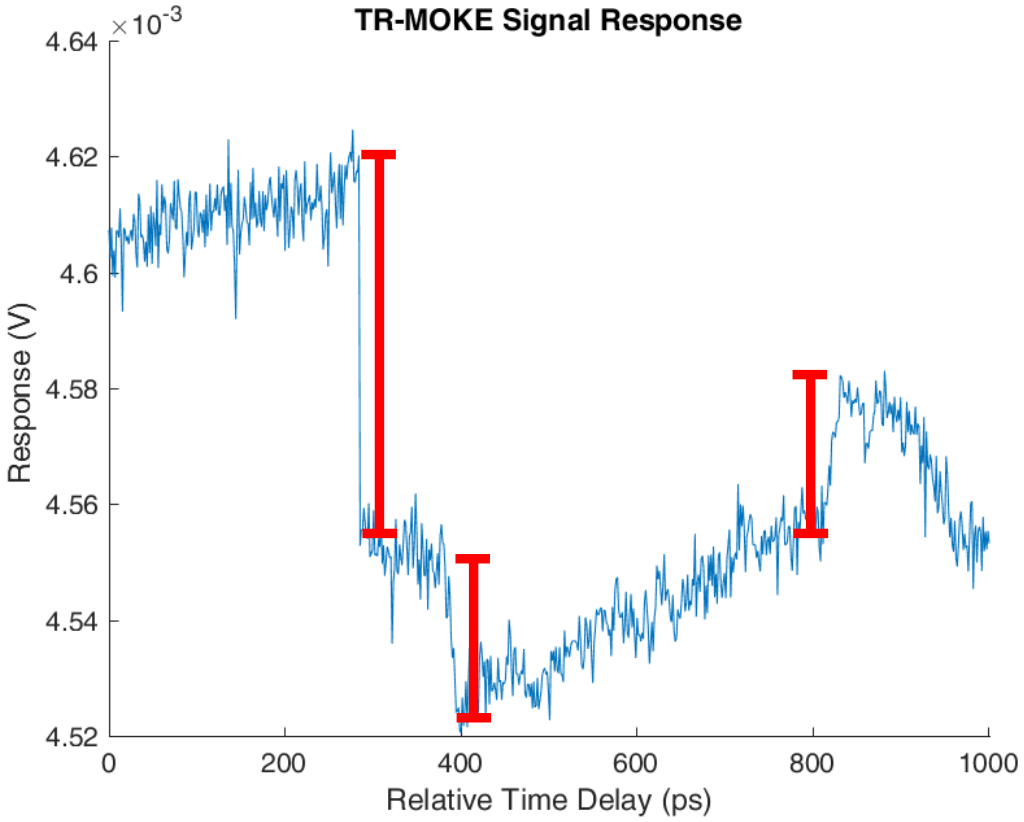

Figure 4.2: An example attempt at collecting a TRMOKE signal where the poynting vector of the laser shifted multiple times. The red bars mark the jumps resulting from the clipping of the Brewster polarizer.

problem of seemingly random alterations to the detected signal, but the alteration to the alignment remains.

4.1.2 Polarization Optics

The optic which turned out to be the culprit of the oddly altering signal is a small half-inch diameter Brewster polarizer. The Brewster polarizer is present in the schematic of figure 4.1 but is replaced with a nanoparticle polarizer in figure 3.14. The Brewster polarizer was originally intended to ensure linear polarization of the probe so that nearly perfectly linear light could be used to probe the sample to detect the Kerr rotation. This requirement of linear polarization still holds true. The Brewster polarizer was a small optic to begin with, but in addition had to be rotated to a steep angle to achieve Brewster's angle where the polarizer functions optimally. At Brewster's angle, the optic appeared to be just large enough for the beam to pass through without clipping the mount.

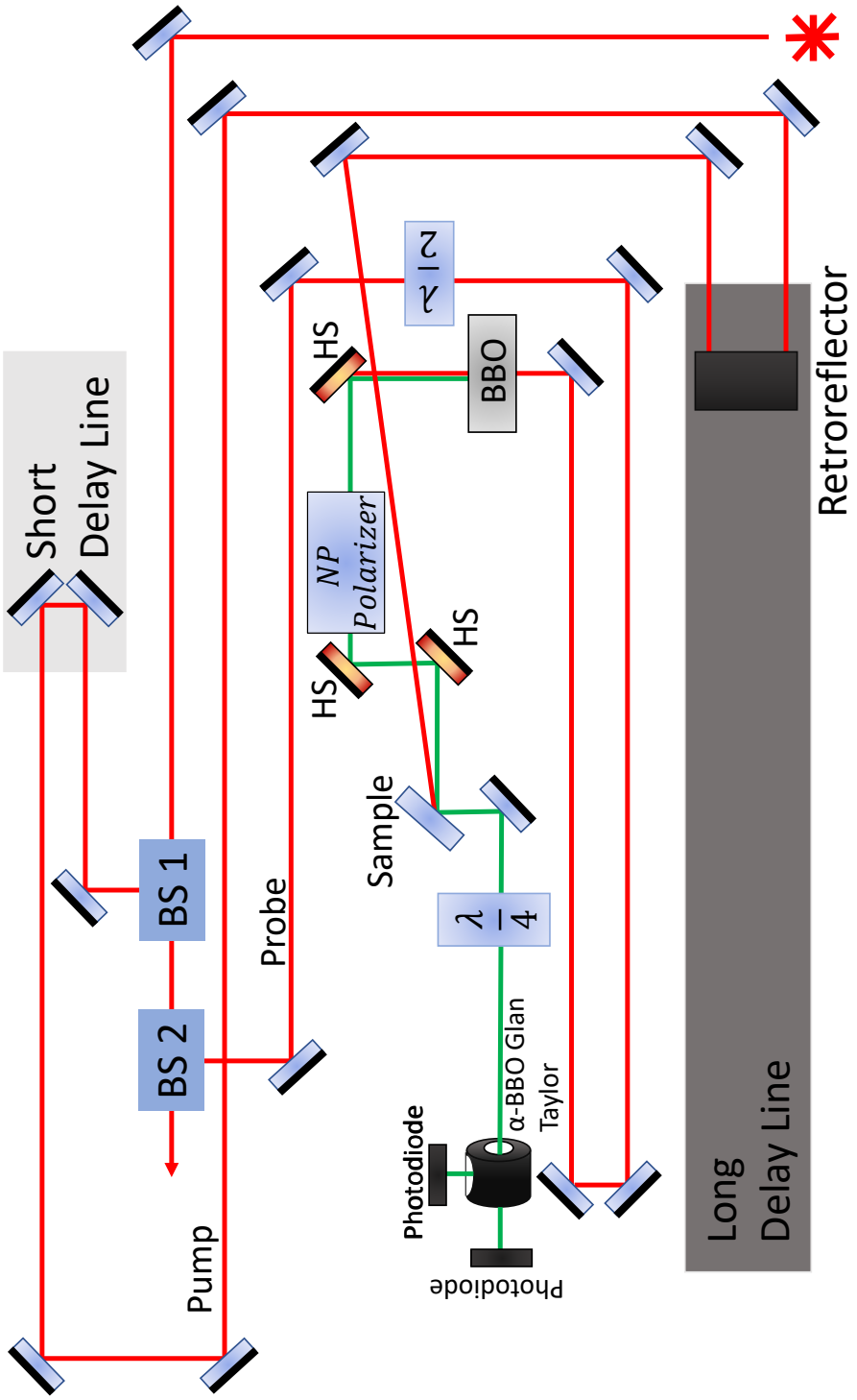

Figure 4.3: A schematic depiction of the full setup for TR-MOKE. For the autocorrelation measurements with a photoswitch, an IR mirror is placed immediately in front of the BBO. The harmonic separators are labeled HS and are designed to reflect 515 nm light while transmitting 1030 nm light. BS 1 and BS2 are the two beamsplitters on table with 90:10 and 80:20 reflection/-transmission respectively.

This may have been a sufficient requirement should the path length of the laser beam have been shorter. The laser applied for this experiment has a small pointing error as touched on in chapter 3. Over time, the angle of the light from the laser can vary slightly which may not be an issue for most applications. However, over a long beam line with small optics involved, this led to odd changes in the measured results when searching for a TR-MOKE signal. Due to the nature of the seemingly random small changes of the Pointing vector from the laser, it was not immediately obvious what it was causing this issue. An example of the effects of this error is presented in figure 4.2. This is a single data set where the retroreflector was moving in one direction along the long delay line. Scans were completed both increasing and decreasing the path length of the probe, however no consistent conclusions could be drawn from the results due to the nature of this signal.

Once the Brewster polarizer was removed from the beam line, the jumps in signal disappeared, indicating that the Brewster polarizer was definitively the cause. In place of the Brewster polarizer a nanoparticle linear polarizer was applied to the probe as seen in figure 3.14. A schematic diagram representing the final design of this TR-MOKE magnetometer is seen in figure 4.3.

Now that we have discussed some of the alterations from the initial design of this experiments which risked leading to confusion, we will turn our attention to the first time resolved measurement in the development of this experiment through an intensity autocorrelator.

4.2 Intensity Autocorrelation

By splitting the initial pulsed laser beam in two, the path length of the higher power beam (the pumping beam) and the lower power beam (the probing beam) may be manipulated to create a time delay as illustrated in figure 4.4.

As the speed of light is mostly constant in air, a measurement of the path lengths traveled by both beams gives an idea where along each delay line the optics must be to match the path length of the pump and probe. Through the development of the apparatus for this work, there have been a large number of changes to the initial design which will be discussed later in this chapter. The path of both beams at the time the autocorrelation measurements were taken is presented in a schematic diagram in figure 4.1.

When two pulsed laser beams pass collinearly through a crystal with nonlinear susceptibility, a nonlinear intensity response can be observed when the pulse from each beam interact with the crystal simultaneously as described by the proportionality

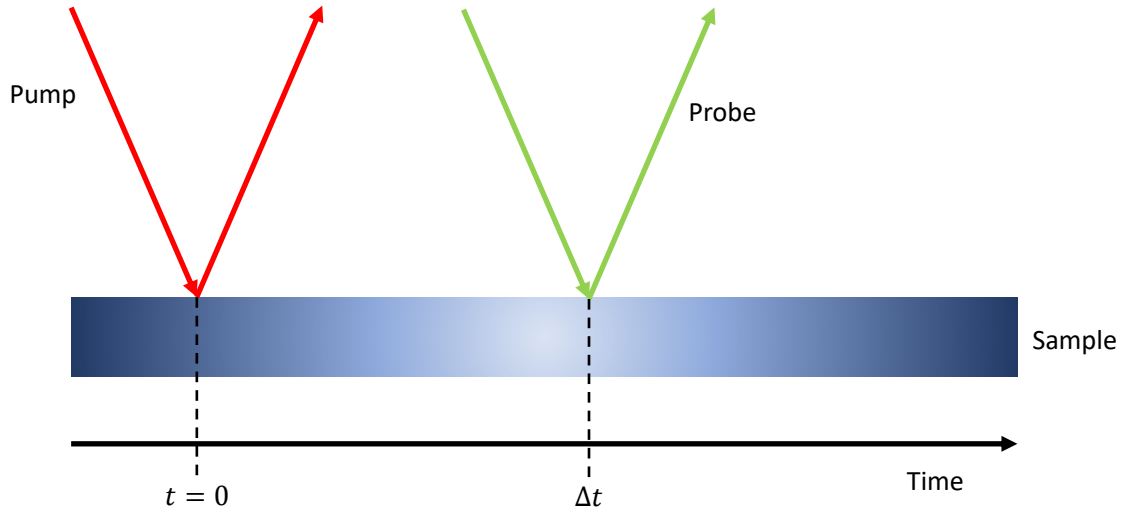

Figure 4.4: A cartoon depiction of a pump probe measurement. At $\delta t = 0$ the pump is first hitting the sample and causing it to change, then as δt gets larger we can observe the sample at some time after the initial event.

$$I_{autocorr} \propto \int_{-\infty}^{\infty} |E(t)E(t-\tau)|^2 dt = \int_{-\infty}^{\infty} I(t)I(t-\tau)dt \tag{4.1}$$

[77,83]. The paths traveled by the pump and probe beam demonstrated in figure 4.1 are chosen such that each beam has two steering mirrors prior to the final beam splitter which is used to recombine the two beams. The steering mirrors are able to adjust the directional vector of each beam to ensure they travel collinearly through the BBO in order to obtain the nonlinear intensity response. An example of the autocorrelation response is presented in figure 4.5.

An autocorrelation signal is able to provide information about the actual pulse length generated by the laser. Ten measurements of an autocorrelation signal were averaged and fit to a gaussian peak as presented in figure 4.6. From the fit, the calculated full-width at half max of the pulsed beam accounted for a pulse length of 216 fs, as opposed to the 120 fs pulse length quoted by the laser manufacturer. There are a few user controlled parameters which are capable of altering the pulse duration of this laser. For the purposes of this project this pulse duration is sufficient to observe ultrafast phenomena so the laser settings at the time of collection of the autocorrealtion measurement are kept for the duration of this work.

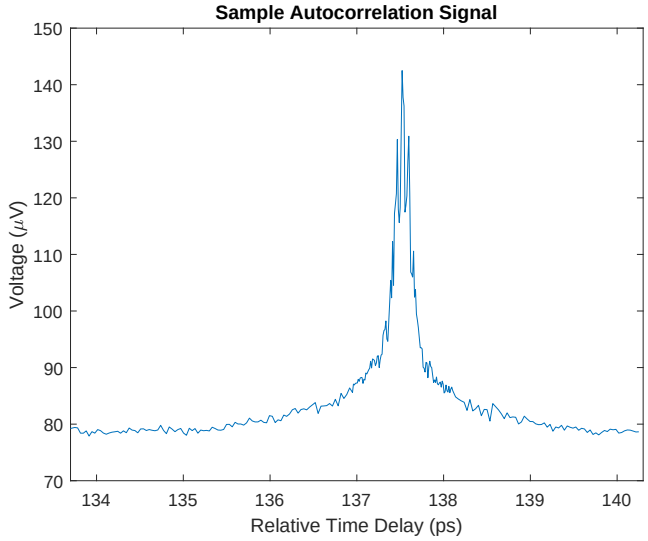

Figure 4.5: An example of a single autocorrelation measurement.

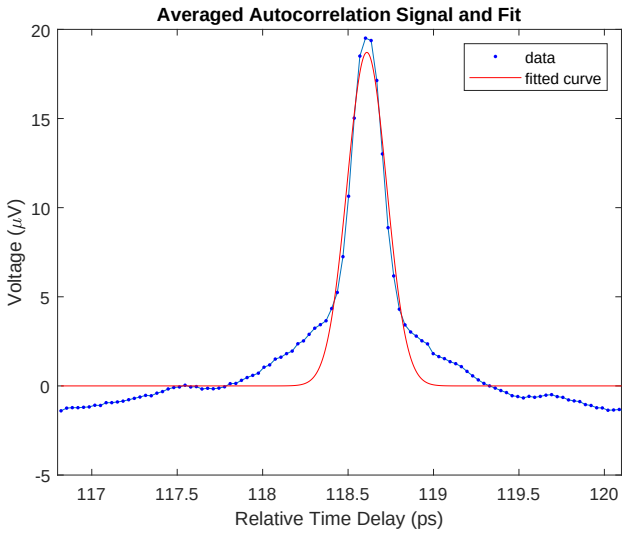

Figure 4.6: 10 autocorrelation measurements averaged with a gaussian fit with a full-width at half max of 216 fs. Note that the results were normalized to compare various scans before averaging resulting in some values below zero.

As there are two delay lines in use for this experiment, one may be used to check the step sizes of the other assuming we know the step size of one. The short delay line is of relatively high precision and each step produces a delay of 33 fs.

The large delay line has a retroreflector on a cart that is moved by a stepper motor controlled by an arduino and motor shield. Measurements were made moving the retro reflector by 1 and 5 steps, the distance measured with the short stage, then averaged to find the mean time delay per step. This data was combined and presented in figure 4.7. The steps that are on the very long and short timescale were from the retroreflector getting near one of the ends of the delay line. The height of the supports for the rail are

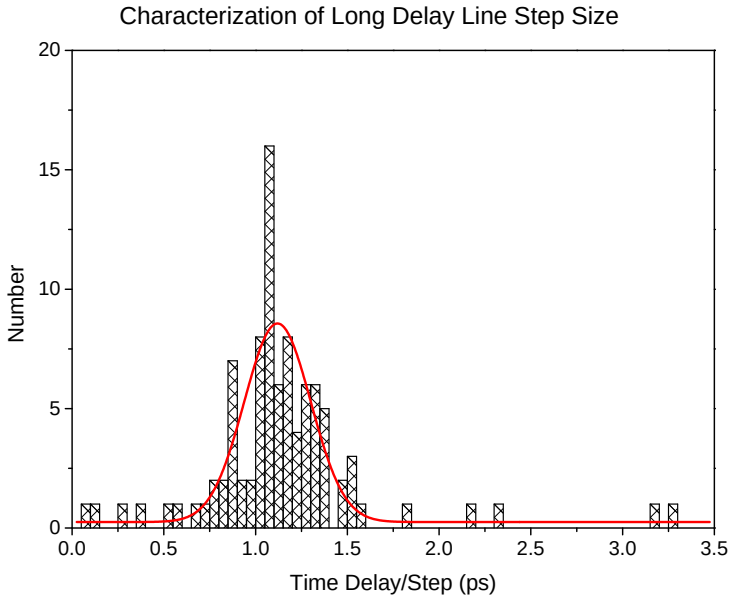

Figure 4.7: A Gaussian fit was placed on the histogram of the step size from the long delay line to determine the value and accuracy of the step sizes

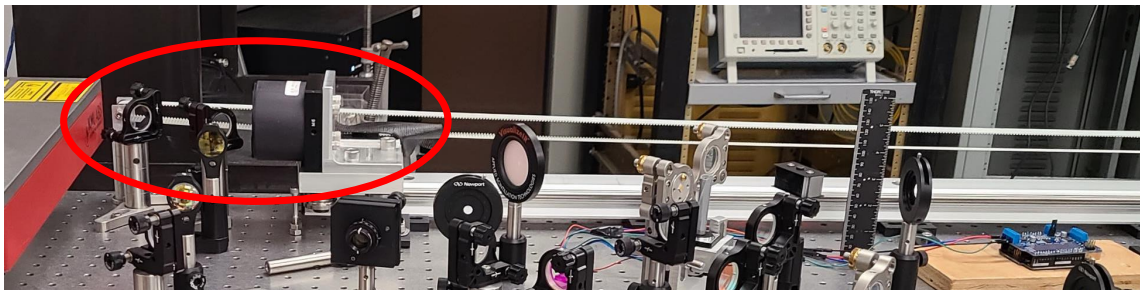

Figure 4.8: The long delay line on table, with the tension at the edge of the delay line circled.

not at the same height as the rail and so, as the cart approaches either end the tension increases, this can be seen in figure 4.8. This was solved well enough with some oil. None the less, the average step size measured with the autocorrelator was 1.1 ps per long stage step, this is the delay applied to the x-axis in figure 3.3.

From the autocorrelation measurements, it appears that each step from the long delay line causes a delay of 1.1 ps, however, when the distance is measured by hand, the expected delay per step calculated is closer to 1.4 ps. This discrepancy may be addressed with another form of autocorrelation implemented later on in the development of this project which makes use of a device known as a photoswitch.

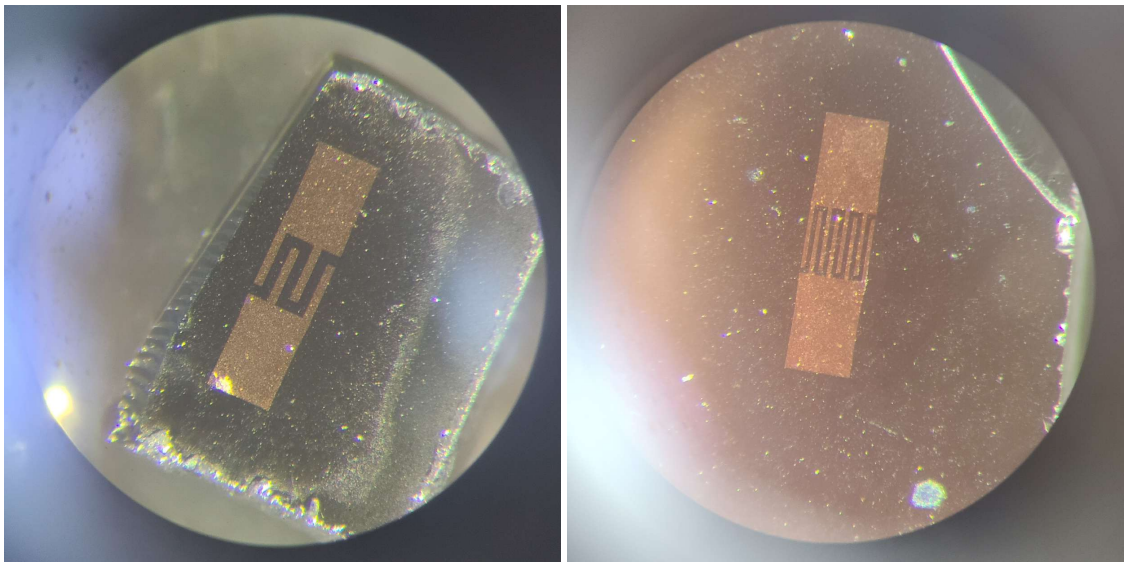

(a) **(b)**

Figure 4.9: Two different photo switches with a larger gap spacing in figure (a) and smaller spacing in figure (b).

4.3 The Photoswitch

The photoswitch (also known as an Auston switch) has turned out to be a crucial aspect of this work. In the most general terms, a photoswitch is a conductor, placed in contact with a semiconducting substrate [84, 85]. When light which has a photon energy equivalent to the band gap of the semi-conductor interacts with the photoswitch, charge carriers are freed and current is allowed to flow across the conducting material. The primary geometry for the conductor, in our case copper, is demonstrated in figure 4.9. These switches are on a Gallium Arsenide substrate which has a band gap of 1.42 eV, putting it bellow the energy of a single 515 nm photon or two 1030 nm photons [77].

The photoswitch is operated by applying voltage across the switch. Since the ends are not in contact, the measured resistance is quite high and no charges can pass from one side to the other. When a laser is incident on the switch with photon energies that can overcome the band-gap of the GaAs, charges are able to flow from one end to the other as the resistance of the circuit drops. Using a pulsed beam, this is only allowed to happen for a very short amount of time and results in a current pulse that can be read off an oscilloscope with a pulse width determined by the pulse duration of the beam and the spacing between the two halves of copper.

The design of the photoswitch with a larger gap size, seen in figure 4.9a, leads to the photoswitch being less prone to damage from the heating and voltage applied across it. This is due to the larger area on the extended teeth. Four photoswitches were used throughout this work for a variety of purposes. The photoswitch with the large gaps was used initially to test a method of magnetic pumping presented later on in reference

The photoswitches pictured in figure 4.9 are unprotected copper, making them susceptible to oxidation when heated by the ultrafast laser pulse [86, 87]. The layer of copper is already quite thin, so oxidation can lead to reduced functionality of the switch. It is necessary to protect the copper such that it is not in contact with air as it is heated to eliminate the risk of oxidation and rapid decay of the photoswitch.

The first attempt at protecting the copper switches was done through gold plating. Pure gold is typically non-corrosive so long as no water is present and so, was a good candidate for protecting the copper. An electroplating set-up from Gold Plating Services [88] was chosen for this application. Through the electroplating process, a voltage is applied to the copper so that it attracts the gold ions in a solution. When gold plating, the amount of time for which the metal is submerged in the plating solution is directly proportional to the thickness of the gold layer. The photoswitch was submerged for less than two seconds, which was enough time for the gold to not only plate to the copper, but fill the gaps between the teeth, ruining the switch by completing the circuit, this result may be seen in figure 4.10.

As the gold plating proved to result in growth too rapid to control reliably, the next option for protecting the copper against oxidation was clear nail polish. A thin layer was

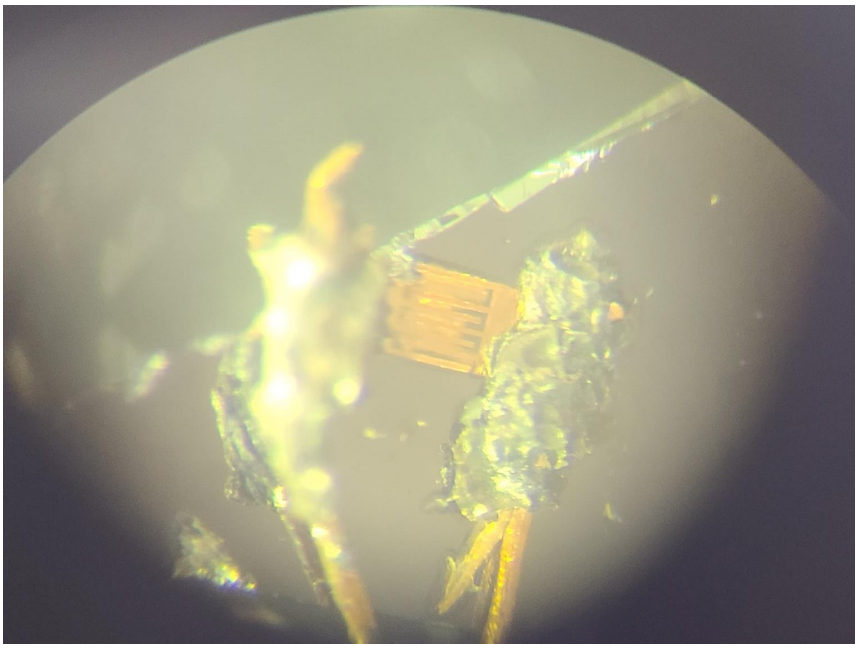

Figure 4.10: A photoswitch coated with a thin layer of gold.

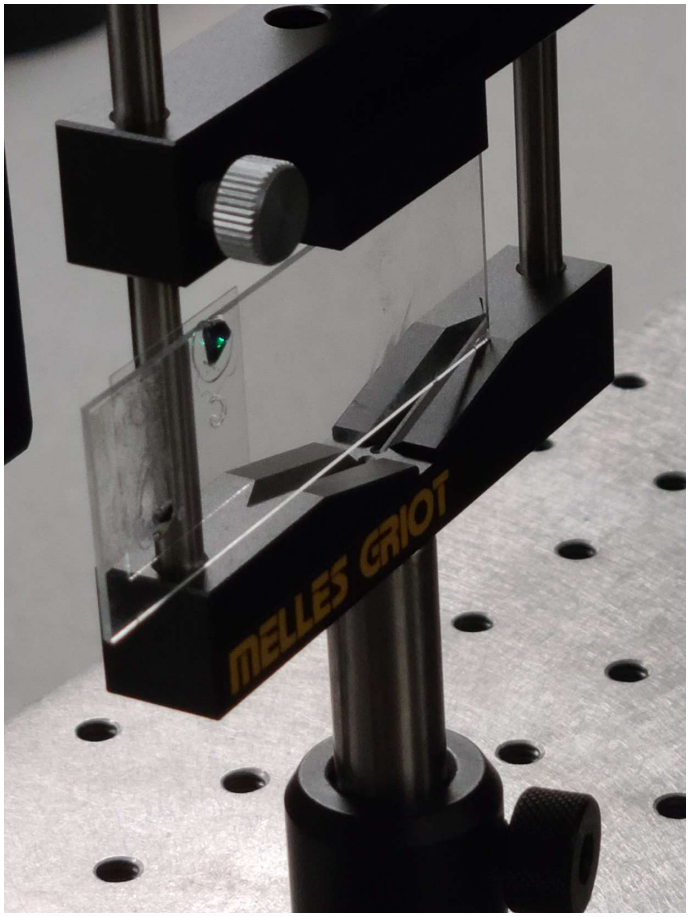

Figure 4.11: A test on the protective properties of nail polish against copper oxidation.

applied to a test piece and placed in the laser beam on a microscope slide. The pump beam as sent to the far side of the optics table in case the nail polish produced smoke which could damage optics. The beam was passed through a BBO crystal to generate green light, then to the test piece as seen in figure 4.11.

After approximately 3 Watts of laser power the nail polish appeared to turn white to the eye. Upon investigation under a microscope it was noted that the heating from the laser did not burn the nail polish (or the copper and GaAs underneath) but instead only expanded the air bubbles in the nail polish as seen in figure 4.12.

The air bubbles expanding within the nail polish upon heating is not ideal as it means air can be in contact with the copper of the switch after heating which poses the risk of oxidizing the copper. The air bubbles did require a larger amount of heat than the photo switch will typically not experience, so this appears to be the best option. For the purposes of this project at this time the nail polish is then applied in air, however, should a photoswitch be needed with more staying power, it could be applied under a Nitrogen atmosphere or vacuum to remove the air bubbles.

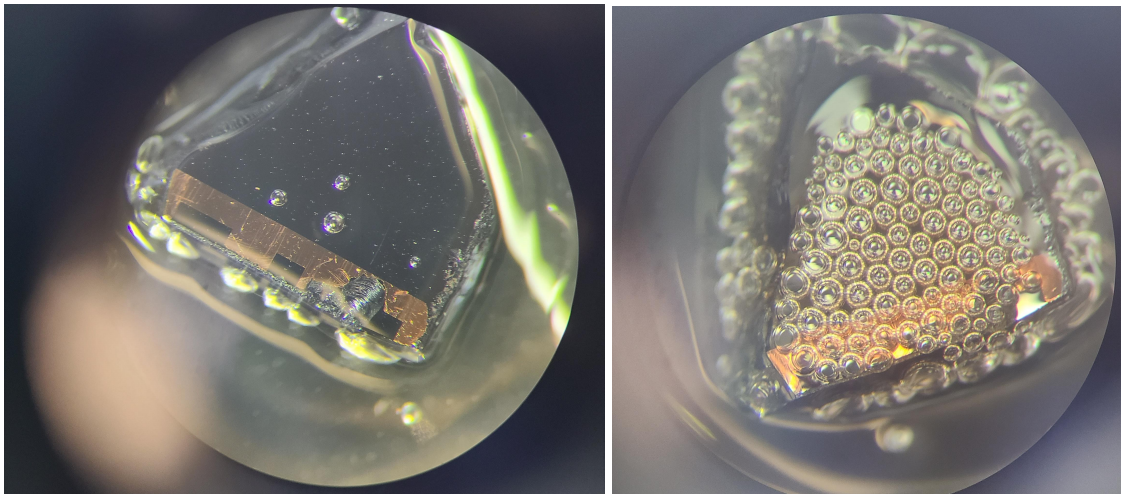

(a) **(b)**

Figure 4.12: Nail polish on a test piece of Gallium Arsenide with some copper. (a) is the nail polish before being placed in the laser beam and (b) is an image through a microscope after the photoswitch was heated with 3 Watts of power.

4.3.1 Autocorrelator

The current pulse generated by the laser interacting with the GaAs is what allows the measurement of a sort of autocorrelation with the photoswitch. When the pump and pulse beams are both incident on the photoswitch, they generate different resolvable peaks in current when passed through an oscilloscope as seen in figure 4.13. Measurements were taken with the delay line at various positions, included are snapshots from the oscilloscope with the delay line at the furthest position in figure 4.13a, dubbed the 0 ps position, at the true t_0 where the pump and probe beams hit simultaneously leading to constructive interferance of the current pulses in figure 4.13b, and at the closest position where the largest delay is obtained in figure 4.13c.

This method of autocorrelation using a photoswitch is a good diagnostic tool for determining where the expected t_0 is along the delay line, however there are a few downsides to this technique. Experimentally, it was observed that, no matter the rotation of the BBO, a large amount of the beam incident on the cryistal is not frequency doubled to green light and thus is discarded. This means that, although the efficiency of generating charge carriers using the green light is expected to be higher, within the parameters of this experiment the higher power of the IR beam typically leads to a larger response from the photoswitch, presumably through two-photon absorption. As a result, the final orientation of the apparatus for the detection of TR-MOKE, as seen in figure 4.3 can be modified by adding a mirror before the BBO, leading to a slightly shorter path length for the probe, where the photoswitch is placed in the location where a sample would typically sit.

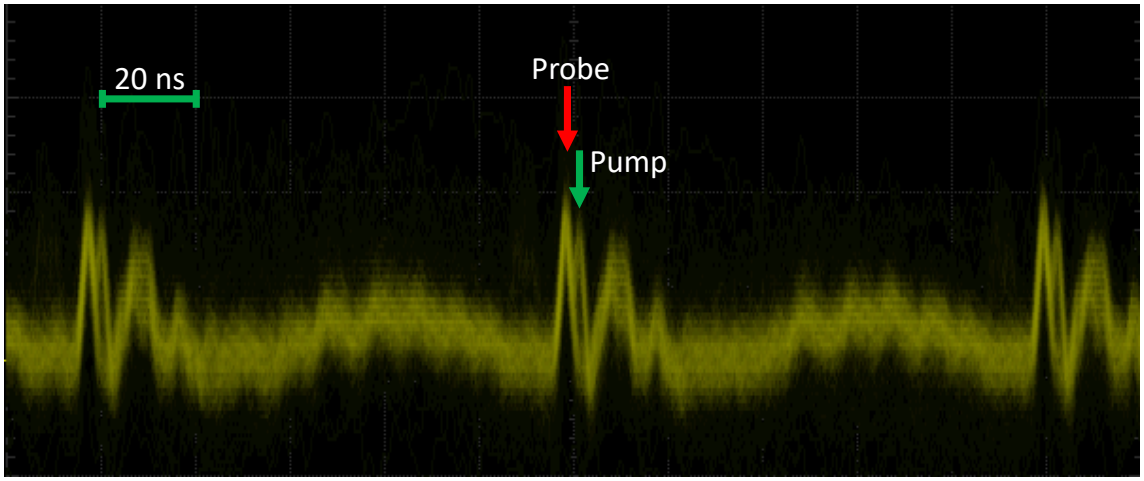

(a)

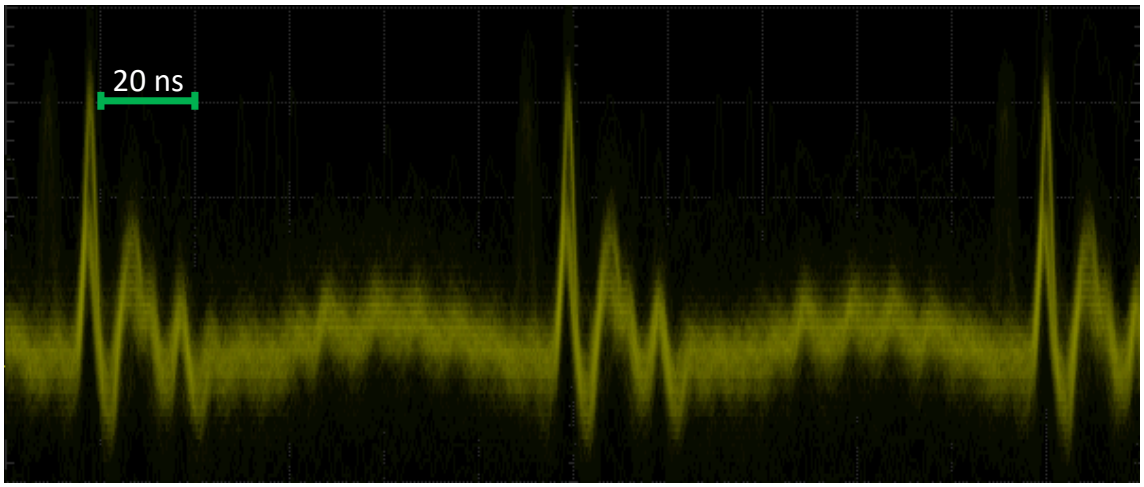

(b)

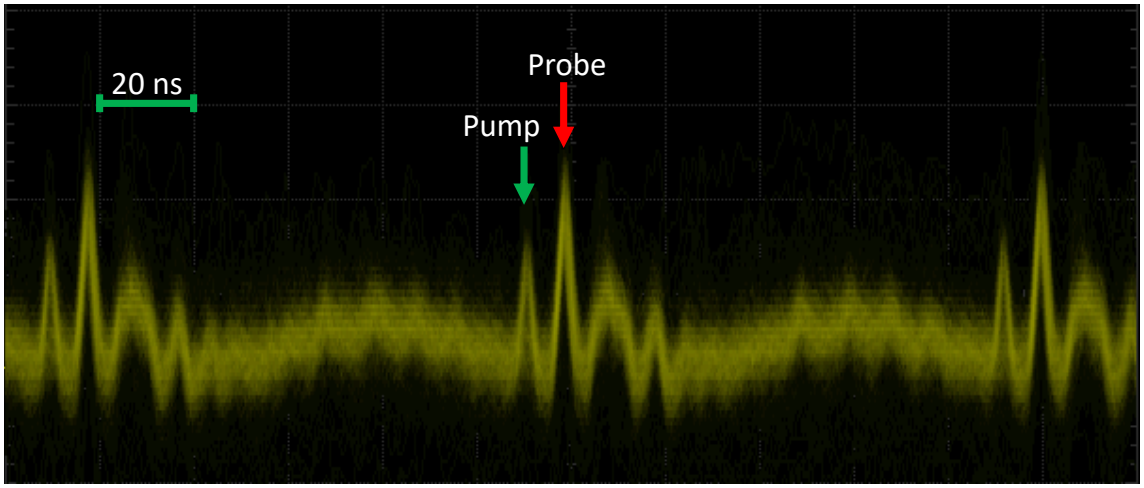

(c)

Figure 4.13: Snapshots of the current pulses generated from the pump and probe beams hitting a photoswitch. In figure (a) the pump is at it's longest path length where the pump beam interacts with the photoswitch before the probe. In figure (b) the peak is largest as the pump and probe are hitting the photoswitch simultaneously, leading to constructive interference of the currents generated by each beam, then in figure (c) the pump hits the photoswitch long after the probe.

4.4 Pumping

At this stage in the experiment, this apparatus has been able to demonstrate the ability to observe a magnetic response as well as time resolution through both the green generation autocorrelator and the photoswitch current pulses. It is at this stage where the development of this apparatus continues into the future of this project.

A background signal is present in every time-resolved measurement which changes with delay position and is many times larger than a MOKE signal could be, leading to the inability thus far to observe the TR-MOKE response as this makes it difficult to discern the difference between optimization of a signal and amplification of background. Reasonable efforts have been made to block as much of this signal as possible, however these results have been insufficient to date. The background signal manifests as a large (many times larger than a Kerr rotation) oscillating signal when the demodulation is on the pumping beam, and can lead to difficulties optimizing the signal and a lack of repeatable results when the demodulation is on the probe. All is not yet lost, however we will return to solutions to this issue in a later section.

In this section, we will discuss the three primary methods of pumping a sample to generate a Kerr rotation. These topics largely build out of the discussion magneto-dynamics in chapter 3. As we have discussed the photoswitch in some detail in this chapter, we will continue with it's application towards pumping a sample.

4.4.1 Magnetic Pumping

As we have already discussed how the operation of the photoswitch works, we may now apply this knowledge in order to magnetically pump a sample. As depicted in figure 4.14, a photoswitch is wired up with two loops of wire that may pass near a sample in order to apply a magnetic field.

As discussed previously, the copper of the photoswitches is susceptible to oxidation when heated in the presence of oxygen, for this reason indium solder had to be used due to the lower melting point to connect the wires. A combination of the indium solder being difficult to work with and the aging of the photoswitches in atmosphere lead to some difficulty in ensuring adhesion. Due to the difficulties in connecting the wires to the switch itself, the solder joints had to be tested frequently in wiring up these devices, which would occasionally result in one side of a switch lifting from the GaAs surface. This is the explanation why in the image in figure 4.15 has an extra photoswitch present.

Two methods of application for the photoswitch were designed to magnetically pump a sample. The first described previously will simply be discussed as the photo-switch as pictured in figure 4.14, the second design dubbed the "flip chip" is pictured in

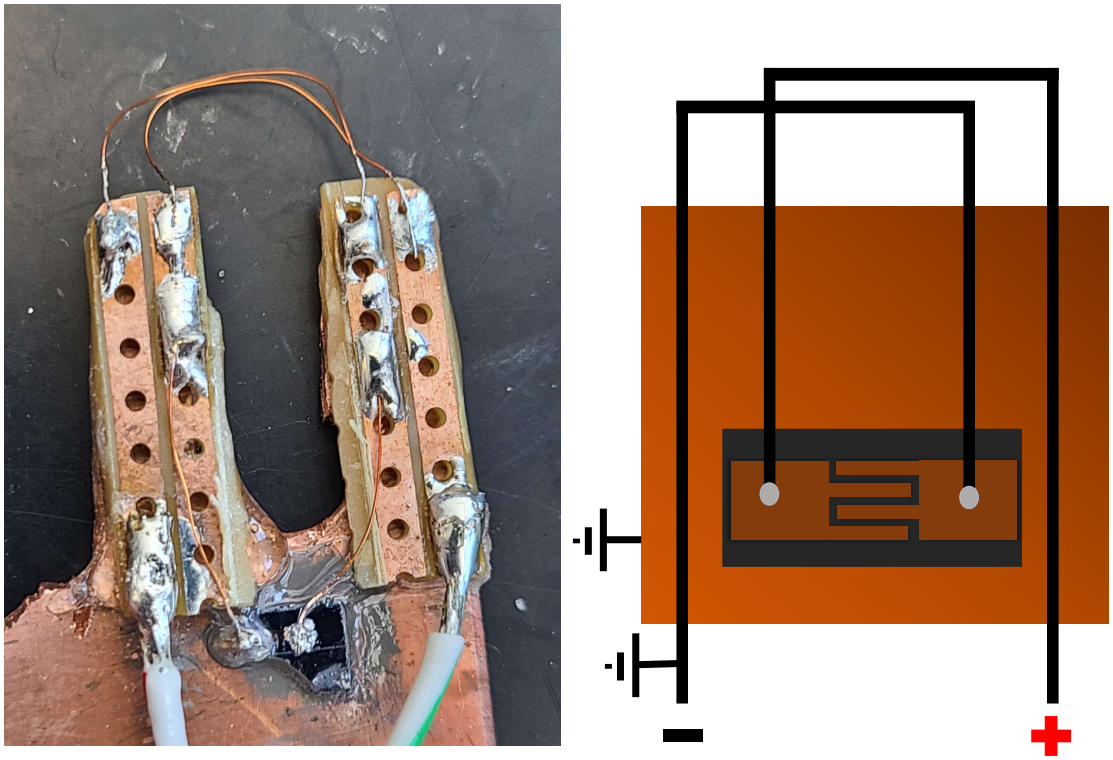

(a) (b)

Figure 4.14: A picture of a wired up photoswitch and a sketch to better describe the circuit. The wires are directed such that the magnetic field from the current passing through each one travels in the same direction such that their magnetic fields add together.

figure 4.15.

The flip chip was designed with a specific permalloy sample in mind. The sample consists of a thin layer of permalloy deposited on a piece of sapphire. With permalloys high saturation magnetization and low coercivity in addition to the layer of this sample only being 5 μm thick, the field generated by the current passing so close to the sample should be sufficient to switch the direction of magnetization. In addition, the current carrying line on the circuit board was scrapped down such that the current density in the wire is increased by the smaller current carrying area near where the sample is mounted to ensure a high magnetic field at the sample.

Considerations had to be made to ensure the highest likelihood of success in operating the flip chip. A layer of kapton tape was placed on the surface of the circuit board for the sample mounting to ensure any sharp edges from the copper would not scratch off the sample. An additional layer was placed on the sapphire to create enough space between the permalloy and the circuit board to reduce the risk of transferring the permalloy to the board. Finally a mount was printed to hold the sample in place as can be seen in figure 4.15 so the sample's position could be adjusted to keep the sample in close proximity to the portion of the circuit board carrying the current.

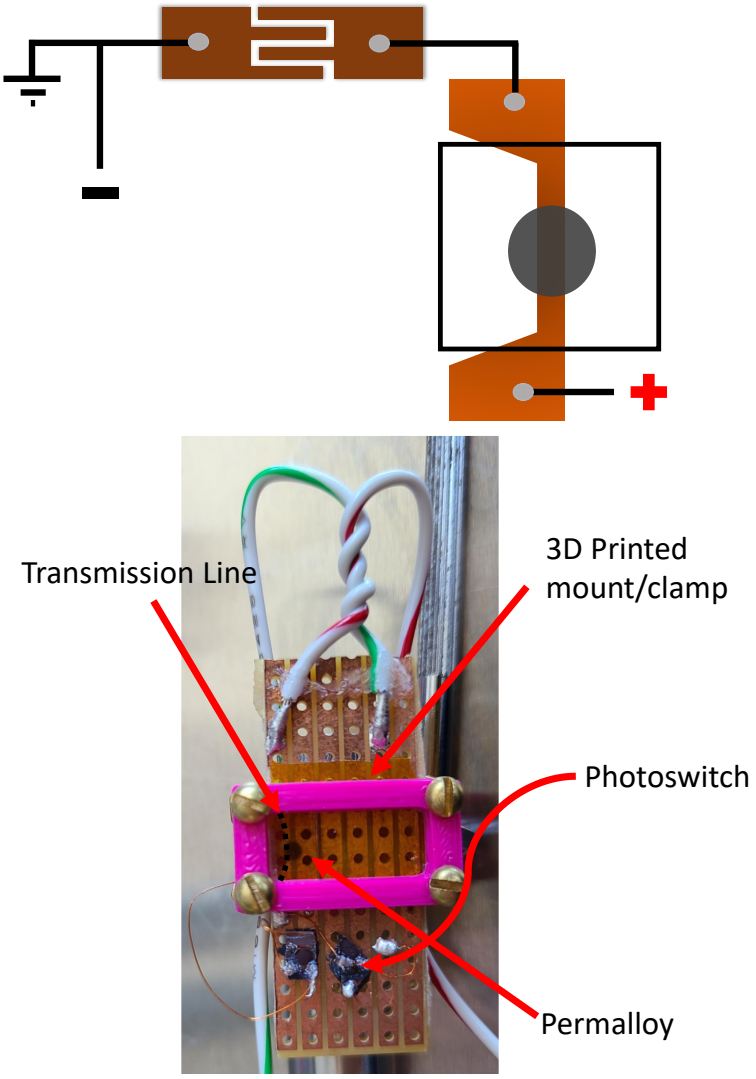

Figure 4.15: The "flip chip" consists of a photoswitch attached to a copper line that has been tapered down to increase current density as the current passes near the permalloy sample. The permalloy is a 5 μm thin film on a piece of sapphire, permalloy side down for close contact to the passing current for the largest possible field generated.

Due to the difficulties in obtaining good electrical contact for the wiring of the photoswitch, each one has to be tested with the oscilloscope to observe the operating voltage for a given laser power where the current generated is maximized without damaging the photoswitch.

The ultrafast laser pulse interacts with the GaAs layer to free charge carriers so that current may travel to cause a magnetic field. The field generated will not only last the 200 fs of the laser pulse duration, but will be instead distorted by the resistance of the circuit and the distance the current travels. The expected phenomena from these devices will then last on the order of nanoseconds, causing the generation of slow spin waves. This is characteristic of Permalloy as we've touched on previously.

4.4.2 Heating

The magnetization of a sample is directly influenced by the samples temperature. Above the Curie temperature, for instance, magnetic order changes and a sample may become demagnetized. By heating a sample with an ultrafast beam, we may induce some degree of demagnetization over longer time scales with multiple laser pulses, or ultrafast time scales with a single pulse, as is the case with ultrafast demagnetization as discussed in chapter 2. Both cases will be observable through applying the apparatus developped through this work.

4.4.3 Circularly Polarized Pumping

The final form of optical pumping is through a circularly polarized beam. Without realignment of any sort, a quarter waveplate may be added following or preceding a measurement with linearly polarized light on a sample. Without effect on the alignment of the apparatus, we are able to shift focus from ultrafast heating to the study of the inverse Faraday effect. In this way we are able to compare the characteristic times resulting from multiple pumping methods for a given sample to provide detailed characterization describing the impact of each form of excitation.

Chapter 5

Time-Resolved Spectroscopy

The status of this apparatus at the conclusion of this work is not where modifications to the experiment end. This apparatus is designed such that it may be reconfigured with minimal effort to complete additional measurements outside of the time-resolved magneto-optical Kerr effect. The first modification to this apparatus was completed through the collection of time resolved IR spectroscopy. Through a collaboration with the Research group of Professor Dave Herbert at the University of Manitoba we studied the time-resolved absorption of IR light passed through a solvent containing an Fe(II) complex of phenanthridine/quinoline diarylamido ligand which has been found to demonstrate absorption in the visible range with a 3 ns excited state lifetime [89]. Previous spectroscopy had been completed over 500 to 800 nm light, so detailed spectroscopy of a higher wavelength, as is possible through the laser applied to this work, may be useful in determining the quality of the model used by this group to describe the behavior of these Fe(II) complexes.

This chapter aims to demonstrate preliminary results for the molecules obtained through this collaboration and demonstrate the ability to modify the apparatus of this work for additional measurement techniques.

5.1 Alterations to the Apparatus

The aim of the versatility of this apparatus is that it be relatively simple to switch from one measurement method to another. We will begin by discussing the initial modifications that must be made in order to complete spectroscopy measurements.

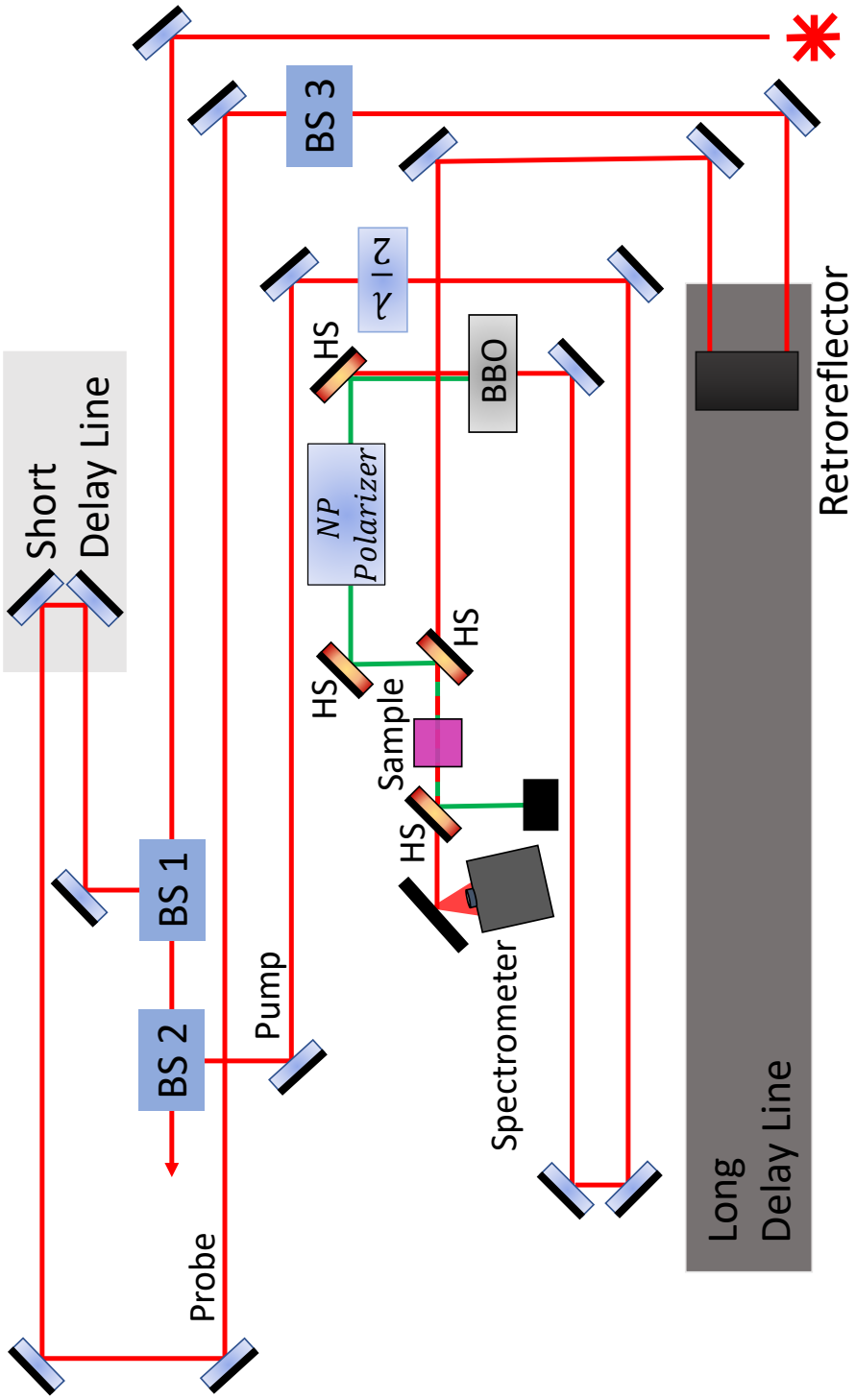

Figure 5.1: The setup for time-resolved spectroscopy measurements. BS 1 through 3 are the beam splitters used. BS 1 and 2 are 90:10 and 80:20 respectively, then BS 3 is an 80:20 beamsplitter to reduce the beam down to closer to the power of the other beam. HS are harmonic separators to transmit IR and reflect visible light.

Modifications from figure 4.3 are made such that the pump and probe are passing through a liquid sample collinearly before the probe is passed to a STS-NIR Miniature Spectrometer from Ocean Optics. The spectrometer applied to this experiment is sensitive to IR and operated using its accompanying software. The alignment for the time-resolved spectroscopy measurements is presented in figure 5.1. For the Fe(II) molecules in particular, we are interested in the effect of the green absorption exciting the sample, so the beam which would typically be used as the probe is instead applied as the pump to this experiment. The IR beam used typically as the pumping beam and now as the probe, then has to be reduced in power using a beamsplitter to eliminate the possibility of the probe heating the sample significantly.

In addition to completing spectroscopy of the samples, we may additionally study the total transmission through these samples using a power meter. This eliminates the ability to determine which wavelengths may be absorbed, however, since the laser is using a relatively narrow bandwidth, we are able to use the added benefit of the demodulated signal to determine if any absorption is occurring. For the intensity measurements the same power meter as the intensity autocorrelation measurements completed in chapter 4.2 is applied. This power meter is sensitive to both IR and visible light, so a harmonic separator is placed to intercept the collinear beams to eliminate the visible pump at the detector.

When the probe passes through the sample, the beam is displaced slightly by the precise sample position. Every time the sample is removed and replaced, this displace-

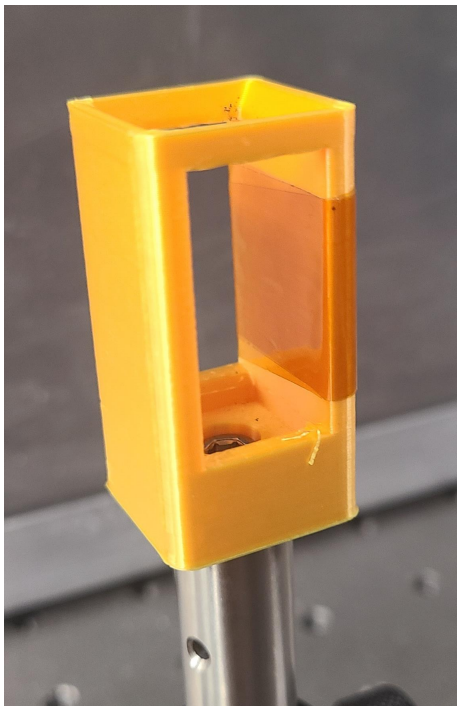

Figure 5.2: The 3D printed holder for the molecule spectroscopy measurements.

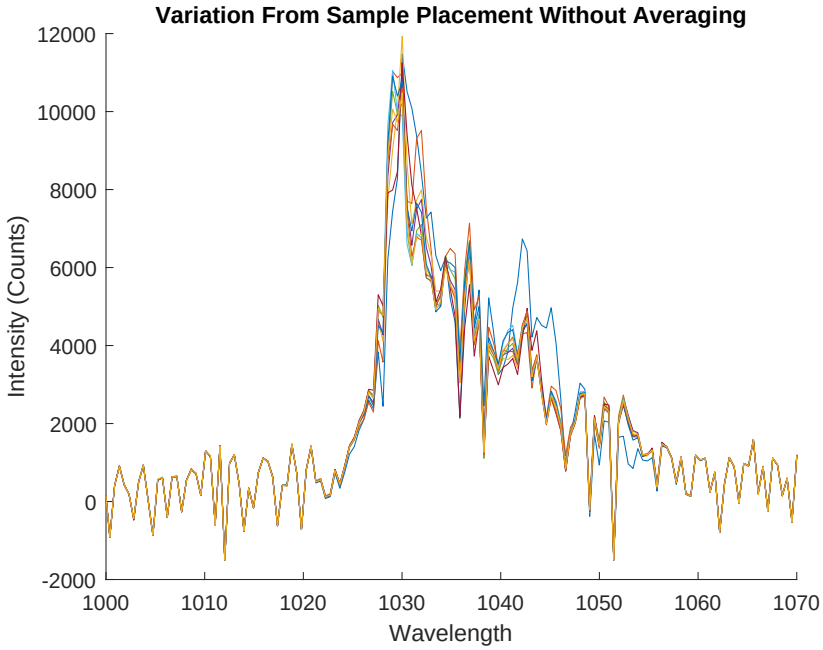

Figure 5.3: The Blank sample was removed and replaced repeatedly in the sample holder to check the repeatability of the resulting spectrum. Each spectrum plotted is a single, long exposure measurement. The counts have been background subtracted such that they average to zero.

ment alters the observed spectrum, so a holder was designed and printed to reduce variability in sample placement. Kapton tape was added to one side of the holder to reduce the space between the holder wall and the cuvette containing the sample to ensure a snug fit and increased repeatability. This 3D printed sample holder may be seen in figure 5.2.

The printed holder was tested by removing the sample from the holder, placing it back in and taking a single measurement. The integration time for the measurements was chosen such that the maximum neared the saturation value for the spectrometer but did not reach it and each measurement is a single snapshot, not an average over multiple measurements. The results to this test are presented in figure 5.3.

From figure 5.3 it is clear that the holder does a reasonable job of reducing variance in the sample from the placement. Only one of the ten measurements displayed any real shift in the spectrum and even this is relatively minor. As the results are averaged over many measurements, we can then reliably begin to look for trends in the results time-resolved spectroscopy results.

In order to ensure the spectrometer was not over-saturated, the light following the sample was not sent directly to the spectrometer, but instead was reflected off an anodized aluminum beam block. The same beam block was used throughout and the spectrometer was then angled towards the block to maximize the observed signal.

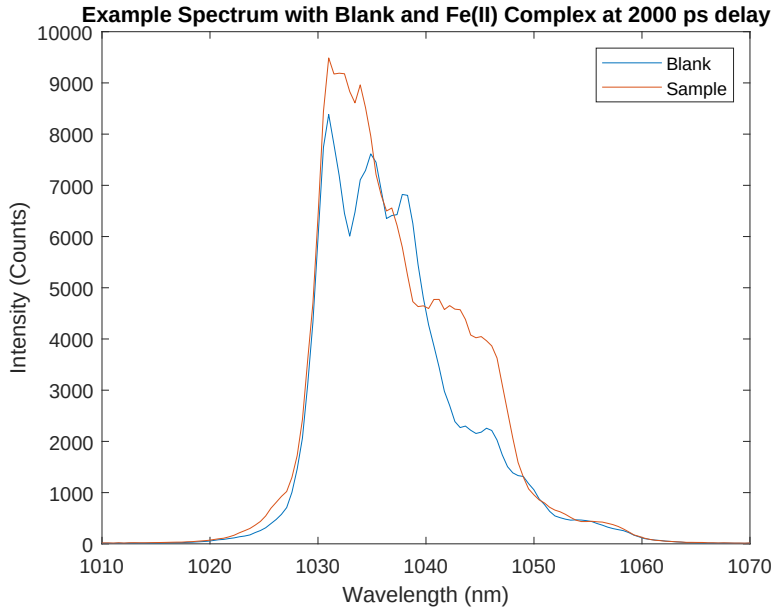

Figure 5.4: An example spectrum of the Fe (II) complex and the blank solvent.

5.2 Results

A large number of measurements were taken for these samples as the expectation of low absorption led for the need to be thorough in the measurement techniques.

To begin, figure 5.4 demonstrates an example spectrum for the Fe (II) complexes. Comparing the recorded spectrum to the expected laser spectrum presented in reference 3.1, there are a few notable differences. The output laser spectrum has a step-like shape at the edges near 1027 nm and 1059 nm. The collected spectrum from the oceanview spectrometer instead demonstrates a slower increase before 1010nm and a sloping decline from 1050 to 1070 nm. It was noted during setup that the spectrometer that the angle it was positioned at affected the generated spectrum. The spectrum displayed using the oceanview software did not only change in amplitude but overall shape with changing the angle of the spectrometer to the beam. It is for this reason that the resulting spectrum can only be compared directly with other changing parameters such as laser power and time delay, but not analyzed in detail on its own.

Figure 5.4 presents the spectra generated by light transmitted through the Fe (II) complex and the blank solvent. The time delay is demonstrated with respect to the long delay line, the expected delay where the path lengths of the pump and probe are equivalent for the apparatus is at 1206 ps. The real delay with respect to the beam of these spectra is then 794 ps. If IR absorption occurs over the bandwidth of the laser, at this delay it should be visible as absorption has been observed for up to 3 ns for these Fe (II) complexes [89]. The variations in spectra between the sample and blank presented

in figure 5.4 are not consistent features observed upon repeatedly alternating between study of the sample and blank, so the spectra may only be compared by changing parameters such as laser power and time delay, but not directly to one another due to this lack of repeatability.

In order to study these samples they were suspended in toluene and the concentration chosen such that they are somewhat transparent to IR. Spectroscopy measurements were taken by varying the laser power from 5 to nearly 17 Watts of total laser power, however, due to the chosen pump configuration for minimal alterations to the overall apparatus, this actually lead to pump values between 400 mW and 1.3 W. For each power, the time delay was altered from the 0 ps position to a maximum delay of 10.7 ns. The results from these measurements on both the Fe (II) sample and the blank containing only the solvent are presented in figures 5.5 and 5.6.

Additionally, transmission measurements were completed on the Iron(II) molecules with and without the pump, these are presented in figure 5.7.

The spectroscopy data of each type was normalized to the minimum power using a normalization factor

$$N_{\text{norm}} = \frac{N}{N_{\text{max}}(N_{\text{min Power}}) \times (P_{\text{current}}/P_{\text{min}}))}, \tag{5.1}$$

where P is the power and N is the number of counts. This normalization allows for a comparison between the results at different powers. Comparing the results of the spectroscopy and the transmission, it does appear as if there is some absorption occurring as demonstrated by the increased transmission without the pump present, however, once again there is a significant background present. Subtracting the background from the data and taking the absolute value gives the results presented in figure 5.8.

These results are noisy and require more tests to be run. It appears as though there is an increase in transmission (although very small) approximately 2 ns after the excitation, followed by a decrease in transmission for the following 6 ns. It is worth noting that these results are noisy and the background may not have been entirely accounted for in the subtraction. In order to confidently analyze these samples, more measurements are needed along with further minimization of background reflections.

Finally, presented in figure 5.9 are the transmission results from the spectroscopy measurements, summing over all wavelengths and averaging all powers after the normalization has been done. These results show clearly that more work is needed as the cross-over of the transmission between the blank and Fe (II) counts seems to suggest some absorption, although minimal, there is also a large discrepancy in the counts before t_0 suggesting either the normalization is insufficient for comparison or a large uncertainty in the results.

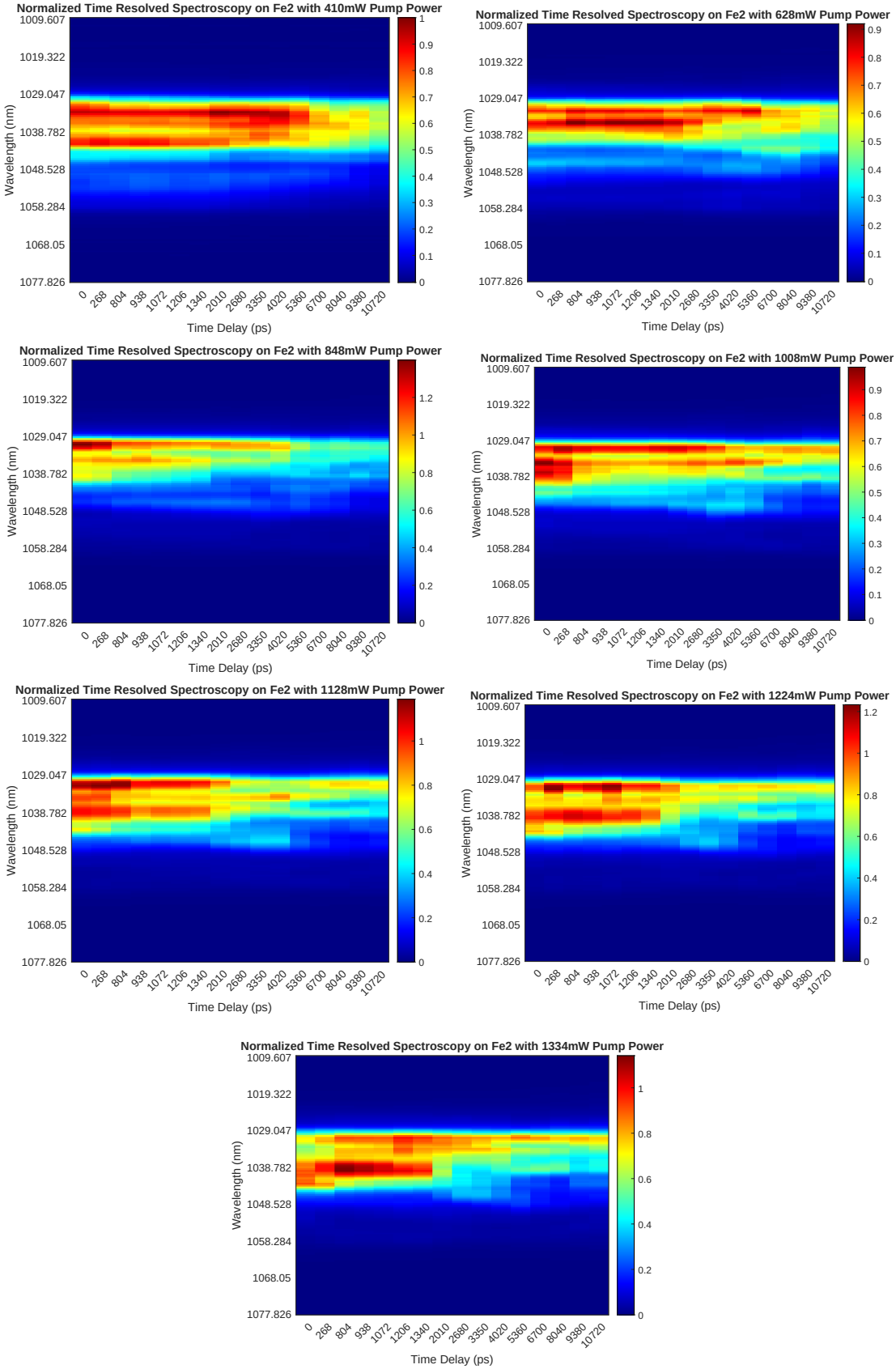

Figure 5.5: The spectroscopy of the Iron-2 molecules with time resolution at different laser powers. The powers varied up to the maximum possible in 10 MHz mode.

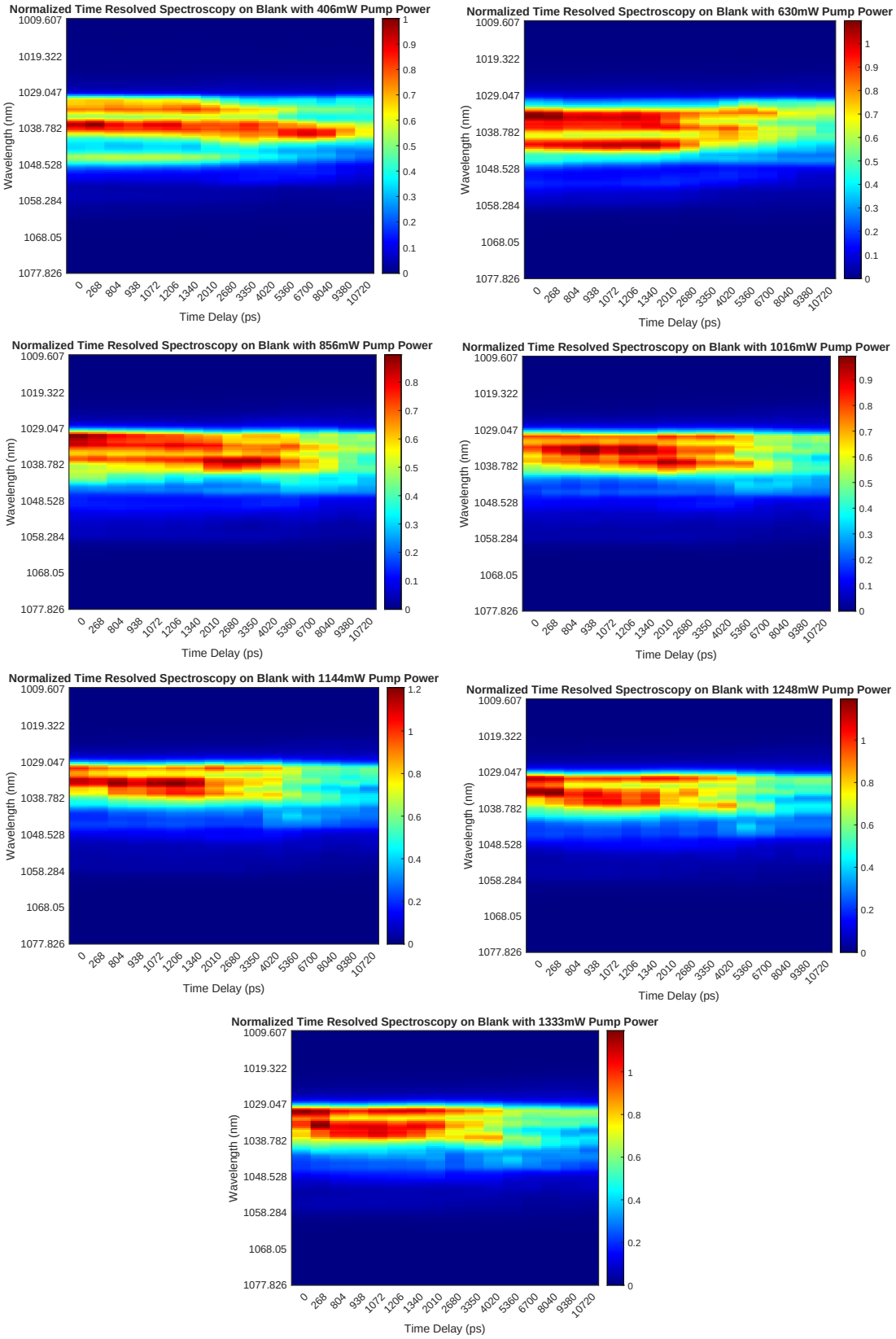

Figure 5.6: The spectroscopy of the Iron-2 Blanks with time resolution at different laser powers. The powers varied up to the maximum possible in 10 MHz mode.

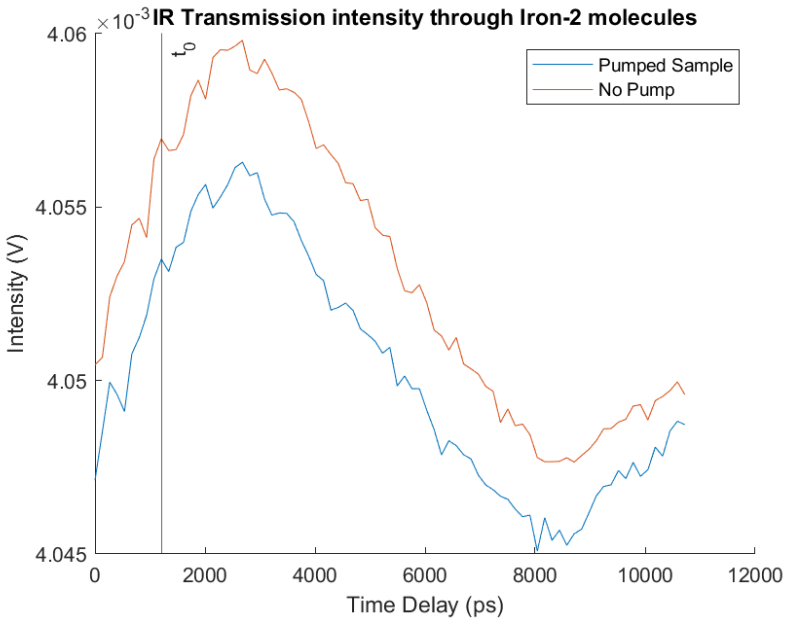

Figure 5.7: The transmission intensity through the Iron-2 molecules under the influence of the pump and without it.

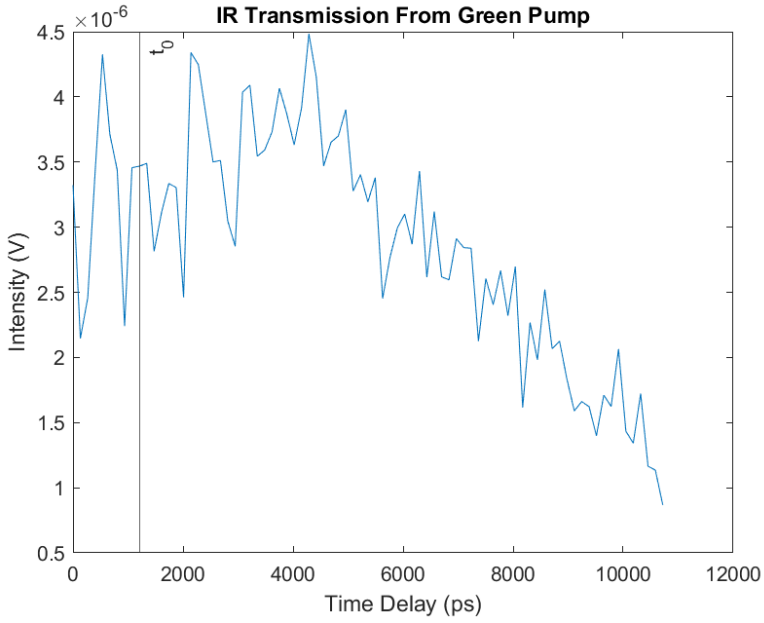

Figure 5.8: The difference data between the measurement of transmission of through the Fe(II) molecules. The difference is taken between the transmission with and without a pump incident on the sample.

5.3 Future Development

The aim of this chapter has been to demonstrate the versatility of this apparatus and its ability to complete IR spectroscopy measurements with only minor adjustments. This goal has been accomplished, and there is more work to be done.

The expectation for these samples, given by the model presented in reference [89],

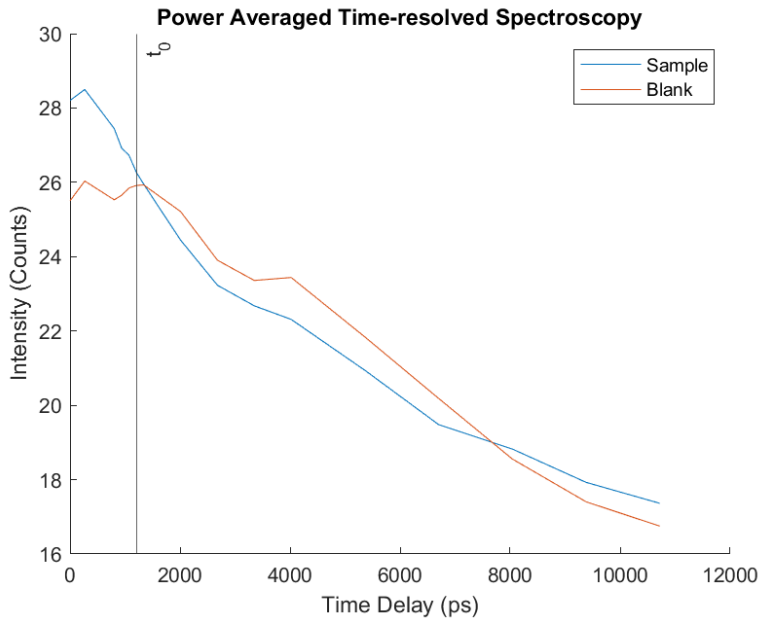

Figure 5.9: Wavelength summed IR transmission from Fe(II) and blank.

was that there would be only a small amount of absorption within the wavelength bandwidth of our laser. The results appear to show some absorption by the Fe (II) complexes and more measurements are needed in order to obtain confidence in these results.

The first step towards improving the quality of the spectroscopy measurements is to obtain a sample for which we expect a notable absorption in our observable IR wavelength range under either a green or IR pump. Comparison of a small absorption result for the molecules measured in this chapter to a sample with a notable response would lend credibility to the results.

There is a clear and significant background reflection present in all of the data for these molecules. The efforts being taken to reduce background reflections for TR-MOKE should have a positive impact on the spectroscopy measurements as well by increasing the quality and quantity of light shielding.

Rather than using the oceanview mini spectrometer, it is possible to build one. A spectrometer may be developed, rather simply, using a diffraction grating to split the wavelengths of light and a delay line to scan over these wavelengths with a photo diode. With this system, the light may be demodulated using a chopper and lock-in amplifier to reduce background effect.

Chapter 6

Conclusions and Future Work

Throughout this thesis we have built up an understanding of the modern study of magnetism and worked through the steps towards the completion of the development of a time-resolved magneto-optical Kerr effect magnetometer capable of measuring magneto-dynamics from GHz to THz frequencies.

We have worked through much of the physics describing the alteration of the polarization of a laser beam in order to understand many of the decisions made through the development of this apparatus. Alterations were made to the long delay line to improve its linearity and a retroreflector was used in order to streamline the alignment procedure.

We observed the first instance of a magneto-optical Kerr rotation for this apparatus using a magnet attached to a stepper motor. This portion of the apparatus has a number of modifications which could lead to the use of the DC MOKE signal as a proper quantitative measurement. For a first order improvement, the magnet may be characterized with a hall probe at a given distance. This characterization has a large uncertainty steaming from the mounting of the magnet to the stepper motor as well as the mounting of the stepper motor itself which allows for variation in the angle of the magnet relative to the sample.

An alteration to improve the quality of the DC MOKE measurements for quantitative characterization could be accomplished by instead placing a solenoid around or near the sample such that the the magnetic field is both controllable in amplitude and direction. This would allow for the quantitative assessment of the saturation magnetization and coercivity at room temperature of these samples during the primary optimization of the detection polarizer.

We have demonstrated, through two methods of autocorrelation, the ability for this apparatus to observe time resolution through pump-probe methods. The proof of both the ability to observe a Kerr rotation and time-resolution lead to the distinct expectation

that this apparatus should be capable of observing a TR-MOKE signal. The only factor not yet accounted for is the fluence of the pump beam to alter the sample, however, the fluence available through the laser applied to this research is comparable to that used in other TR-MOKE research. There is then a reasonable expectation that this apparatus will be capable of observing this effect once the background reflection has been sufficiently reduced.

Efforts are being made to apply a number of techniques in order to eliminate the background reflection at the detectors. Attempts have been made to block all possible reflections on table, however this signal persists. To eliminate the background effects, work is being done to implement a dual-frequency chopper for demodulation of both the pump and probe beams at different frequencies. The demodulation setting is made such that the signal detected by a lock-in amplifier must contain both frequency components.

In additions to the steps taken towards observing the time-resolved magneto-optical Kerr effect, we have demonstrated the versatility of this apparatus through the time-resolved spectroscopy of Fe (II) complexes. Additional measurements are needed and a scheme has been proposed to develop a spectrometer which will implement demodulation to reduce the background which complicated these measurements as well.

The development of this apparatus to study the time-resolved magneto-optical Kerr effect with a dual-delay line configuration has proven to require the consideration of many subtle components. Work is well under way to resolve the background reflection which has, thus far, prevented the observation of a TR-MOKE signal. Once this work is completed this apparatus is primed to easily observe the effects of ultra-fast heating, helicity dependent magneto-dynamics through a circularly polarized pump, and direct magnetic pumping. All of these methods can be applied to a single sample with relative ease due to the care taken in planning out the orientation of the set-up along with the work described throughout this thesis.

Appendix A

Matlab Code

Throughout the development of this apparatus a Zurich Instruments MFLI lock-in amplifier was used and the code for automation of the data collection was written for each step. What follows are the functions written throughout this work towards automation of the collection of a TR-MOKE measurement.

The code to set up a TR-MOKE measurement:

```
function [par] = Christie_TRMOKE_Setup()
%Set up all user/device specific information. Check these to be
    valid
%before starting a measurment.

%User specific
par.Directory = ''; %Directory Path

%Date specifics
par.Date = '';
par.StartTime = '';

%Measurment specifics
par.NumScans = 1;%
par.BigStep = 1; % Yes or no take long stage steps. If no will take
     short stage steps
par.StepPos0 = 0; % Starting position of stage that is not in
    motion.
par.BothDirections = 0; % Yes or no to move in both directions
par.Offset = 0; % If the long stage is not starting at zero
    position this
```

```
18 %should be the number of steps forward it starts at.
19 par.FileName = ''; % Leave as empty for automatically generated
       name
20 par.StepSize =10;
21 par.Distance = 8000; % Total number of steps to travel max 8000 for
        long stage, 9000 for short
22 par.FreqPlot = 10; % Set the frequence with which plots will be
       made during a measurement
23 par.Power = '';
24 par.Sample = '';
25
26 par.Notes = ''; % Anything else to say? This will become a file
       name.
27
28 %General Setup Info
29 par.ShortStage_Callibration = 0.033; % picosecond delay time
       callibration
30 par.LongStage_Callibration = 1.34; % picosecond delay time
       callibration.
31
32 %Measurment Details
33 par.TC = 0.03;%Time Constant
34 par.BurstTime = par.TC *10; %Define how long to measure as x* the
       time constant
35 par.TimeDelay = par.TC *10; % Time delay after moving stages (
       either one).
36 end
```

The code to initialize the lock-in amplifier:

```
function Christie_TRMOKE_InitZiDAQ(par)
%Initialize the Zurich
clear ziDAQ;
%path will change depending on where on the computer in use the drivers are stored
run('path');
%connect to MF instrument run on the local machine with API level 6 which is optimal for an MF instrument
ziDAQ('connect', 'IP address', 8004, 6); %This IP address can also be entered into the browser to
%use the web interface for communication.

%set to an external reference (aka lock in to the chopper frequency connected to aux ref 1)
ziDAQ('setInt', '/dev3683/extrefs/0/enable', 1);
ziDAQ('setInt', '/dev3683/demods/1/adcselect', 8);
ziDAQ('setInt', '/dev3683/demods/0/adcselect', 0);

%Enable the measuring of the beam power separately through aux 2
%ziDAQ('setInt', '/dev3683/demods/0/adcselect', 9);

%Set the detected signal to be a difference measured between polarizations.
ziDAQ('setInt', '/dev3683/sigins/0/diff', 1);

%Set the time constant and the rate.
ziDAQ('setDouble', '/dev3683/demods/0/timeconstant', par.TC);
ziDAQ('setInt', '/dev3683/demods/0/order', 3);
ziDAQ('setDouble', '/dev3683/demods/0/rate', 1000);

end
```

The code to collect a single averaged measurement:

```
function [Data] = Christie_TRMOKE_Measure_WSig(par)

device = 'dev3683';
BurstDuration = par.BurstTime;
NumCols = 3000*BurstDuration;

ziDAQ('setDebugLevel', 0);
read_count = 0;
%Create an instance of the Data Acquisition Module.
h = ziDAQ('dataAcquisitionModule');
% Configure the Data Acquisition Module.
ziDAQ('set', h, 'device', device);% Set the device that will be
    used for the trigger
ziDAQ('set', h, 'type', 0);% Specify continuous acquisition (type
    =0).
ziDAQ('set', h, 'grid/mode', 2);%Linear interpolation
ziDAQ('set', h, 'count', 1);% 'count' - Specify the number of
    bursts of data
ziDAQ('set', h, 'duration', BurstDuration);% 'duration' - Burst
    duration in seconds.
ziDAQ('set', h, 'grid/cols', NumCols);% 'grid/cols' - The number of
     points within each duration.
%    This parameter specifies the number of points to return within
    each
%    burst (duration seconds worth of data)

demod_path = ['/' device '/demods/0/sample'];

%Define signal path info in a way I don't understand but that does
    work.
signal_paths = {};
signal_paths{end+1} = [demod_path, '.r'];
%While the aux ports are labled 1 and 2 on the box, for coding they
     are 0
%and 1.
% signal_paths{end+1} = [demod_path, '.auxin1'];
```

```
29 data_path_lookup = containers.Map();
30 data_path_lookup([demod_path, '_r']) = @(data) data.(device).demods
       (1).sample_r;
31 % data_path_lookup([demod_path, '_auxin1']) = @(data) data.(device)
       .demods(1).sample_auxin1;
32
33
34 data = containers.Map();%%%
35 data([demod_path, '_r']) = {};
36 % data([demod_path, '_auxin1']) = {};
37 ziDAQ('subscribe', h, signal_paths{1});
38 % ziDAQ('subscribe', h, signal_paths{2});
39
40 ziDAQ('execute', h);
41
42 while ~ziDAQ('finished', h)
43
44     [data] = read_data_update_plot(h, data, signal_paths,
          data_path_lookup);
45     read_count = read_count + 1;
46     pause(0.05);
47
48 end
49 [data] = read_data_update_plot(h, data, signal_paths,
       data_path_lookup);
50 ziDAQ('clear', h);
51
52 %Get the data saved in a map container.
53 r=data('/dev3683/demods/0/sample_r');
54 Data=0;
55
56 %Get power saved in map container?
57 % r_other = data('/dev3683/demods/0/sample_auxin1');
58 % Data_other = 0;
59
60 %Average over all bursts.
61 for j = 1:length(r)
```

```
62      r_avg=mean(r{1,j}.value);
63      Data=Data+r_avg;
64
65  %       r_other_avg = mean(r_other{1,j}.value);
66  %       Data_other = Data_other + r_other_avg;
67  end
68
69  Data=Data/length(r);
70  % Data_other=Data_other/length(r_other);
71
72  end
73
74  function [data] = read_data_update_plot(h, data,signal_paths,
        data_path_lookup)
75  % Read the acquired data out from the module
76
77  data_read = ziDAQ('read', h);
78
79  % Loop over all the subscribed signals:
80  for ii=1:length(signal_paths)
81
82      % Replace e.g. '.x' with '_x'
83      signal_path = strrep(signal_paths{ii}, '.', '_');
84
85      if ziCheckPathInData(data_read, signal_path)
86
87          f = data_path_lookup(signal_path);
88          signal_bursts = f(data_read);
89          % Loop over all the bursts for the subscribed signal. More
                than one burst may be returned at a time, in
90          for n=1:length(signal_bursts)
91              signal_burst = signal_bursts{n};
92
93              %tmp is inefficient because it helps store each
                    measurement in
94              %the data map. I don't know enough about maps to make
                    this
```

```
                %better.
                tmp = data(signal_path);
                tmp{end+1} = signal_burst;
                data(signal_path) = tmp;
            end
        end
        pause(0.01)
    end
end
```

The code to save matlab data as a text file :

```
function Christie_Save2txt(Data, Directory, Savename, Direction)
datSavename = strcat(Directory, Savename, Direction, '.txt');

TimeDelay = Data(1,:).';
Signal = Data(2,:).';

T = table (TimeDelay,Signal);
writetable (T, datSavename);

end
```

The code to run a TR-MOKE measurement in full:

```
function Christie_TRMOKE()
%Collect TRMOKE measurments. See setup function for any and all user input
%parameters and see initZiDAQ function for zurich optimization needs.
%Currently set to either scan over the short or long delay lines although
%the actual time delay needs to be considered. If extending path length on
%the long stage we are lengthening the time delay. When increasing the step number
%of the short stage we are shortening the pump path length and so
%shortening the time delay.

[par] = Christie_TRMOKE_Setup;

statement = strcat('This scan will take ~', num2str((par.Distance/par.StepSize)*0.055), ' minutes to complete.');
disp(statement);
%% Set up the directory information to save data.
%Check if a folder exists in the directory with the date, else create one.
if ~exist(strcat(par.Directory, par.Date), 'dir')
    mkdir(par.Directory, par.Date);
end

par.Directory = strcat(par.Directory, par.Date, '\');
if ~exist(strcat(par.Directory,par.Notes), 'dir')
    mkdir(par.Directory, par.Notes);
end
par.Directory = strcat(par.Directory, par.Notes, '\');

%Generate a file name if a specific one has not been defined by the user.
if isempty(par.FileName)
    %Create file name based off input parameters.
```

```
29      par.FileName = strcat(par.Sample);
30  end
31
32  %Make sure the input file name is unique within the folder.
33  if exist([par.Directory, par.FileName, '_IncreasingDelay.mat'], '
        file')
34      error('File name already exists within directory. Please change
            settings or save in a new folder.');
35  end
36
37  %Save a parameter file in folder
38  InfoFile = strcat(par.Directory, par.FileName, 'Notes.txt');
39  Parameter = {'Start Time'; 'Step Size'; 'Total Number of Steps'; '
        Laser Power'; 'Sample'; 'Time Constant';'Burst duration'; 'Note'
        };
40  val.StepSize = num2str(par.StepSize);
41  val.Distance = num2str(par.Distance);
42  val.TC = num2str(par.TC);
43  val.BurstTime = num2str(par.BurstTime);
44  info = {par.StartTime; val.StepSize; val.Distance; par.Power; par.
        Sample; val.TC;val.BurstTime; par.Notes };
45  L = table(Parameter, info);
46  writetable (L, InfoFile);
47
48  %% Initialize any relevant devices.
49
50  device_name = detect_stage();
51  device_id = open_stage(device_name);
52
53  %Set the short stage to start at its first position
54  if par.BigStep == 1
55      move_stage( device_id,  par.StepPos0, 0);
56      close_stage(device_id);
57  else
58      move_stage( device_id,  0, 0);
59  end
60
```

```
61 a = arduino('COM7', 'Uno', 'Libraries', 'Adafruit\MotorShieldV2');
62 shield = addon(a,'Adafruit/MotorShieldV2');
63 sm = stepper(shield, 2, 200, 'StepType', 'Double', 'RPM', 2);
64
65 for i = 1:par.NumScans
66     %% Create array for saving data
67     FinalData = 0:par.StepSize:par.Distance;
68
69     %If moving in both directions make a second array
70     if par.BothDirections == 1
71         FinalDataBack = par.Distance:-par.StepSize:0;
72         FinalDataBack(2,:) = NaN(1, length(FinalDataBack));
73     end
74
75     % Callibrate step size to the stage that's moving.
76     if par.BigStep == 0
77         FinalData = (FinalData * par.ShortStage_Callibration) + par
               .Offset*par.LongStage_Callibration;
78         if par.BothDirections == 1
79             FinalDataBack = (FinalDataBack * par.
                   ShortStage_Callibration)+ par.Offset*par.
                   LongStage_Callibration;
80         end
81     end
82     if par.BigStep == 1
83         FinalData = (FinalData * par.LongStage_Callibration)+ par.
               Offset*par.LongStage_Callibration+par.StepPos0*par.
               ShortStage_Callibration;
84         if par.BothDirections == 1
85             FinalDataBack = (FinalDataBack * par.
                   LongStage_Callibration)+ par.Offset*par.
                   LongStage_Callibration+par.StepPos0*par.
                   ShortStage_Callibration;
86         end
87     end
88     FinalData(2,:) = NaN(1, length(FinalData));
89
```

```
90      if ((par.NumScans > 1) && (i ==1))
91          TotAvg = FinalData;
92          TotAvg(2,:) = zeros(1,length(TotAvg));
93          OGFileName = par.FileName;
94      end
95      if par.NumScans > 1
96          par.FileName = strcat(num2str(i), '_', OGFileName);
97      end
98
99      %% Move and Measure
100
101     StepPos = 0; % Initial step position set to zero for the stage
            that will be moving.
102     num = 1; % Counting for the saved data.
103
104     % Take first measurment before moving
105     Christie_TRMOKE_InitZiDAQ(par);
106     [FinalData(2,num)] = Christie_TRMOKE_Measure_WSig(par);
107     % Positive direction in both stages INCREASES the time delay.
108     if par.BigStep == 1
109
110         while StepPos < par.Distance
111             StepPos = StepPos + par.StepSize;
112             num = num + 1;
113             move(sm, par.StepSize);
114             currentStep = num2str(StepPos);
115             statement = strcat('Current Position = ', currentStep);
116             disp(statement);
117             pause(par.TimeDelay);
118
119             Christie_TRMOKE_InitZiDAQ(par);
120             [FinalData(2,num)] = Christie_TRMOKE_Measure_WSig(par);
121
122             %plot every so many measurements as set by you.
123             if mod(num, par.FreqPlot) == 0
124                 figure(1)
125                 clf()
```

```
126                 title('TR-MOKE Signal Response (Forward)');
127                 xlabel('Relative Time Delay (ps)')
128                 ylabel('Response (V) ')
129                 xlim([FinalData(1,1), FinalData(1,length(FinalData
                        (1,:)))]);
130                 hold on;
131                 plot(FinalData(1,:), FinalData(2,:));
132             end
133         end
134
135         %Plot one more time in case there are measurements that are
                yet to get
136         %plotted.
137         figure(1)
138         clf()
139         title('TR-MOKE Signal Response (Forward)');
140         xlabel('Relative Time Delay (ps)')
141         ylabel('Response (V) ')
142         xlim([FinalData(1,1), FinalData(1,length(FinalData(1,:)))])
                ;
143         hold on;
144         plot(FinalData(1,:), FinalData(2,:));
145
146         %Save the first figure
147         savefig([par.Directory, par.FileName, '_IncreasingDelay.fig
                ']);
148         saveas(gcf, [par.Directory, par.FileName, '_IncreasingDelay
                .png']);
149
150         %Save collected data
151         save([par.Directory, par.FileName,'_IncreasingDelay.mat'],'
                FinalData');
152         Christie_Save2txt(FinalData, par.Directory, par.FileName, '
                _IncreasingDelay');
153
154         if par.BothDirections == 1
155             num = 1;
```

```
156
157             % Take first measurment before moving
158             Christie_TRMOKE_InitZiDAQ(par);
159             [FinalDataBack(2,num)] = Christie_TRMOKE_Measure_WSig(
                    par);
160
161             while StepPos > 0
162                 StepPos = StepPos - par.StepSize;
163                 num = num + 1;
164                 move(sm, -par.StepSize);
165                 currentStep = num2str(StepPos);
166                 statement = strcat('Current Position = ',
                        currentStep);
167                 disp(statement);
168                 pause(par.TimeDelay);
169
170                 Christie_TRMOKE_InitZiDAQ(par);
171                 [FinalDataBack(2,num)] =
                        Christie_TRMOKE_Measure_WSig(par);
172
173                 %plot every so many measurements as set by you.
174                 if mod(num, par.FreqPlot) == 0
175                     figure(2)
176                     clf()
177                     title('TR-MOKE Signal Response (Backward)');
178                     xlabel('Relative Time Delay (ps)')
179                     ylabel('Response (V) ')
180                     xlim([FinalData(1,1), FinalData(1,length(
                            FinalData(1,:)))]);
181                     hold on;
182                     plot(FinalDataBack(1,:), FinalDataBack(2,:));
183                 end
184             end
185
186             figure(2)
187             clf()
188             title('TR-MOKE Signal Response (Backward)');
```

```
189         xlabel('Relative Time Delay (ps)')
190         ylabel('Response (V) ')
191         xlim([FinalData(1,1), FinalData(1,length(FinalData(1,:)
                ))]);
192         hold on;
193         plot(FinalDataBack(1,:), FinalDataBack(2,:));
194
195         %Save the second figure
196         savefig([par.Directory, par.FileName, '_DecreasingDelay
                .fig']);
197         saveas(gcf, [par.Directory, par.FileName, '
                _DecreasingDelay.png']);
198
199         %Flip backwards data so comparing becomes easier
200         FinalDataBack(1,:) = flip(FinalDataBack(1,:));
201         FinalDataBack(2,:) = flip(FinalDataBack(2,:));
202
203         %Save this collected data
204         save([par.Directory, par.FileName,'_DecreasingDelay.mat
                '],'FinalDataBack');
205         Christie_Save2txt(FinalDataBack, par.Directory, par.
                FileName, '_DecreasingDelay');
206
207         %Average the forward and backward data and save the
                plot.
208         AverageData = FinalData;
209         AverageData(2,:) = (FinalData(2,:) + FinalDataBack(2,:)
                )./2;
210         %Put the averaged data in terms of mV to make
211         %understanding the plots a little easier.
212         AverageData(2,:) = AverageData(2,:) .*1000;
213
214         figure(3)
215         clf()
216         title('Averaged TR-MOKE Signal Response');
217         xlabel('Relative Time Delay (ps)')
218         ylabel('Response (mV) ')
```

```
219             xlim([FinalData(1,1), FinalData(1,length(FinalData))]);
220             hold on;
221             plot(AverageData(1,:), AverageData(2,:));
222
223             %Save the averaged Data.
224             savefig([par.Directory, par.FileName, 'Average.fig']);
225             saveas(gcf, [par.Directory, par.FileName, 'Average.png'
                    ])
226
227             %Save this collected data
228             save([par.Directory, par.FileName,'Average.mat'],'
                    AverageData');
229             Christie_Save2txt(AverageData, par.Directory, par.
                    FileName, '_Average');
230
231             Diff = FinalData;
232             Diff(2,:) = Diff(2,:) - FinalDataBack(2,:);
233
234             figure(4)
235             clf()
236             title('Forward/Backward Difference');
237             xlabel('Relative Time Delay (ps)')
238             ylabel('Response (V) ')
239             xlim([FinalData(1,1), FinalData(1,length(FinalData(1,:)
                    ))]);
240             hold on;
241             plot(Diff(1,:), Diff(2,:));
242
243             %Save the difference Data.
244             savefig([par.Directory, par.FileName, 'Diff.fig']);
245             saveas(gcf, [par.Directory, par.FileName, 'Diff.png'])
246
247             %Save this difference data data
248             save([par.Directory, par.FileName,'Diff.mat'],'Diff');
249             Christie_Save2txt(Diff, par.Directory, par.FileName, '
                    _Diff');
250
```

```
251         else
252             move(sm, -par.Distance);
253         end
254         clear ziDAQ;
255         close_stage(device_id);
256 
257     else  % If moving with the short stage instead.
258         while StepPos < par.Distance
259             StepPos = StepPos + par.StepSize;
260             num = num + 1;
261             move_stage(device_id, StepPos, 0);
262             currentStep = num2str(StepPos);
263             statement = strcat('Current Position = ', currentStep);
264             disp(statement);
265             pause(par.TimeDelay);
266 
267             Christie_TRMOKE_InitZiDAQ(par);
268             [FinalData(2,num)] = Christie_TRMOKE_Measure_WSig(par);
269 
270             %plot every so many measurements as set by you.
271             if mod(num, par.FreqPlot) == 0
272                 figure(1)
273                 clf()
274                 title('TR-MOKE Signal Response (Forward)');
275                 xlim([FinalData(1,1), FinalData(1,length(FinalData)
                        )]);
276                 xlabel('Relative Time Delay (ps)')
277                 ylabel('Response (V) ')
278                 hold on;
279                 plot(FinalData(1,:), FinalData(2,:));
280 
281             end
282         end
283 
284         %Plot one more time in case there are measurements that are
                yet to get
285         %plotted.
```

```
286         figure(1)
287         clf()
288         title('TR-MOKE Signal Response (Forward)');
289         xlabel('Relative Time Delay (ps)')
290         ylabel('Response (V) ')
291         xlim([FinalData(1,1), FinalData(1,length(FinalData))]);
292         hold on;
293         plot(FinalData(1,:), FinalData(2,:));
294
295         %Save the first figure
296         savefig([par.Directory, par.FileName, 'IncreasingDelay.fig'
                ]);
297         saveas(gcf, [par.Directory, par.FileName, '_IncreasingDelay
                .png']);
298
299         %Save collected data
300         save([par.Directory, par.FileName,'IncreasingDelay.mat'],'
                FinalData');
301         Christie_Save2txt(FinalData, par.Directory, par.FileName, '
                _IncreasingDelay');
302
303         if par.BothDirections == 1
304             num = 1;
305
306             % Take first measurment before moving
307             Christie_TRMOKE_InitZiDAQ(par);
308             [FinalDataBack(2,num)] = Christie_TRMOKE_Measure_WSig(
                    par);
309
310             while StepPos > 0
311                 StepPos = StepPos - par.StepSize;
312                 num = num + 1;
313                 move_stage(device_id, StepPos, 0);
314                 currentStep = num2str(StepPos);
315                 statement = strcat('Current Position = ',
                        currentStep);
316                 disp(statement);
```

```
317                 pause(par.TimeDelay);
318
319                 Christie_TRMOKE_InitZiDAQ(par);
320                 [FinalDataBack(2,num)] =
                        Christie_TRMOKE_Measure_WSig(par);
321
322                 %plot every so many measurements as set by you.
323                 if mod(num, par.FreqPlot) == 0
324                     figure(2)
325                     clf()
326                     title('TR-MOKE Signal Response (Backward)');
327                     xlim([FinalData(1,1), FinalData(1,length(
                            FinalData))]);
328                     xlabel('Relative Time Delay (ps)')
329                     ylabel('Response (V) ')
330                     hold on;
331                     plot(FinalDataBack(1,:), FinalDataBack(2,:));
332
333                 end
334             end
335
336             figure(2)
337             clf()
338             title('TR-MOKE Signal Response (Backward)');
339             xlabel('Relative Time Delay (ps)')
340             ylabel('Response (V) ')
341             xlim([FinalData(1,1), FinalData(1,length(FinalData))]);
342             hold on;
343             plot(FinalDataBack(1,:), FinalDataBack(2,:));
344
345             %Flip results so comparison to other direction is
                    easier.
346             FinalDataBack(1,:) = flip(FinalDataBack(1,:));
347             FinalDataBack(2,:) = flip(FinalDataBack(2,:));
348
349             %Save the second figure
350             savefig([par.Directory, par.FileName, 'DecreasingDelay.
```

```
    fig']);
351 saveas(gcf, [par.Directory, par.FileName, '
    _DecreasingDelay.png'])
352
353 %Save this collected data
354 save([par.Directory, par.FileName,'DecreasingDelay.mat'
    ],'FinalDataBack');
355 Christie_Save2txt(FinalDataBack, par.Directory, par.
    FileName, '_DecreasingDelay');
356 %               close_stage(device_id);
357
358 %Average the forward and backward data and save the
    plot.
359 AverageData = FinalData;
360 AverageData(2,:) = (FinalData(2,:) + FinalDataBack(2,:)
    )./2;
361 %Put the averaged data in terms of micro volts to make
362 %understanding the plots a little easier.
363 AverageData(2,:) = AverageData(2,:) .*1000;
364
365 figure(3)
366 clf()
367 title('Averaged TR-MOKE Signal Response');
368 xlabel('Relative Time Delay (ps)')
369 ylabel('Response (mV) ')
370 xlim([FinalData(1,1), FinalData(1,length(FinalData))]);
371 hold on;
372 plot(AverageData(1,:), AverageData(2,:));
373
374 %Save the averaged Data.
375 savefig([par.Directory, par.FileName, 'Average.fig']);
376 saveas(gcf, [par.Directory, par.FileName, 'Average.png'
    ])
377
378 %Save this collected data
379 save([par.Directory, par.FileName,'Average.mat'],'
    AverageData');
```

```
380             Christie_Save2txt(AverageData, par.Directory, par.
                    FileName, '_Average');
381
382
383             Diff = FinalData;
384             Diff(2,:) = Diff(2,:) - FinalDataBack(2,:);
385
386             figure(4)
387             clf()
388             title('Forward/Backward Difference');
389             xlabel('Relative Time Delay (ps)')
390             ylabel('Response (V) ')
391             xlim([FinalData(1,1), FinalData(1,length(FinalData(1,:)
                    ))]);
392             hold on;
393             plot(Diff(1,:), Diff(2,:));
394
395             %Save the difference Data.
396             savefig([par.Directory, par.FileName, 'Diff.fig']);
397             saveas(gcf, [par.Directory, par.FileName, 'Diff.png'])
398
399             %Save this difference data data
400             save([par.Directory, par.FileName,'Diff.mat'],'Diff');
401             Christie_Save2txt(Diff, par.Directory, par.FileName, '
                    _Diff');
402
403         else
404             move_stage(device_id, 0, 0);
405             %               close_stage(device_id);
406         end
407         clear ziDAQ;
408     end
409     if par.NumScans > 1
410         if par.BothDirections == 0
411             AverageData = FinalData;
412         end
413         TotAvg(2,:) = TotAvg(2,:) + AverageData(2,:);
```

```
414     end
415 end
416 if par.BigStep == 0
417     close_stage(device_id);
418 end
419 if par.NumScans > 1
420     TotAvg(2,:) = TotAvg(2,:)./par.NumScans;
421     par.FileName = strcat(par.Sample);
422 
423     figure(5)
424     clf()
425     title('Average of Scans');
426     xlabel('Relative Time Delay (ps)')
427     ylabel('Response (mV) ')
428     xlim([TotAvg(1,1), TotAvg(1,length(TotAvg(1,:)))]);
429     hold on;
430     plot(TotAvg(1,:), TotAvg(2,:));
431 
432     %Save the difference Data.
433     savefig([par.Directory, par.FileName, 'TotAvg.fig']);
434     saveas(gcf, [par.Directory, par.FileName, 'TotAvg.png'])
435 
436     %Save this difference data data
437     save([par.Directory, par.FileName,'TotAvg.mat'],'TotAvg');
438     Christie_Save2txt(TotAvg, par.Directory, par.FileName, '_TotAvg
        ');
439 end
440 end
```

Bibliography

[1] J. Coey, "Magnetism in future," *Journal of Magnetism and Magnetic Materials*, vol. 226, pp. 2107–2112, 2001.

[2] J. M. Coey, *Magnetism and magnetic materials*. Cambridge university press, 2010.

[3] W. Kang, H. Wang, Z. Wang, Y. Zhang, and W. Zhao, "In-memory processing paradigm for bitwise logic operations in stt–mram," *IEEE Transactions on Magnetics*, vol. 53, no. 11, pp. 1–4, 2017.

[4] R. L. Stamps, S. Breitkreutz, J. Åkerman, A. V. Chumak, Y. Otani, G. E. Bauer, J.-U. Thiele, M. Bowen, S. A. Majetich, M. Kläui *et al.*, "The 2014 magnetism roadmap," *Journal of Physics D: Applied Physics*, vol. 47, no. 33, p. 333001, 2014.

[5] D. Sander, S. O. Valenzuela, D. Makarov, C. Marrows, E. Fullerton, P. Fischer, J. McCord, P. Vavassori, S. Mangin, P. Pirro *et al.*, "The 2017 magnetism roadmap," *Journal of Physics D: Applied Physics*, vol. 50, no. 36, p. 363001, 2017.

[6] E. Y. Vedmedenko, R. K. Kawakami, D. D. Sheka, P. Gambardella, A. Kirilyuk, A. Hirohata, C. Binek, O. Chubykalo-Fesenko, S. Sanvito, B. J. Kirby *et al.*, "The 2020 magnetism roadmap," *Journal of Physics D: Applied Physics*, vol. 53, no. 45, p. 453001, 2020.

[7] C. D. Stanciu, F. Hansteen, A. V. Kimel, A. Kirilyuk, A. Tsukamoto, A. Itoh, and T. Rasing, "All-optical magnetic recording with circularly polarized light," *Physical review letters*, vol. 99, no. 4, p. 047601, 2007.

[8] M. Freeman, R. Ruf, and R. Gambino, "Picosecond pulsed magnetic fields for studies of ultrafast magnetic phenomena," *IEEE transactions on magnetics*, vol. 27, no. 6, pp. 4840–4842, 1991.

[9] W. K. Hiebert, "Experimental micromagnetic dynamics: ultrafast magnetization reversal using time resolved scanning kerr effect microscopy," Ph.D. dissertation, University of Alberta, 2001.

[10] A. A. Mills, "The lodestone: History, physics, and formation," *Annals of Science*, vol. 61, no. 3, pp. 273–319, 2004.

[11] W. Gilbert, "De magnete (1600); english translation," 1958.

[12] R. B. Lindsay, "William gilbert and magnetism in 1600," *American Journal of Physics*, vol. 8, no. 5, pp. 271–282, 1940.

[13] H. C. Oersted, "Experiments on the effect of a current of electricity on the magnetic needle," *Annals of Philosophy*, vol. 16, no. 1820, pp. 273–276, 1820.

[14] D. C. Mattis, "History of magnetism," in *The Theory of Magnetism I*. Springer, 1981, pp. 1–38.

[15] M. Faraday, "On the magnetization of light and the illumination of magnetic lines of force," *Philosophical Transactions of the Royal Society of London*, vol. 136, pp. 1–20, 1846.

[16] M. Freiser, "A survey of magnetooptic effects," *IEEE Transactions on magnetics*, vol. 4, no. 2, pp. 152–161, 1968.

[17] J. Kerr, "Xliii. on rotation of the plane of polarization by reflection from the pole of a magnet," *The London, Edinburgh, and Dublin Philosophical Magazine and Journal of Science*, vol. 3, no. 19, pp. 321–343, 1877.

[18] ——, "Xxiv. on reflection of polarized light from the equatorial surface of a magnet," *The London, Edinburgh, and Dublin Philosophical Magazine and Journal of Science*, vol. 5, no. 30, pp. 161–177, 1878.

[19] P. Weiss, "L'hypothèse du champ moléculaire et la propriété ferromagnétique," *J. Phys. Theor. Appl.*, vol. 6, no. 1, pp. 661–690, 1907.

[20] ——, "Sur la rationalité des rapports des moments magnétiques moléculaires et le magnéton," *J. Phys. Theor. Appl.*, vol. 1, no. 1, pp. 965–988, 1911.

[21] H. Kliem, M. Kuehn, and B. Martin, "The weiss field revisited," *Ferroelectrics*, vol. 400, no. 1, pp. 41–51, 2010.

[22] R. M. White, *Quantum theory of magnetism*. Springer, 1983, vol. 1.

[23] W. Heisenberg, "Zur theorie des ferromagnetismus," in *Original Scientific Papers Wissenschaftliche Originalarbeiten*. Springer, 1985, pp. 580–597.

[24] S. Blundell, "Magnetism in condensed matter," 2003.

[25] N. W. Ashcroft and N. D. Mermin, *Solid state physics*. Cengage Learning, 2022.

[26] M. Suzuki and I. S. Suzuki, "Lecture note on solid state physics superexchange interaction," *Binghamton, New York*, pp. 13 902–6000, 2009.

[27] E. Koch, "Exchange mechanisms," *Correlated electrons: from models to materials*, vol. 2, pp. 1–31, 2012.

[28] L. Landau and E. Lifshitz, "On the theory of the dispersion of magnetic permeability in ferromagnetic bodies," in *Perspectives in Theoretical Physics*. Elsevier, 1935, pp. 51–65.

[29] T. L. Gilbert, "A lagrangian formulation of the gyromagnetic equation of the magnetization field," *Phys. Rev.*, vol. 100, p. 1243, 1955.

[30] M. Lakshmanan, "The fascinating world of the landau–lifshitz–gilbert equation: an overview," *Philosophical Transactions of the Royal Society A: Mathematical, Physical and Engineering Sciences*, vol. 369, no. 1939, pp. 1280–1300, 2011.

[31] A. Vansteenkiste and B. Van de Wiele, "Mumax: A new high-performance micromagnetic simulation tool," *Journal of Magnetism and Magnetic Materials*, vol. 323, no. 21, pp. 2585–2591, 2011.

[32] W. D. Doyle, S. Stinnett, C. Dawson, and L. He, "Magnetization reversal at high speed-an old problem in a new context," *The Magnetics Society of Japan*, vol. 22, no. 3, pp. 91–106, 1998.

[33] M. Blois Jr, "Preparation of thin magnetic films and their properties," *Journal of Applied Physics*, vol. 26, no. 8, pp. 975–980, 1955.

[34] R. Conger, "Magnetization reversal in thin films," *Physical Review*, vol. 98, no. 6, p. 1752, 1955.

[35] Z. Jin, H. Ma, L. Wang, G. Ma, F. Guo, and J. Chen, "Ultrafast all-optical magnetic switching in natb (wo 4) 2," *Applied Physics Letters*, vol. 96, no. 20, p. 201108, 2010.

[36] J. Gorchon, C.-H. Lambert, Y. Yang, A. Pattabi, R. B. Wilson, S. Salahuddin, and J. Bokor, "Single shot ultrafast all optical magnetization switching of ferromagnetic co/pt multilayers," *Applied physics letters*, vol. 111, no. 4, p. 042401, 2017.

[37] C. Davies, G. Bonfiglio, K. Rode, J. Besbas, C. Banerjee, P. Stamenov, J. Coey, A. Kimel, and A. Kirilyuk, "Exchange-driven all-optical magnetic switching in compensated 3 d ferrimagnets," *Physical Review Research*, vol. 2, no. 3, p. 032044, 2020.

[38] R. A. Beth, "Mechanical detection and measurement of the angular momentum of light," *Physical Review*, vol. 50, no. 2, p. 115, 1936.

[39] K. S. Vul'fson, "Angular momentum of electromagnetic waves," *Soviet Physics Uspekhi*, vol. 30, no. 8, p. 724, 1987.

[40] A. Kimel, A. Kirilyuk, P. Usachev, R. Pisarev, A. Balbashov, and T. Rasing, "Ultrafast non-thermal control of magnetization by instantaneous photomagnetic pulses," *Nature*, vol. 435, no. 7042, pp. 655–657, 2005.

[41] R. Hertel, "Theory of the inverse faraday effect in metals," *Journal of magnetism and magnetic materials*, vol. 303, no. 1, pp. L1–L4, 2006.

[42] M. Battiato, G. Barbalinardo, and P. M. Oppeneer, "Quantum theory of the inverse faraday effect," *Physical review B*, vol. 89, no. 1, p. 014413, 2014.

[43] E. Beaurepaire, J.-C. Merle, A. Daunois, and J.-Y. Bigot, "Ultrafast spin dynamics in ferromagnetic nickel," *Physical review letters*, vol. 76, no. 22, p. 4250, 1996.

[44] G. Zhang and W. Hübner, "Laser-induced ultrafast demagnetization in ferromagnetic metals," *Physical review letters*, vol. 85, no. 14, p. 3025, 2000.

[45] F. Dalla Longa, J. Kohlhepp, W. De Jonge, and B. Koopmans, "Influence of photon angular momentum on ultrafast demagnetization in nickel," *Physical Review B*, vol. 75, no. 22, p. 224431, 2007.

[46] A. Eschenlohr, M. Battiato, P. Maldonado, N. Pontius, T. Kachel, K. Holldack, R. Mitzner, A. Föhlisch, P. M. Oppeneer, and C. Stamm, "Ultrafast spin transport as key to femtosecond demagnetization," *Nature materials*, vol. 12, no. 4, pp. 332–336, 2013.

[47] B. Vodungbo, B. Tudu, J. Perron, R. Delaunay, L. Müller, M. H. Berntsen, G. Grübel, G. Malinowski, C. Weier, J. Gautier *et al.*, "Indirect excitation of ultrafast demagnetization," *Scientific reports*, vol. 6, no. 1, pp. 1–9, 2016.

[48] Z. Chai, X. Hu, F. Wang, X. Niu, J. Xie, and Q. Gong, "Ultrafast all-optical switching," *Advanced Optical Materials*, vol. 5, no. 7, p. 1600665, 2017.

[49] Y. Quessab, M. Deb, J. Gorchon, M. Hehn, G. Malinowski, and S. Mangin, "Resolving the role of magnetic circular dichroism in multishot helicity-dependent all-optical switching," *Physical Review B*, vol. 100, no. 2, p. 024425, 2019.

[50] P. Stephens, "Magnetic circular dichroism," *Annual Review of Physical Chemistry*, vol. 25, no. 1, pp. 201–232, 1974.

[51] A. Prabhakar and D. D. Stancil, *Spin waves: Theory and applications*. Springer, 2009, vol. 5.

[52] T. Holstein and H. Primakoff, "Field dependence of the intrinsic domain magnetization of a ferromagnet," *Physical Review*, vol. 58, no. 12, p. 1098, 1940.

[53] C. Kittel, "On the theory of ferromagnetic resonance absorption," *Physical review*, vol. 73, no. 2, p. 155, 1948.

[54] S. O. Demokritov and A. N. Slavin, *Magnonics: From fundamentals to applications*. Springer Science & Business Media, 2012, vol. 125.

[55] K. Perzlmaier, G. Woltersdorf, and C. H. Back, "Observation of the propagation and interference of spin waves in ferromagnetic thin films," *Physical Review B*, vol. 77, no. 5, p. 054425, 2008.

[56] G. Ju, A. Vertikov, A. Nurmikko, C. Canady, G. Xiao, R. Farrow, and A. Cebollada, "Ultrafast nonequilibrium spin dynamics in a ferromagnetic thin film," *Physical Review B*, vol. 57, no. 2, p. R700, 1998.

[57] E. Beaurepaire, M. Maret, V. Halté, J.-C. Merle, A. Daunois, and J.-Y. Bigot, "Spin dynamics in copt 3 alloy films: A magnetic phase transition in the femtosecond time scale," *Physical Review B*, vol. 58, no. 18, p. 12134, 1998.

[58] S.-i. Ohkoshi and H. Tokoro, "Hard magnetic ferrite: ε-Fe_2O_3," *Bulletin of the Chemical Society of Japan*, vol. 86, no. 8, pp. 897–907, 2013.

[59] P. Weinberger, "John kerr and his effects found in 1877 and 1878," *Philosophical Magazine Letters*, vol. 88, no. 12, pp. 897–907, 2008.

[60] W. K. Hiebert, "Ferromagnetic resonance in a permalloy microstructure using time resolved scanning kerr effect microscopy," 1998.

[61] C. Robinson, "Electromagnetic theory of the kerr and the faraday effects for oblique incidence," *JOSA*, vol. 54, no. 10, pp. 1220–1224, 1964.

[62] ThorLabs, "Pulsed Lasers Introduction to Power and Energy Calculations Serving the Intellectually Curious Pulsed laser or CW laser , does it make a difference ?" 2019. [Online]. Available: https://www.thorlabs.com/images/tabimages/Laser_Pulses_Power_Energy_Equations.pdf

[63] KMLABS, "KMLABS Y-Fi Manual," Boulder, Tech. Rep. [Online]. Available: https://www.thorlabs.com/images/TabImages/KML_YFi%20Series_180817.pdf

[64] R. Boyd, "Nonlinear optics 3rd edn, ed rw boyd (burlington: Academic)," 2008.

[65] D. Jeong, "Second harmonic generation in nonlinear optical crystal," 2005.

[66] S. G. Turyshev, J. G. Williams, W. M. Folkner, G. M. Gutt, R. T. Baran, R. C. Hein, R. P. Somawardhana, J. A. Lipa, and S. Wang, "Corner-cube retro-reflector instrument for advanced lunar laser ranging," *Experimental Astronomy*, vol. 36, no. 1, pp. 105–135, 2013.

[67] P. Bender, D. Currie, S. Poultney, C. Alley, R. Dicke, D. Wilkinson, D. Eckhardt, J. Faller, W. Kaula, J. Mulholland *et al.*, "The lunar laser ranging experiment: Accurate ranges have given a large improvement in the lunar orbit and new selenophysical information." *Science*, vol. 182, no. 4109, pp. 229–238, 1973.

[68] J. Liu and R. Azzam, "Polarization properties of corner-cube retroreflectors: theory and experiment," *Applied optics*, vol. 36, no. 7, pp. 1553–1559, 1997.

[69] M. S. Scholl, "Ray trace through a corner-cube retroreflector with complex reflection coefficients," *JOSA A*, vol. 12, no. 7, pp. 1589–1592, 1995.

[70] A. Gerrard and J. M. Burch, *Introduction to matrix methods in optics*. Courier Corporation, 1994.

[71] B. Park, T. Eom, and M. Chung, "Polarization properties of cube-corner retroreflectors and their effects on signal strength and nonlinearity in heterodyne interferometers," *Applied optics*, vol. 35, no. 22, pp. 4372–4380, 1996.

[72] S. E. Segre and V. Zanza, "Mueller calculus of polarization change in the cube-corner retroreflector," *JOSA A*, vol. 20, no. 9, pp. 1804–1811, 2003.

[73] R. Kalibjian, "Stokes polarization vector and mueller matrix for a corner-cube reflector," *Optics communications*, vol. 240, no. 1-3, pp. 39–68, 2004.

[74] R. Chang, D. G. Currie, C. Alley, and M. Pittman, "Far-field diffraction pattern for corner reflectors with complex reflection coefficients," *JOSA*, vol. 61, no. 4, pp. 431–438, 1971.

[75] Y. A. Kravtsov and B. Bieg, "Evolution of complex amplitudes ratio in weakly anisotropic plasma," *Journal of plasma physics*, vol. 76, no. 5, pp. 795–807, 2010.

[76] EdmundOptic, "50.8mm Clear Aperture, 2 Arcsec, Gold Retroreflector." [Online]. Available: https://www.edmundoptics.com/p/508mm-clear-aperture-2-arcsec-gold-retroreflector/10180/

[77] B. E. Saleh and M. C. Teich, *Fundamentals of photonics*. Wiley, 2019.

[78] D. Allwood, G. Xiong, M. Cooke, and R. Cowburn, "Magneto-optical kerr effect analysis of magnetic nanostructures," *Journal of Physics D: Applied Physics*, vol. 36, no. 18, p. 2175, 2003.

[79] D. Hou, Z. Qiu, R. Iguchi, K. Sato, E. Vehstedt, K. Uchida, G. Bauer, and E. Saitoh, "Observation of temperature-gradient-induced magnetization," *Nature communications*, vol. 7, no. 1, pp. 1–6, 2016.

[80] Y. Yamamoto, T. Miura, M. Suzuki, N. Kawamura, H. Miyagawa, T. Nakamura, K. Kobayashi, T. Teranishi, and H. Hori, "Direct observation of ferromagnetic spin polarization in gold nanoparticles," *Physical review letters*, vol. 93, no. 11, p. 116801, 2004.

[81] M. Trainer, "The 50th anniversary of the laser," *World Patent Information*, vol. 32, no. 4, pp. 326–330, 2010.

[82] J. Hecht, "A short history of laser development," *Applied optics*, vol. 49, no. 25, pp. F99–F122, 2010.

[83] Brown University, "Measuring Ultrashort Laser Pulses I: Autocorrelation," pp. 1–42. [Online]. Available: https://www.brown.edu/research/labs/mittleman/sites/brown.edu.research.labs.mittleman/files/uploads/lecture14.pdf

[84] F. Smith, H. Le, V. Diadiuk, M. Hollis, A. Calawa, S. Gupta, M. Frankel, D. Dykaar, G. Mourou, and T. Hsiang, "Picosecond gaas-based photoconductive optoelectronic detectors," *Applied Physics Letters*, vol. 54, no. 10, pp. 890–892, 1989.

[85] D. Bertram, R. Klann, H. Grahn, K. v. Klitzing, and K. Eberl, "Time-resolved electroluminescence spectroscopy of resonant tunneling in gaas-alas superlattices," *Applied physics letters*, vol. 68, no. 21, pp. 2921–2923, 1996.

[86] F. Yi, J. B. DeLisio, N. Nguyen, M. R. Zachariah, and D. A. LaVan, "High heating rate decomposition dynamics of copper oxide by nanocalorimetry-coupled time-of-flight mass spectrometry," *Chemical Physics Letters*, vol. 689, pp. 26–29, 2017.

[87] V.-H. Castrejón-Sánchez, A. C. Solís, R. López, C. Encarnación-Gomez, F. M. Morales, O. S. Vargas, J. E. Mastache-Mastache, and G. V. Sánchez, "Thermal oxidation of copper over a broad temperature range: towards the formation of cupric oxide (cuo)," *Materials Research Express*, vol. 6, no. 7, p. 075909, 2019.

[88] GoldPlatingServices, "Gold Plating Jewelty," 2022. [Online]. Available: https://www.goldplating.com/pages/jewelry

[89] C. B. Larsen, J. D. Braun, I. B. Lozada, K. Kunnus, E. Biasin, C. Kolodziej, C. Burda, A. A. Cordones, K. J. Gaffney, and D. E. Herbert, "Reduction of electron repulsion in highly covalent fe-amido complexes counteracts the impact of a weak ligand field on excited-state ordering," *Journal of the American Chemical Society*, vol. 143, no. 49, pp. 20 645–20 656, 2021.